

Electronic Thesis and Dissertation Repository

6-11-2020 2:00 PM

A Genetically-Encoded Reporter for In Vivo Imaging in Deep Tissues

Nivin N. Nasri, *The University of Western Ontario*

Supervisor: Scholl, Timothy J., *The University of Western Ontario*

Co-Supervisor: Ronald, John A., *The University of Western Ontario*

A thesis submitted in partial fulfillment of the requirements for the Doctor of Philosophy degree in Medical Biophysics

© Nivin N. Nasri 2020

Follow this and additional works at: <https://ir.lib.uwo.ca/etd>



Part of the [Biotechnology Commons](#)

Recommended Citation

Nasri, Nivin N., "A Genetically-Encoded Reporter for In Vivo Imaging in Deep Tissues" (2020). *Electronic Thesis and Dissertation Repository*. 7130.

<https://ir.lib.uwo.ca/etd/7130>

This Dissertation/Thesis is brought to you for free and open access by Scholarship@Western. It has been accepted for inclusion in Electronic Thesis and Dissertation Repository by an authorized administrator of Scholarship@Western. For more information, please contact wlsadmin@uwo.ca.

Abstract

Introduction. The ability to track cells in living organisms with sensitivity, accuracy and high spatial resolution would revolutionize the way we study disease. Reporter genes are valuable tools as they encode detectable products, allowing for “reporting” of viable cells that express them. Previously, a gene encoding Organic anion-transporting polypeptide 1a1 (*Oatp1a1*) was established as a magnetic resonance imaging (MRI) reporter based on its ability to take up the paramagnetic contrast agent gadolinium ethoxybenzyl diethylenetriamine pentaacetic acid (Gd-EOB-DTPA). Our objective was to assess, characterize and further develop this system for whole-body tracking of cells *in vivo*. **Methods.** Cancer cells were engineered to synthetically express *Oatp1a1*, or *Oatp1b3*, a closely related human transporter protein. In our first study, T_1 -weighted images of *Oatp1a1*-expressing primary tumours in preclinical animals were acquired before and after administration of 0.1-mmol/kg Gd-EOB-DTPA at 3-Tesla. At endpoint, heterogenous contrast enhancement patterns within the primary tumour architecture were compared to whole-tumour fluorescent histology. In the next study, T_1 -weighted images of *Oatp1b3*-expressing primary tumours, and their spontaneous metastases to the lymph nodes and lungs, were acquired before and after administration of 1-mmol/kg Gd-EOB-DTPA at 3-Tesla. In the final study, the feasibility of *Oatp1b3* as a photoacoustic reporter gene was assessed by acquiring full-spectrum near infrared photoacoustic images of primary tumours in preclinical animals before and after administration of 8-mg/kg indocyanine green. **Results.** We were able to demonstrate the feasibility of imaging cancer cells with *Oatp1a1* at 3-Tesla and 0.1 mmol/kg Gd-EOB-DTPA. Importantly, as primary tumours grew over time, heterogeneous contrast

enhancement patterns that emerged near-endpoint strongly correlated to viable cell distributions on whole-tumour histology. *Oatp1b3* was also shown to operate as an MRI reporter gene at 3-Tesla, based on the same principle as *Oatp1a1*. Impressively, single lymph node metastases and the formation of micro-metastases in the lungs of preclinical animals were detected with *Oatp1b3*-MRI. Finally, we also demonstrated the ability of *Oatp1b3* to operate as a photoacoustic reporter gene based on its ability to take up indocyanine green. **Conclusion.** The *Oatp1* reporter gene system is a versatile imaging tool for spatiotemporal tracking of engineered cells *in vivo* with high sensitivity, high resolution, and 3-dimensional spatial information.

Keywords

Gadolinium, indocyanine green, magnetic resonance imaging, molecular imaging, optoacoustic imaging, organic anion-transporting polypeptide, photoacoustic imaging, reporter gene

Summary for Lay Audience

The ability to effectively detect a specific cell type, such as cancer cells, in the context of a larger, living biological organism would be useful for the study of medicine and, more broadly, for the life sciences. Though methods do exist to track cells non-invasively, the imaging is limited to superficial surfaces and/or sub-optimal resolution. Our work here tackles cellular imaging by focusing on magnetic resonance imaging (MRI) as a platform, allowing us to overcome several of these limitations. Unlike other imaging methods, MRI scanners produce highly detailed anatomical images and do not lose signal with increasing tissue depth. To image specific cells on MRI, we have developed a nanotechnology in the form of a protein that embeds itself on the surface of the cells we are interested in studying, and allows those cells to “pack” themselves with an MR imaging dye. Meanwhile, other cells do not have this capability. We test the effectiveness of this system for tracking cancer cells in preclinical animal models, and remarkably, it has allowed us to visualize the changing architecture of a primary tumour over time, as well as track the spread of cancer cells from the primary tumour to other parts of the body with high sensitivity and high resolution. This molecular technology can, in principle, be applied to any cell type, and paves the path for imaging various biological processes to better understand their mechanisms and develop new treatments for disease.

Co-authorship Statement

This thesis is presented in an integrated article format, the chapters of which are based on the following manuscripts that are either published or in preparation for submission. As first author on the peer-reviewed manuscripts, Nivin Nyström was a significant contributor to all aspects of the studies, manuscript preparation and submission. All work was performed under supervision of Dr. John Ronald and Dr. Timothy Scholl. Specific contributions of all other coauthors for each manuscript are described below.

Chapter 2 is an original research article reprinted from: NN Nyström, AM Hamilton, W Xia, S Liu, TJ Scholl, JA Ronald. Longitudinal visualization of viable cancer cell intratumoral distribution in mouse models using *Oatp1a1*-enhanced magnetic resonance imaging. *Investigative Radiology* 2019 May; 54(5): 302-311. NNN, TJS, and JAR designed the experiments. NNN conducted the experiments with help from AMH and SL. NNN analyzed the data with help from WX. NNN wrote the manuscript body. All authors edited and reviewed the manuscript.

Chapter 3 is in preparation for submission. NN Nyström, FM Martinez, JJ Kelly, TJ Scholl, JA Ronald. Dynamic whole-body tracking of metastasizing cancer cells using a genetically-encoded MR reporter. NNN, TJS, and JAR designed the experiments. NNN conducted the experiments with help from FMM and JJK. NNN analyzed the data. NNN wrote the manuscript body. All authors edited and reviewed the manuscript.

Chapter 4 is an original research article reprinted from: NN Nyström, LCM Yip, JLL Carson, TJ Scholl, JA Ronald. A human photoacoustic imaging reporter gene using the clinical dye indocyanine green. *Radiology: Imaging Cancer* 2019 November; 1(2): e190035. NNN, TJS, and JAR designed the experiments. NNN and LCMY conducted the experiments. NNN analyzed the data. NNN wrote the manuscript body. All authors edited and reviewed the manuscript.

To all the women who inspire me.

“Through countless generations, from the very beginning, the social subservience of women resulted naturally in the partial atrophy or at least the hereditary suspension of mental qualities which we now know the female sex to be endowed with no less than men... It is not in the shallow physical imitation of men that women will assert first their equality and later their superiority, but in the awakening of the intellect of women... The female mind has demonstrated a capacity for all the mental acquirements and achievements of men, and as generations ensue that capacity will be expanded; the average woman will be as well educated as the average man, and then better educated, for the dormant faculties of her brain will be stimulated to an activity that will be all the more intense and powerful because of centuries of repose. Woman will ignore precedent and startle civilization with her progress.”

- Nikola Tesla

When Woman Is Boss

January 30, 1926

Acknowledgements

I am extremely lucky to have been part of the Department of Medical Biophysics at the University of Western Ontario. I have been given the opportunity to work with brilliant scientists and learn with exceptional graduate students. I have had access to incredible resources and expertise at the Robarts Research Institute -- this place is unlike any in the world. It takes a village of experts to raise a junior scientist, and there are a number of people of whom I am greatly appreciative.

First, to my PhD supervisors, Dr. Timothy Scholl and Dr. John Ronald. I cannot describe the impact that each of you have had on my life in these past four years. I have learned a great deal from you. You both provided me with endless opportunities for success. You encouraged me to present my research at conferences around the world, and for its publication in competitive journals. Each manuscript and award would not have been possible without your mentorship and guidance. You also passionately support my future endeavors beyond the lab, and for that, I am very grateful.

To Tim: you have pushed me to investigate and analyze data beyond what I thought was intellectually possible for myself. You consistently strive for technical excellence and adopting this virtue from you has pushed my research expectations to new levels. You have also supported me greatly during difficult times in life outside of my PhD. You uphold very professional work relationships with your students, but you also care deeply for their personal well-being, and because of this, it has been an extraordinary pleasure to study as your trainee.

To John: you have introduced me more to a world of art than science. The creativity you bring into designing imaging technologies is remarkable. On this front, you have inspired me. Anyone coming into your lab is destined for success. Thank you for your mentorship, as well as your friendship. I was very lucky to have been one of your first students, and I cannot wait to see your lab grow over the next few years into an unstoppable force.

The rest of the Cellular and Molecular Imaging Group (CMIG) at Robarts has become a second family to me. Thank you to Dr. Paula Foster for being a part of my journey. You have provided me with career-shaping opportunities, from lending me your (Damadian-signed!) copy of “A Machine Called Indomitable,” to setting me up for invited talks with renowned researchers. Thank you for all of your advice and guidance, in and out of the scope of science. I will carry your wisdom with me throughout my career.

To Dr. Francisco “Paco” Martinez: if programming was an Olympic sport, you would be the gold medalist every quadrennial. Thank you for your support on my projects, especially for being there to troubleshoot my silly mistakes, for our lovely conversations, and for growing hot peppers and challenging people to eat them. To Dr. John “JK” Kelly: thank you for helping me with my Western blotting and immunofluorescent staining, and for being a great target to prank (and a good sport about it). You have made my graduate school experience a great deal more fun. To Dr. Yuanxin Chen: thank you for being a fellow night owl and making late work in the lab much more eventful.

I owe much gratitude to the CMIG students. When I first came in, I didn't know what to expect. Thank you to Dr. Ashley Makela for setting the bar high. You are a great role model, and continue to impress me even from across the border. Thank you to Dr. Heeseung Lim, for teaching me everything I know about practical MR and for pushing my troubleshooting abilities beyond limits. Thank you to my CMIG "brother" Nolan Broeke, who started graduate school with me. It was bittersweet to see you graduate: I was so happy for you, but our fun times were coming to an end. Playing midnight euchre with your siblings at the base of the Eiffel Tower has been the best conference finale so far. Thank you for all the wonderful memories.

I am also appreciative of TianDuo Wang, Xin Yue Wang, Nourhan Shalhab, Veronica Dubois, Olivia Sehl, Natasha Knier, and Ryan Williams who joined the lab after me, for their friendship and support. You are going to do great things. I know you will continue to grow the CMIG momentum with impactful publications and snag awards along the way. You are determined, hard-working, and intelligent -- you've got this!

Thanks are also due to everyone who helps run the Medical Biophysics program, particularly to the graduate chairs during my time there, Dr. Grace Parraga and Dr. Aaron Ward. Thank you for believing in me and for your leadership. Thanks are also due to the student body of the Medical Biophysics graduate program, who I have had the pleasure of personally meeting through my BIOPHYS 9700 teaching assistantship. The breadth of research and level of excellence exuded by your presentations is inspiring, and I'm happy to have played a small part in your great voyage.

I would additionally like to express my gratitude to Dr. Savita Dhanvantari, former Director of the Molecular Imaging Collaborative Program and current Director of the Biomedical Imaging Research Centre. You have consistently encouraged me to amplify my capacity, with respect to my knowledge of imaging science, as well as my career aspirations as a woman in science. You lead with passion, compassion, humour and style. Your mentorship during my PhD has been a great gift. To my advisory committee members, Dr. Gregory Dekaban and Dr. Muriel Brackstone: thank you for your scientific advice and for your support. I have sincerely enjoyed working with you and I appreciate everything you have done to contribute to my success.

I also owe immense appreciation to the funding sources which helped make this journey easier for myself and my supervisors: to the Molecular Imaging Collaborative Program, the Translational Breast Cancer Research Unit, the Schulich School of Medicine, the Natural Sciences and Engineering Council, the World Molecular Imaging Congress and the International Society for Magnetic Resonance in Medicine. I appreciate the effort that goes into raising funds to support trainees like myself.

Finally, an extraordinary thank you goes to the Nutbrowns. You welcomed me wholeheartedly into your family, and have spoiled me with your love. You have shown me that life can be so full of joy. You have given me strong character and an untroubled attitude. Thank you especially to my darling Drew: for your support, your companionship, and your adventurous spirit. You have been there for me from the beginning. I am so excited to marry you and live our incredible lives together.

Table of Contents

Abstract	ii
Keywords	iv
Summary for Lay Audience	v
Co-authorship Statement	vi
Dedication	viii
Epigraph	ix
Acknowledgement	xiii
Table of Contents	xiv
List of Tables	xix
List of Figures	xx
List of Abbreviations	xxi
Chapter 1 Introduction	1
<i>1.1 Motivation and Overview</i>	2
<i>1.2 Modeling Cancer</i>	4
1.2.1 Cancer Trends	
1.2.2 Preclinical Animal Models in Oncology	
1.2.3 Cancer Cell Lines and Tumour Initiation	
1.2.4 Established Mechanisms of Metastasis	
1.2.5 Modeling Metastatic Disease	
<i>1.3 Molecular Imaging</i>	15
1.3.1 Imaging Cancer in Patients	

1.3.2 Molecular Imaging of Cancer	
1.3.3 Targeted Molecular Probes	
1.3.4 <i>Ex Vivo</i> Cellular Loading	
1.3.5 Reporter Genes	
1.3.6 Multimodality Imaging	
<i>1.4 Bioluminescence Imaging</i>	25
1.4.1 Reporter Gene Development	
1.4.2 <i>In Vivo</i> Image Generation	
1.4.3 Applications for Cancer Research	
1.4.4 Limitations of Bioluminescence Imaging	
<i>1.5 Magnetic Resonance Imaging</i>	33
1.5.1 Magnetic Resonance Imaging in Medicine	
1.5.2 Nuclear Magnetic Resonance	
1.5.3 Generating Images	
1.5.4 Contrast in Images	
1.5.5 Reporter Genes for Magnetic Resonance Imaging	
1.5.6 Organic Anion-Transporting Polypeptides	
<i>1.6 Photoacoustic Imaging</i>	46
1.6.1 Basic Principles	
1.6.2 Applications for Cancer Research	
1.6.3 Photoacoustic Reporter Genes	
<i>1.7 Purpose of Thesis</i>	51
1.7.1 Rationale	
1.7.2 Hypothesis	
1.7.3 Overview of Studies	
<i>1.8 References</i>	54

Chapter 2: Intratumoral Distribution of Viable Cancer Cells over Time	82
2.1 <i>Introduction</i>	84
2.2 <i>Materials and Methods</i>	87
2.2.1 Lentiviral Construction and Production	
2.2.2 Cell Culture and Stable Cell Generation	
2.2.3 Immunofluorescence Staining	
2.2.4 Proliferation Assays	
2.2.5 <i>In Vitro</i> Luciferase Assays	
2.2.6 <i>In Vitro</i> Magnetic Resonance Imaging	
2.2.7 Orthotopic Tumour Model	
2.2.8 <i>In Vivo</i> Fluorescence and Bioluminescence Imaging	
2.2.9 <i>In Vivo</i> Magnetic Resonance Imaging	
2.2.10 Histology	
2.2.11 Statistics	
2.3 <i>Results</i>	97
2.4 <i>Discussion</i>	111
2.5 <i>References</i>	117
Chapter 3: Whole-body Tracking of Spontaneous Metastases on MRI	125
3.1 <i>Introduction</i>	127
3.2 <i>Materials and Methods</i>	130
3.2.1 Lentiviral Construction and Production	
3.2.2 Cell Culture and Stable Cell Generation	
3.2.3 <i>In Vitro</i> Bioluminescence Imaging	
3.2.4 Western Blot	
3.2.5 <i>In Vitro</i> Magnetic Resonance Imaging	
3.2.6 Spontaneous Metastasis Model	

3.2.7 <i>In Vivo</i> Bioluminescence Imaging	
3.2.8 <i>In Vivo</i> Magnetic Resonance Imaging	
3.2.9 Statistics	
3.3 <i>Results</i>	138
3.4 <i>Discussion</i>	150
3.5 <i>References</i>	153
Chapter 4: Detection of Viable Cancer Cells on Photoacoustic Imaging	159
4.1 <i>Introduction</i>	160
4.2 <i>Materials and Methods</i>	162
4.2.1 Cell Culture	
4.2.2 Lentiviral Production and Generation of Stable Cells	
4.2.3 Immunofluorescence Staining	
4.2.4 Proliferation Assays	
4.2.5 <i>In Vitro</i> Fluorescence Imaging	
4.2.6 <i>In Vitro</i> Photoacoustic Imaging	
4.2.7 <i>In Vivo</i> Fluorescence Imaging	
4.2.8 <i>In Vivo</i> Photoacoustic Imaging	
4.2.9 <i>Ex Vivo Fluorescence Imaging and Histology</i>	
4.2.10 Statistics	
4.3 <i>Results</i>	170
4.4 <i>Discussion</i>	183
4.5 <i>References</i>	188
Chapter 5 Summary and Future Work	194
5.1 <i>Discussion and Conclusions</i>	195

5.1.1 Chapter 2 Summary and Significance	
5.1.2 Chapter 3 Summary and Significance	
5.1.3 Chapter 4 Summary and Significance	
5.2 Challenges and Limitations	200
5.2.1 Sensitivity of Detection	
5.2.2 Unintended Effects on Biology by Reporter Genes	
5.2.3 Gadolinium Toxicity and Dose	
5.3 Future Work	207
5.3.1 Genetic Engineering Methods	
5.3.2 Manganese Probe for MR Imaging of <i>Oatp1b3</i> Expression	
5.3.3 Syngeneic Reporter Gene Systems	
5.4 References	211
Chapter 6 Appendices	218
6.1 Permissions	219
6.2 Curriculum Vitae	224

List of Tables

- p.35 1.1 Gyromagnetic Ratios of Various Atomic Species
- p.40 1.2 Relaxation Times of Common Tissues at 3 Tesla

List of Figures

p.5	1.1	The Tumour Microenvironment
p.12	1.2	The Invasion-Metastasis Cascade
p.30	1.3	Bioluminescence Imaging of Preclinical Animal Models
p.37	1.4	Transverse Decay and Longitudinal Restoration
p.45	1.5	Magnetic Resonance Imaging of <i>Oatp1</i> Expression <i>In Vivo</i>
p.48	1.6	Imaging Resolution vs Imaging Depth of Optic or Optic Modalities
p.98	2.1	Engineering Cells with a Multimodality Reporter Gene System
p.101	2.2	<i>In Vitro</i> Functional Characterization of Reporter Genes
p.104	2.3	<i>In Vivo</i> Bioluminescence Enhancement via <i>Oatp1a1</i>
p.106	2.4	<i>In Vivo</i> MR Signal Enhancement via <i>Oatp1a1</i>
p.109	2.5	<i>In Vivo</i> MRI of TNBC Tumours with Corresponding Histology
p.110	2.6	Pixelwise Analysis of <i>In Vivo</i> MR Intensity to <i>Ex Vivo</i> Fluorescence
p.139	3.1	Imaging Principle and <i>In Vitro</i> Reporter Gene Expression
p.142	3.2	Spin-lattice Relaxation Rates of <i>Oatp1b3</i> -engineered Cells at 3 Tesla
p.144	3.3	BLI and MRI at 3 Tesla of Spontaneous Metastases
p.148	3.4	Longitudinal Tracking of Metastasizing Cancer Cells via BLI and MRI
p.171	4.1	Cell Engineering and Characterization
p.174	4.2	<i>In Vitro</i> Fluorescence and Photoacoustic Imaging
p.176	4.3	<i>In Vivo</i> Fluorescence Imaging of Engineered Tumours
p.179	4.4	<i>In Vivo</i> Near-Infrared Spectral Photoacoustic Imaging
p.182	4.5	<i>Ex Vivo</i> Fluorescence Imaging

List of Abbreviations, Symbols, Nomenclature

B ₀	main external magnetic field
BLI	bioluminescent imaging
Bw	bandwidth
CCD	charge coupled device
CNR	contrast-to-noise ratio
CT	computed tomography
CTC	circulating tumour cell
DNA	deoxyribonucleic acid
DTC	disseminated tumour cell
EC	extinction coefficient
ECM	extracellular matrix
EMT	epithelial to mesenchymal transition
ER	estrogen receptor
FLI	fluorescent imaging
FLM	fluorescent microscopy
FLuc2	human-codon optimized firefly luciferase
FOV	field of view
Gd	gadolinium
GE	gradient echo
GFP	green fluorescent protein
H&E	hematoxylin and eosin
HER2	human epidermal growth factor receptor 2

ICG	indocyanine green
IP	intraperitoneal
IR	inversion recovery
IV	intravenous
MBC	metastatic breast cancer
MI	molecular imaging
Mn	manganese
MRI	magnetic resonance imaging
NEX	number of excitations
NMRD	nuclear magnetic relaxation dispersion
Oatp1	organic anion-transporting polypeptide 1
Oatp1a1	organic anion-transporting polypeptide 1a1
Oatp1b1	organic anion-transporting polypeptide 1b1
Oatp1b3	organic anion-transporting polypeptide 1b3
PAI	photoacoustic imaging
PET	positron emission tomography
PFA	paraformaldehyde
PM	precision medicine
PR	progesterone receptor
PSMA	prostate-specific membrane antigen
QY	quantum yield
R_1	spin-lattice relaxation rate
R_2	spin-spin relaxation rate

RF	radiofrequency
ROI	region of interest
SE	spin echo
SPECT	single photon emission computed tomography
SNR	sound-to-noise ratio
S _N 2	nucleophilic substitution reaction mechanism
T	tesla
T ₁	spin-lattice relaxation time
T ₂	spin-spin relaxation time
TE	echo time
TME	tumour microenvironment
TNBC	triple-negative breast cancer
TNM	tumour size, node status, metastasis staging system
TR	repetition time
US	ultrasound

CHAPTER 1 Introduction

The overarching goal of this thesis is to develop the *organic anion-transporting polypeptide 1* reporter gene system for non-invasive, longitudinal tracking of viable cancer cells in preclinical animal models. This introductory chapter provides an overview on known cancer mechanisms, clinical imaging methods, and preclinical approaches for studying cancer. Additionally, an overview of current methods in molecular imaging and in-depth background knowledge on the relevant modalities for this thesis, including bioluminescence imaging, magnetic resonance imaging, and photoacoustic imaging, will be provided. Background knowledge on organic anion-transporting polypeptides is also discussed to provide a baseline for its development as a multimodality reporter gene.

1.1 Motivation and Overview

Cancer is a heterogeneous group of diseases involving abnormal cell growth with potential to invade and spread to other parts of the body. Cancerous, or malignant, tumours are distinct from benign tumours, by their ability to spread throughout the body. Each year, over 14 million new cases of cancer are diagnosed, and approximately 10 million deaths result directly from cancer, comprising 15.7% of all annual deaths (1). Non-invasive imaging plays a critical role in the detection, staging, and monitoring of cancer in individual patients (2). The technologies used for this purpose encompass multiple modalities such as ultrasound (US), computed tomography (CT), magnetic resonance imaging (MRI), and positron emission tomography (PET). These technologies have also been applied for assessing cancer progression at the preclinical stage.

“Precision Medicine” (PM) increasingly shows greater promise than conventional “one-size-fits-all” traditional medicine with respect to patient outcomes, spurring the need for understanding the molecular features of cancer in individual patients, rather than its macroscopic features (3). Molecular imaging (MI) is a growing biomedical research discipline that enables the visualization, characterization, and quantification of biological processes taking place at both the cellular and subcellular levels within intact living subjects over time, including patients (4). As a small part of this larger effort, this thesis develops a reporter gene technology to image the viability of engineered cancer cells in preclinical animals at the primary tumour stage, as well as for noninvasive, longitudinal tracking of metastatic cancer cell dissemination throughout the entire body. Specifically, this thesis employs, characterizes and develops methods for using *organic*

anion-transporting polypeptide 1 (Oatp1) as a reporter gene for tracking of engineered cancer cells *in vivo* in preclinical animal models. We also discuss the potential utility of *Oatp1* reporter genes for future use in clinical cell tracking studies.

In Chapter 2, *Oatp1a1* was investigated for longitudinal imaging of primary triple-negative breast cancer tumours on magnetic resonance imaging (MRI) with concomitant enhancement of bioluminescence imaging (BLI) signals, and effectively demonstrated non-homogenous distributions of breast cancer cells within tumour masses. In Chapter 3, *Oatp1b3* was explored for tracking of metastasizing triple-negative breast cancer cells in preclinical animals on MRI, with simultaneous tracking of metastases with BLI. This collection of experiments demonstrated detection of the spread from primary orthotopic tumours to single lymph nodes via *Oatp1b3*-enhanced MRI, subsequent visualization of multi-lymph node spread, and finally detection of small metastatic lung lesions within the same animal over time.

In Chapter 4, *Oatp1b3* was additionally assessed for its ability to take up a fluorescent and photoacoustic contrast agent called indocyanine green (ICG), allowing for the establishment of *Oatp1b3* as a photoacoustic reporter gene for rapid, cost-effective imaging of engineered cells in localized tissues with concurrent high-contrast and resolution. Finally, Chapter 5 summarizes the conclusions and significance of this thesis, discusses its experimental limitations, and presents ideas for future work to build on the results presented in this thesis.

1.2 Modeling Cancer

1.2.1 Cancer Trends

In North America, one in every two women, and one in every three men will develop cancer in their lifetime (5). In general, when the cancer is caught when still confined to its tissue of origin, the main goal is to eradicate the tumour from the primary site and prevent distant metastasis via surgical resection, radiation, and/or systemic therapy (6). Prognosis is often hopeful at these stages, though notable exceptions exist (1, 7). At the primary site, the tumour has been demonstrated to comprise not only of cancer cells as one might expect. In fact, nonmalignant cells can account for approximately half of the tumour mass, in both primary and metastatic lesions (8) (**Figure 1.1**). These other components profoundly influence its progression and metastatic efficiency, and shape its therapeutic responses and resistance to treatment (9).

Direct targeting of non-cancer cells within the tumour microenvironment (TME) has contributed to positive therapeutic outcomes (10-12). These TME components include vascular endothelial cells, tumour-associated adipocytes, fibroblasts, lymphocytes, neutrophils, and macrophages, secreted factors and extracellular matrix (ECM) proteins (13). Once the cancer metastasizes, curative treatment becomes less likely. Unfortunately, many patients present with distant metastatic spread at their initial diagnosis (14). At that juncture, the goal often becomes prolonging the life of the patient and symptom palliation (6). And while metastatic disease accounts for the vast majority of cancer-associated deaths, this process remains the least understood aspect of cancer biology (15).

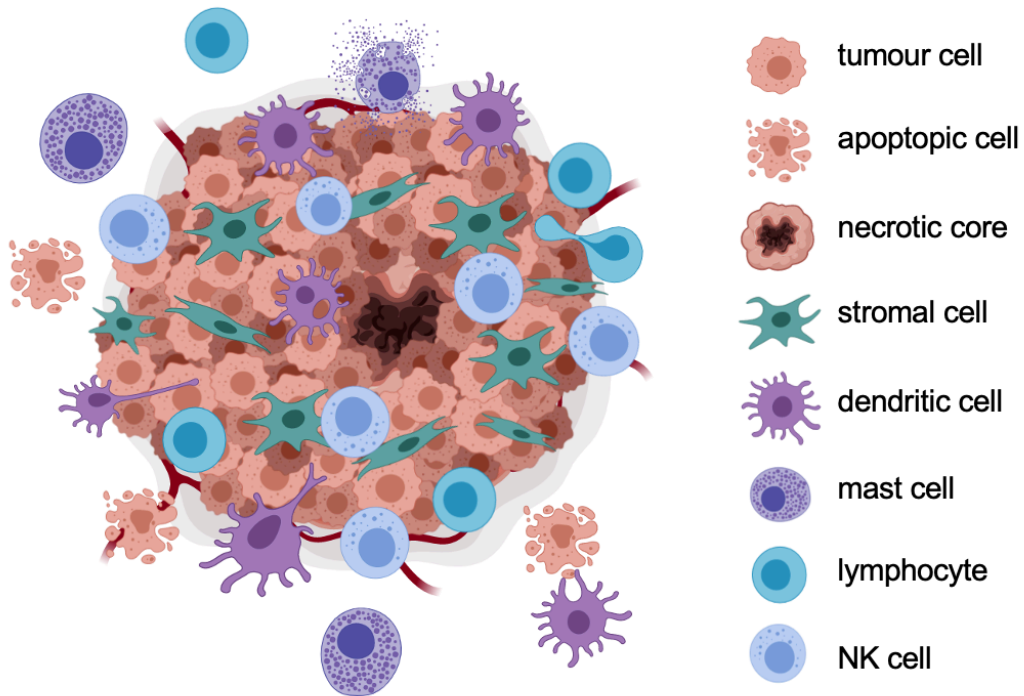


Figure 1.1. The Tumour Microenvironment. The tumour microenvironment is a complex ecosystem of heterogeneous tumour cells, stromal cells, and a variety of immune cells residing in a network of dysregulated vasculature and collagen. Poor perfusion and densely-packed glycolytic tumour cells create pockets of reduced oxygen or hypoxia, low pH, poor nutrient availability, anti-inflammatory cytokines, chemokines, and accumulated metabolic by-products, such as lactate. Tumour-infiltrating immune cells of both the myeloid and lymphoid lineages are found within the TME. NK, natural killer. This figure was drawn by Nivin N. Nyström.

1.2.2 Preclinical Animal Models in Oncology

Clinical research in oncology is largely limited to analytical or observational methods, for obvious ethical reasons, with therapy-focused clinical trials being the one exception to this rule. Preclinical animal models therefore offer an indispensable intermediate to clinical trials and reductionist *in vitro* research that fails to model the complexity of cancer progression at both early and late stages of the disease, including TME development and metastatic colonization (16). Preclinical animal models provide a platform to improve our understanding of underlying biological mechanisms in oncology, as well as a platform to test the initial efficacy of new treatment strategies, and have contributed to major breakthroughs, such as the first demonstration of immune checkpoint blockade (17).

In 2016, approximately two-thirds of published studies in oncology employed preclinical animal models in their methods, and immunodeficient mice constitute the vast majority of animals in these studies (16). Immunodeficient mice are required for xenografting of human cancer cells in order to avoid cancer rejection; although models using mice reconstituted with components of the human immune system, so called “humanized” mouse models, are being developed (18). Syngeneic immunocompetent models also exist using mouse-derived cell lines but these are less utilized for “proof-of-concept” imaging studies. The most common immunodeficient mouse strain used in oncology is the athymic nude mouse (57% of all studies), followed by the NOD scid gamma (NSG) mouse (24% of all studies).

Specifically, the athymic nude strain was generated from a spontaneous mutation of *Foxn1*, a transcription activator particularly important in thymic epithelium. This resulted in mice unable to develop their thymus gland, and in turn, a systemic depletion of T cells, and a decreased rejection rate of tumour cell engraftments relative to immunocompetent mice (19). Although their natural killer (NK) cell counts are low at birth, this metric increases with age, and their innate immunity remains intact. In contrast, NSG mice are far more immunodeficient than athymic nudes. Specifically, the NSG mouse model exhibits depletion of both T and B cells, a dysfunctional complement system, extremely low development of NK activity, and impaired innate immunity. As a result, NSG mice ultimately feature the highest tumour engraftment rates of all mouse strains and are highly permissive for metastasis (20).

1.2.3 Cancer Cell Lines and Tumour Initiation

There are different methods by which tumour growth can be initiated within a preclinical animal. These include environmentally-induced tumour models (6% of studies), genetically-engineered mouse models (24% of studies), and, most commonly, due to cost-effectiveness and time efficiency, cell implantation models (89% of studies) (16). This thesis focuses on cell implantation models of tumour initiation. Most studies using cell implantation methods for tumour initiation employ established cancer cell lines harvested from tumours in human patients or animals, that are subsequently propagated *in vitro* as a monolayer or *in vivo* as xenografts. The establishment of cell lines as a

scientific tool has an unfortunate history, clouded with racism and medical misconduct. The first cancer cell line, “HeLa,” was harvested in 1951 from Henrietta Lacks, an African-American cervical cancer patient from a poor socioeconomic background. Sampling of both her healthy tissue and cancer was performed, with the intention of culturing the specimens for laboratory research, without her knowledge or consent during her multiple visits to John Hopkins University (21). This was conducted despite the contemporary norm of obtaining consent at the time, which was propelled by the Nuremberg Code of 1947, and soon followed by the legal recognition and duty of “Informed Consent” in 1957 (see *Salgo v. Leland Stanford, Jr. University Board of Trustees*) (22).

It was another 30 years before the first widely-used breast cancer cell lines, the MD Anderson (MDA) series of cells, became established, which this thesis uses to model breast cancer *in vivo* (23). More recent breast cancer cell lines include the “SUM” series of cells derived from primary tumours, pleural effusions or various metastatic sites (24). Additionally, the murine-derived 4T1 cell line established by Miller *et al* in 1983, which is also used in this thesis, was isolated from a triple negative breast cancer, and is a widely-used metastatic breast cancer model (25, 26). Since innate and adaptive immunity have been demonstrated to play important roles in tumour growth and metastasis, a murine-derived breast cancer cell line, which can be grown in immunocompetent mice, represents an important tool for studying immune responses in cancer development (27, 28). Though there are known caveats to using any animal model (29, 30), cell lines remain powerful experimental tools. In many instances,

information generated from a study has translated to clinical benefit. For example, the discovery that anti-estrogens regulated growth of tamoxifen-stimulated MCF-7 cells led to development and trials of fulvestrant (Faslodex®, AstraZeneca Pharmaceutical LP, Wilmington, DE, USA), that is now regularly recommended for treatment of recurrent ER-positive metastatic breast cancer in menopausal women (31-34).

To establish a primary tumour with the cell implantation method, cells often are introduced ectopically, that is subcutaneously, or orthotopically, into the tissue that matches the tumour histotype. For breast cancer cells in mice, orthotopic implantation means a cell injection into one (or more) of four mammary fat pads. Orthotopic implantations of tumour cells have been extensively described to be superior with respect to modelling tumour microenvironmental interactions, therapeutic response and metastatic patterns, relative to ectopic implantations (35-40). After implantation, a host of cell types come together and actively interact with the implanted tumour cells to establish the TME. Depending on the immunocompetency of the mouse strain, these may include macrophages, fibroblasts, NK cells, neutrophils, decreases in local pH, and remodeling of the ECM (41).

1.2.4 Established Mechanisms of Metastasis

Metastasis accounts for about 90% of cancer related deaths (15). Though drastic improvements to survival have been shown for cancer at early stages, randomized clinical trials over a 30-year period have largely failed to show

sustained increases in survival for patients with metastatic disease (42). To target metastatic disease, a better understanding of the metastatic process is warranted, and this represents a major area of investigation for various cancer types. The dissemination of cancer cells from primary tumours and subsequent seeding of new tumour colonies into distant tissue involves a multi-step process known as the **invasion-metastasis cascade** (15) (**Figure 1.2**). Before the metastatic process can begin, the primary TME, that encompasses the tumour cells and the stroma in which they grow as well as the interactions between these two compartments, is established at the primary site (43).

The first step of the invasion-metastasis cascade is **(1) dissociation** of a single cancer cell from the primary tumour through epithelial-to-mesenchymal transition (EMT) or a collective of cancer cells in which some “leader cells” have undergone mesenchymal transition but carry epithelial-type cargo cancer cells along with them. The dissociated tumour cells infiltrate into the surrounding stroma and invade and migrate through the basement membrane supporting the endothelium of local blood and/or lymphatic vessels as the second step of the invasion-metastasis cascade called **(2) invasion**. It is worth noting that spread of tumour cells to nearby lymph nodes is an early and common event in patients, and the lymphatic vasculature is therefore considered as an important route of metastatic spread. It has been proposed that entry of cancer cells into the lymphatic vasculature might be facilitated by the higher permeability of lymphatic vessels relative to blood vessels and/or by the absence of a complete basement membrane barrier (44). Yet, the relative frequencies at which distal organ

metastasis occurs directly via lymphatics, or directly through the bloodstream, or indirectly from the lymphatic system to the bloodstream and then to the organ, are not fully understood.

Next, **(3) intravasation** occurs, whereby the dissociated tumour cells enter the hematogenous and/or lymphogenous vasculature after having successfully crossed through the extracellular matrix (ECM). In blood circulation, the tumour cells are referred to as circulating tumour cells (CTCs). In this phase, the bloodstream represents a hostile environment for CTCs, exposing them to rapid clearance by natural killer cells or fragmentation due to the physical stresses encountered in transit through the circulation. The dissociated tumour cells are distributed to remote organs by blood or lymphatic flow and actively leave the vasculature via **(4) extravasation**, at which point they are referred to as disseminated tumour cells (DTCs). Having traveled far from the primary tumour, DTCs find themselves in a new microenvironment devoid of familiar stromal cells, growth factors, and ECM constituents that previously sustained the viability of their predecessors in the primary site (45). DTCs may reside within their newfound organ in a non-proliferative state for many months or even years in a phase known as **(5) dormancy**. Finally, the growth of an overt metastatic colony represents the concluding and most deadly phase in the malignant progression of a tumour.

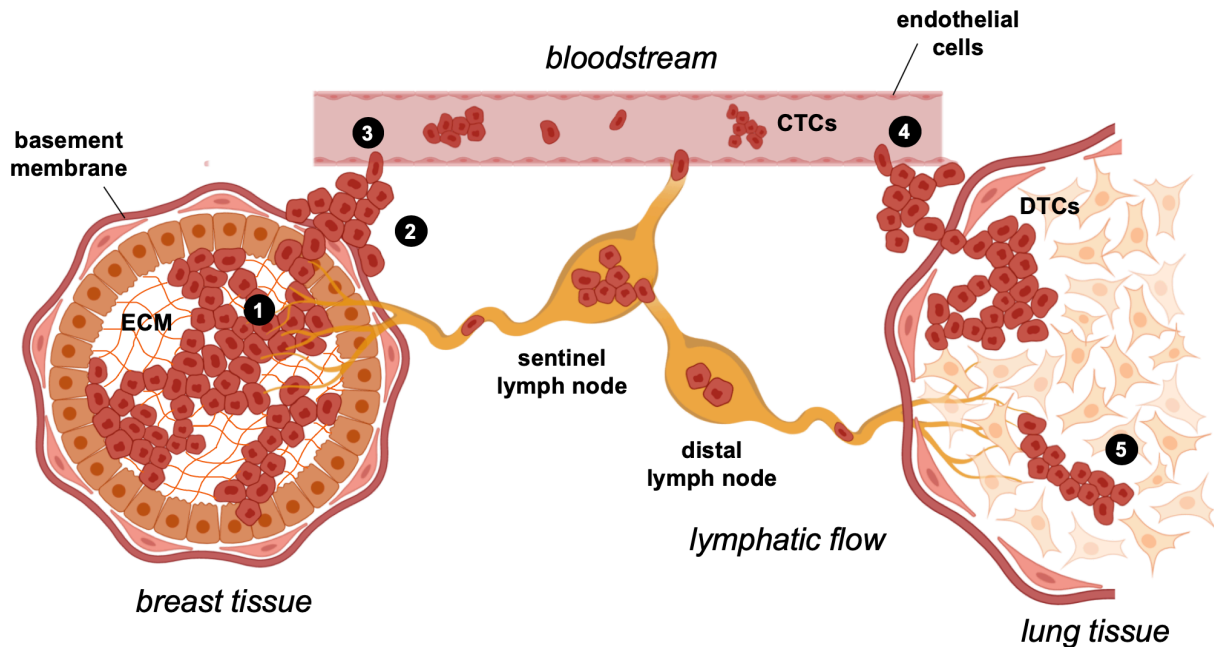


Figure 1.2. The Invasion-Metastasis Cascade. (1) Epithelial to mesenchymal transition (EMT) results in dissociation of the breast cancer cell from the primary tumour. (2) Invasion of the dissociated tumour cell through the extracellular matrix (ECM) and basement membrane of the primary site. (3) Intravasation of the dissociated tumour cell into the bloodstream, or alternatively, into the lymphatic system. At this point, the dissociated tumour cell is deemed to be a circulating tumour cell, CTC. (4) Extravasation of the CTC from the bloodstream into the target tissue such as the lungs, at which point, the tumour cell is called a disseminated tumour cell (DTC). (5) The DTC remains in a non-proliferative state at the metastatic site for some time, a phase called dormancy, and may or may not enter a proliferative state at a later time. This figure was drawn by Nivin N. Nyström.

1.2.5 Modeling Metastatic Disease

Metastasis accounts for about 90% of cancer-related deaths (15). Yet, approximately 75% of studies employing preclinical animal models focus only on the primary tumour and do not include the study of metastasis (16). Even more, investigators in these studies largely use rudimentary measurements such as primary tumour growth curves and tumour mass as study readouts to estimate therapeutic response (16). In fact, many preclinical studies are limited to simple end point readouts such as tumour weight, tumour volume or survival. While these are clinically important parameters, end point readouts neglect the temporal kinetics of tumour growth and metastatic progression. It is therefore unsurprising that survival rates for patients diagnosed with metastatic disease have not improved for breast cancer (42), as well as several other types of cancer (46, 47). The low success rate of clinical trials in oncology warrant a change in the approach taken to identify and assess new therapies (48).

To model metastatic disease in preclinical animal models, cells can be injected via the intravenous, intracardiac, or intrasplenic routes to generate reliable metastases within lung, brain, or liver tissue, respectively (49). These are referred to as experimental metastasis models because they recapitulate metastatic colonization but circumvent the primary disease. The most comprehensive way to study the entire metastatic cascade in preclinical animal models is orthotopic tumour cell implantation to induce the development of a primary tumour followed by spontaneous cancer cell metastasis to other parts of the body (16). These spontaneous metastasis models recapitulate the entire

invasion-metastasis cascade for more precise modeling of tumour progression. However, spontaneous models are used much less often than experimental metastasis models due to a longer experimental timeline, and unpredictable outcomes (49). For instance, it is difficult to determine, exactly and absolutely, where the metastasizing cells colonize and patterns may differ from mouse to mouse. In summary, preclinical evaluation of metastasis is challenging, but necessary to expand knowledge on the metastatic process and test therapies targeting metastatic disease.

1.3 Molecular Imaging

1.3.1 Imaging Cancer in Patients

Imaging technologies play a critical role in the diagnosis of cancer. While primary diagnostic tools include ultrasound (US) and computed tomography (CT), other modalities such as magnetic resonance imaging (MRI) and positron emission tomography (PET) have seen increasing use and have overall demonstrated better detection and staging of disease (50). For example, PET imaging of prostate-specific membrane antigen (PSMA) for prostate cancer staging shows increased specificity and sensitivity compared to standard imaging protocols, enabling personalized treatment planning and improved outcomes (51). And while US-guided prostate biopsy exhibits true positive detection rates of 10–19%, this increases to 59% for multiparametric MRI-guided biopsies (52).

Imaging is also playing an increasingly important role in monitoring treatment delivery and treatment response (53). For instance, imaging therapy response in gastrointestinal stromal cancer patients with 2-deoxy-2-[¹⁸F]-fluoroglucose (¹⁸F-FDG) PET allowed for determination of patient response status only 8 days after the start of treatment, compared to 8 weeks for CT, thereby offering the opportunity to provide salvage therapies for non-responders before the cancer has a chance to progress (54). Though costs of providing advanced imaging technologies for cancer diagnosis, staging and monitoring have deterred widespread utility, their usage is cost-effective with respect to life-year gains, and have been shown to offset costs via rapid determination of effective personalized treatments (55, 56).

1.3.2 Molecular Imaging of Cancer

Clinical imaging for abnormalities at the macroscopic scale is sensitive but unspecific (57). To address these limitations, the motivation for molecular imaging (MI) is to translate highly informative *in vitro* and *ex vivo* bioassays to an *in vivo* or *in situ* setting, an approach which has strong roots in nuclear medicine but is rapidly emerging in other modalities (58). While *in vitro* and *ex vivo* techniques provide valuable insight into innerworkings of cells and biochemistry of disease, they are limited by an inability to provide spatiotemporal information over entire intact organisms, making it difficult to appreciate the “full picture” of disease states and/or biochemical processes.

Additionally, the need to remove a tissue sample from its natural environment and process it renders results not accurate of true *in vivo* physiological conditions. Further, destruction or irreversible processing of tissue makes each sample useful for a small number of *in vitro* protocols, which may limit the information that could possibly be extracted per sample. Finally, the need to euthanize animals for *ex vivo* protocols makes longitudinal studies of the same animal impossible, and creates issues with respect to both increased costs and inter-subject variability (59).

To visualize, quantify, and monitor cell populations over time, one of three approaches may be taken: 1) development of an imaging probe that targets biomarkers on cells and/or pathways of interest, 2) pre-loading cells of interest with a contrast agent and subsequently introducing them into the biological system, and 3) engineering cells with a reporter gene *in vitro* or *ex vivo* and

subsequently introducing them into the biological system, or engineering them with a reporter gene *in situ*. Each of these methods has its strengths and limitations, which will be discussed in detail in **Sections 1.3.3, 1.3.4, and 1.3.5**, respectively.

Further, each of these methods can be employed on various imaging modalities. Likewise, each of these modalities also presents with its own set of strengths and disadvantages, and its effective application depends greatly on the details of the disease and/or biochemical process of interest. The relevant imaging modalities for this thesis, which include bioluminescence imaging, magnetic resonance imaging, and photoacoustic imaging, will be thoroughly reviewed in **Sections 1.4, 1.5, and 1.6**, respectively.

1.3.3 Targeted Molecular Probes

The development of targeted molecular probes is perhaps the most obvious approach for MI. These include a broad range of categories, including small molecules, peptides, aptamers, relatively high-molecular-weight antibodies, engineered protein fragments, and nanoparticles. Each type of agent falls within a different size range and thus possesses distinct pharmacokinetic and binding properties (59). In general, the objective of a molecular probe is to effectively target a specific biomarker *in situ* and generate significant signal above background for detection and image generation. In general, there are two main mechanisms by which a targeted probe may function: 1) probes that bind specific

receptors, transporters, or ion channels, (60) and 2) probes that enable imaging of metabolism, enzymatic activity, and/or transport (61).

The main advantage of targeted molecular probes is the ease of their translation into human patients, relative to all other MI approaches, once safety and effectiveness has been demonstrated. Their limitation, however, is the time and expense required to create a new molecular probe for each biological marker (62). Additionally, the targeting mechanism of the probe may activate or inhibit its target, which may cause undesired effects on the biochemical process being studied, especially if binding is irreversible, although this is less of a concern for modalities requiring biologically-negligible probe concentrations like PET (63).

On the other hand, probes that target metabolism, enzymatic activity, and/or transport such as hyperpolarized carbon-13 pyruvate for MRI and ^{18}F -FDG for PET can be used to image a generic process, *e.g.* all cancers exhibit increased pyruvate to lactate metabolism due to the Warburg effect, but this does not allow for identification of specific molecular biomarkers for each individual cancer patient (64). Further, specificity may be limited because other non-related pathologies *e.g.* non-oncogenic inflammation, can exhibit similar changes in metabolism (65); however, new metabolic probes for hyperpolarized carbon-13 MRI are being developed for increased cellular specificity (66-68).

1.3.4 *Ex Vivo* Cellular Loading

Cells can also be tracked by direct labelling via *in vitro* or *ex vivo* incubation with a contrast agent prior to their introduction or re-introduction into

the biological system, respectively. Examples of *ex vivo* cell loading approaches include indium-111 for imaging of white blood cells in patients with PET (69), iron-oxide nanoparticles for MRI of cancer cells in preclinical animal models (70), and gold nanoparticles for PAI (71) and/or CT (72). This approach allows for sensitive and specific determination of the location of labelled cells for a limited time after their introduction into the body (73).

While cellular loading is clinically relevant for immune cells in patients, it is limited to preclinical animal models for tracking of diseased cells, *e.g.* it is unethical to (re-)introduce labelled cancer cells into a patient. After their introduction into the biological system, the number of contrast agent molecules per cell declines over time due to its diffusion out of the cell and/or dilution due to cell division (74). This is a significant limitation for tracking proliferative cancer cells in preclinical animal models, such as during the initial establishment of a primary tumour, prior to their spontaneous spread to other parts of the animal.

On the other hand, some groups have taken advantage of the “dilution-with-division” effect in cellular loading and used this method to study the dormancy phase of cancer cells in experimental metastasis models (75, 76). Some cells types are not extensively proliferative, like stem cells, and these have been monitored using iron oxide nanoparticles and MRI with success (77). A second limitation of cellular loading is that the contrast agent molecules can also be engulfed by other cells once the initially loaded cells have died, *e.g.* macrophages can ingest particles via phagocytosis, thereby generating false positive signals in absence of the cells of interest (74). These limitations for *in*

vitro or *ex vivo* labelling of cells, largely restrict the timeframe in which cells of interest can be accurately detected and identified using *in vitro* or *ex vivo* direct labelling (78). Further, considerations must be taken with the effects of foreign particles packed into cells on normal cellular function. Ideally, the contrast agent used for labelling would remain inert, but this is not always the case. For example, cancer cells labelled *in vitro* with iron oxide nanoparticles and subsequently introduced into preclinical animal models exhibited reduced rates of growth due to pro-inflammatory effects caused by the labelling agent (79).

1.3.5 Reporter Genes

Reporter genes are functional pieces of deoxyribonucleic acid (DNA) that encode detectable proteins. Unlike traditional contrast agents, they can be fused to a gene of interest at the DNA-level to track the protein product across time and space at sub-cellular resolutions, or alternatively, the reporter can be placed under equivalent regulatory control to the gene of interest to indirectly track its spatiotemporal expression at the supra-cellular level. Green fluorescent protein, pioneered by Drs. Osamu Shimomura, Martin Chalfie and Roger Y. Tsien, became so widely used in biomedical research that it was subject of the 2008 Nobel Prize in Chemistry. The means by which scientists employ reporter genes can become quite complex to provide detailed information on highly specialized processes, *e.g.* determination of stem cell differentiation status (80), resonance transfer methods for detection of protein-protein interactions (81, 82), genetic circuitry to image cell-cell interactions (83), fluorescent barcoding of cells to track

cellular ancestry (84), but ultimately, reporter genes are used as a protein-based detection mechanism to track and monitor the fates of live cells in tissues.

Recently, reporter genes have become of particular interest for development and clinical management of gene and adoptive cell therapies in patients, which represents a revolutionary form of treatment for a number of diseases (85-88).

Reporter genes and other genetic material can be introduced into cells in a number of ways (89). In this thesis, the primary method of delivering genetic material to the cell is through the utilization of lentiviruses, a technique first described by Dr. Didier Trono's group at the Salk Institute in 1996 (90). Lentiviral vector systems typically consist of three separate plasmids: the packaging, envelope, and transfer plasmids. Briefly, the packaging plasmid includes a set of genes, including *gag* and *pol* that encode the major structural polyprotein required for assembly of the viral capsid, and the reverse transcriptase required for the integration of the genetic material of the virus into the host genome (91). The envelope plasmid includes the *env* gene, which ultimately encodes the viral spike protein, important in dictating the tropism of the virus (92). Finally, the transfer plasmid encodes the transgene of interest, flanked by viral long terminal repeats (LTRs) that facilitate viral packaging and host genome integration (93). Following co-transfection of these plasmids, packaging cells such as the 293T cell line release transgene-containing lentiviral particles into the media, which could then be collected for experimental use.

In MI, reporter genes overcome several limitations presented by targeted probes and cellular loading approaches, and as a result, have increasingly been

utilized in the literature at the preclinical stage (94). Once a reporter gene is established to work in one cell type, it can generally be used as a universal tool to track any gene of interest, unlike targeted probes that need to be newly designed for each biomarker. If scientists opt to integrate the reporter gene into the genome of a target cell, its DNA sequence then replicates with cell division; thus, its expression and subsequent detection depends only on the genetic regulation employed in the study, independent of cell division. Importantly, after the engineered cell dies, the DNA encoding the reporter is destroyed and its contrast mechanism cannot be transferred to bystander and/or phagocytic cells, unlike contrast agents used for cellular loading.

However, reporter gene contrast mechanisms also do present with some shortcomings. For example, reporter genes have decreased sensitivity relative to *ex vivo* cellular loading approaches (59). Additionally, while reporter genes are highly useful for tracking protein entities *in vivo*, tracking of non-protein small molecules in the body with genetically-encoded reporters becomes complicated and is better suited for targeted probe approaches (95). Nonetheless, since green fluorescent protein was first established, reporters for various modalities have been developed, including bioluminescence imaging (96-100), photoacoustic imaging (101), positron emission tomography (102-104), magnetic resonance imaging (105-110), and ultrasound (111). Traditionally, cells would be engineered *in vitro* or *ex vivo*, similar to cellular loading, but new methods are emerging for genetic engineering of target cells *in situ* (112-114).

1.3.6 Multimodality Imaging

It is important to recognize that all molecular imaging modalities have advantages as well as inherent limitations. Multimodality imaging allows researchers to combine different imaging datasets to gain a more complete understanding of the biology being studied. The most widespread application of multimodality imaging is the integration of PET, which allows for sensitive detection of probe activity, with computed tomography that provides detailed anatomical images of internal structures, thereby allowing clinicians and researchers to determine the three-dimensional (3D) locations of radiotracers (115). Within the last decade, PET/MRI has been increasingly commissioned at research centres, to combine functional information from PET, with structural and additional functional information from MRI for ultimate high sensitivity, high specificity, and high resolution molecular imaging (116).

Beyond PET, researchers are combining other modalities and molecular imaging approaches at the preclinical stage to better understand disease pathogenesis in terms of the interplay between different cell types, to identify putative mechanisms of disease and/or to evaluate the efficacy of new candidate treatments. For example, in studying the biology of cancer cell dormancy, a phenomenon that is increasingly being recognized as a hallmark of metastatic disease (117), Parkins *et al.* combined cellular loading of iron oxide nanoparticles for MRI with BLI of luciferase expression to detect viable cancer cells arrested into the brains of mice after systemic administration (118). Iron oxide nanoparticles allowed for high resolution 3D imaging of single cells with detailed

anatomical context, but provided no information on the viability of the cancer cells; *i.e.* hypointense signals on MRI may be stemming from uncleared particles even after cancer cell death or, alternatively, from microglia that have engulfed the nanoparticles as well as other unrelated sources of reduced MRI signal. Adding BLI to their protocol allowed for viability measurements of engineered cancer cells within brains of mice, confirming the presence of live cancer cells. Other studies have utilized various combinations of modalities, which ultimately serve to clarify or further experimental findings (119, 120). In the development of *Oatp1* as a reporter gene in this thesis, complementary modalities are used in combination primarily to confirm reporter gene activity *in vivo*, *e.g.* bioluminescence as a reference for reporter gene activity on MRI, ultrasound with photoacoustics for anatomical context. The sections below introduce the imaging modalities relevant to this thesis and include detailed discussions on established reporter genes for each modality.

1.4 Bioluminescence Imaging

1.4.1 Reporter Gene Development

Bioluminescence is a specific form of chemiluminescence whereby light is produced and emitted from biological organisms. This process occurs widely in marine vertebrates and invertebrates, as well as in some fungi, microorganisms, including some bioluminescent bacteria, and terrestrial arthropods such as fireflies (121). The principal reaction in bioluminescence involves the oxidation of a molecule called the “luciferin” via an enzyme, called the “luciferase.” The luciferase may require other cofactors, such as calcium or magnesium ions, and/or the energy-carrying molecule adenosine triphosphate (ATP), in order to perform the oxidation (**Equation 1.1**).

Equation 1.1. Biological oxidation of D-luciferin by firefly luciferase.



In firefly luciferase, the oxygen of the C₄ carboxyl end group on luciferin acts as a strong nucleophile and attacks the electrophilic phosphorous in the α-position within ATP in an S_N2 displacement (122). Inorganic pyrophosphate (PPi) is removed as the leaving group, resulting in an enzyme-bound intermediate, luciferyl-adenylate (123). The acidity of the C₄ carbon is increased in its new bond to AMP, allowing for its deprotonation, and carbanion formation (124). At this step, the carbanion, as a nucleophile, will then tend to attack molecular oxygen, thus generating a high-energy intermediate, the luciferin dioxetanone

(125, 126). Finally, dioxetanone spontaneously decarboxylates to form oxyluciferin (127). The resulting molecule, oxyluciferin, is in a singlet excited state, and its decay to the ground state releases a photon (128). Throughout the reaction, the Mg^{2+} shields the negative charges and influences the conformation of the phosphate groups (129).

In the laboratory, luciferase-based systems are used as reporter genes for biomedical research purposes. Work on luciferase as a reporter gene system first began in 1982 when Belas *et al.* isolated and expressed luciferase genes from marine bacteria in *E. coli* (130). The most widely used luciferase reporter gene today, firefly luciferase, was first cloned and expressed in *E. coli* by De Wet *et al.* in 1985 (131), expressed in mammalian cells just two years later in 1987 by Keller *et al.* (132), and used to image cells of interest in mammalian hosts in 1995 by Contag *et al.* (133).

1.4.2 *In Vivo* Image Generation

Current methods to generate bioluminescence imaging data with live animals first involves generation of stable Firefly luciferase-expressing cells and subsequent implantation of these cells into animals. The animal would then typically receive intraperitoneal administration of D-luciferin, after which, the substrate diffuses into surrounding organs and, thereafter, is carried away by capillary blood or lymph within those tissues. Evidence suggests that D-luciferin diffuses slowly and passively across cell membranes to enter the cytoplasm where the luciferase protein would be present within engineered cells (134). A

broad spectral distribution of light peaked at a wavelength of 560 nm is emitted following relaxation of excited oxyluciferin to its ground state (135). Light emission from constitutively expressed luciferase is proportional to tumour cell burden, and photon emission increases as the cell population multiplies (136).

Kinetic PET studies with radiolabeled ^{14}C -D-luciferin revealed generally low brain uptake likely due to presence of the blood brain barrier, high intestinal uptake due to the intraperitoneal route of injection, and predominant renal excretion of the luciferase substrate (137-139). Depending on the model, the signal from *in vivo* bioluminescence generally peaks 10 to 15 minutes post-administration of D-luciferin, after which signals plateau and eventually drop as the substrate is renally excreted. The bioluminescent reaction between the luciferase enzyme and its substrate produces low-intensity light that ordinarily cannot be seen with the human eye or by conventional microscopy (121).

A specialized imaging detector is required, especially when imaging cells within preclinical animal models, as light scattering and light attenuation from surrounding tissues further obscure the spatial location of the signal source. The most common system for imaging bioluminescence *in vivo* comprises of a light-tight imaging chamber into which the anesthetized subjects are placed onto a heated stage. A bright-field photograph from the top of the black chamber is first taken of the subject as a spatial reference, after which a sensitive charged-coupled device (CCD) camera is used to detect and spatially localize the bioluminescent photons. The CCD is super-cooled to approximately -90°C to minimize thermal noise and increase exposure times, thereby increasing its

ability to detect very low levels of light (140). The units of measurement for bioluminescence signals can include counts measured in photons (p), total flux (p/s), or average radiance (p/s/cm²/sr). Total flux is generally used to calculate total tumour burden for an animal, whereas average radiance can be utilized to measure individual bioluminescence signals from a specific region of interest (141).

1.4.3 Applications for Cancer Research

There are several advantages of bioluminescence imaging that make it a useful modality for cancer research. Before bioluminescence imaging was established, the default method by which preclinical scientists could dynamically track tumour progression was with simple readouts such as caliper measurements, which are not feasible for measuring tumour growth or metastatic burden in deep tissues. More extensive measurements could be made posthumously, by either staining tissue for cancer cell markers or by imaging histology with confocal microscopy for fluorescent reporter gene expression. These histological methods, require extensive and time-consuming tissue preparation and provide information only at endpoint. Further, this preparation meant that only *ex vivo* tissues could be observed, giving a static picture of gene expression and/or cellular location, with the exception of translucent, non-mammalian model organisms *e.g. C. elegans, D. rerio* (142).

For longitudinal imaging in mammalian models with these previous methods, studies needed to overcome inherent inter-subject variability at each

timepoint. Thus, large numbers of animals would need to represent different timepoints for a methodical understanding of the biological phenomenon being studied. However, bioluminescence imaging allows for whole-body imaging without euthanasia, offering a tool to longitudinally track the protein and/or cell of interest in an individual animal over time, which greatly reduces the number of animals needed to understand a hypothesis or effect (143). In addition, mammalian systems do not naturally produce bioluminescence signals, so luciferase-expressing cells in preclinical animal models generate sensitive imaging data due to an inherently high contrast-to-background ratio. Bioluminescent imaging has therefore become a critical tool in preclinical oncology research. In recent years, the luciferase reporter gene has been used to track the expression of specific oncoproteins (144-147), model metastatic progression (148-150), and assess the delivery, biodistribution, and/or efficacy of new candidate therapies (151-153).

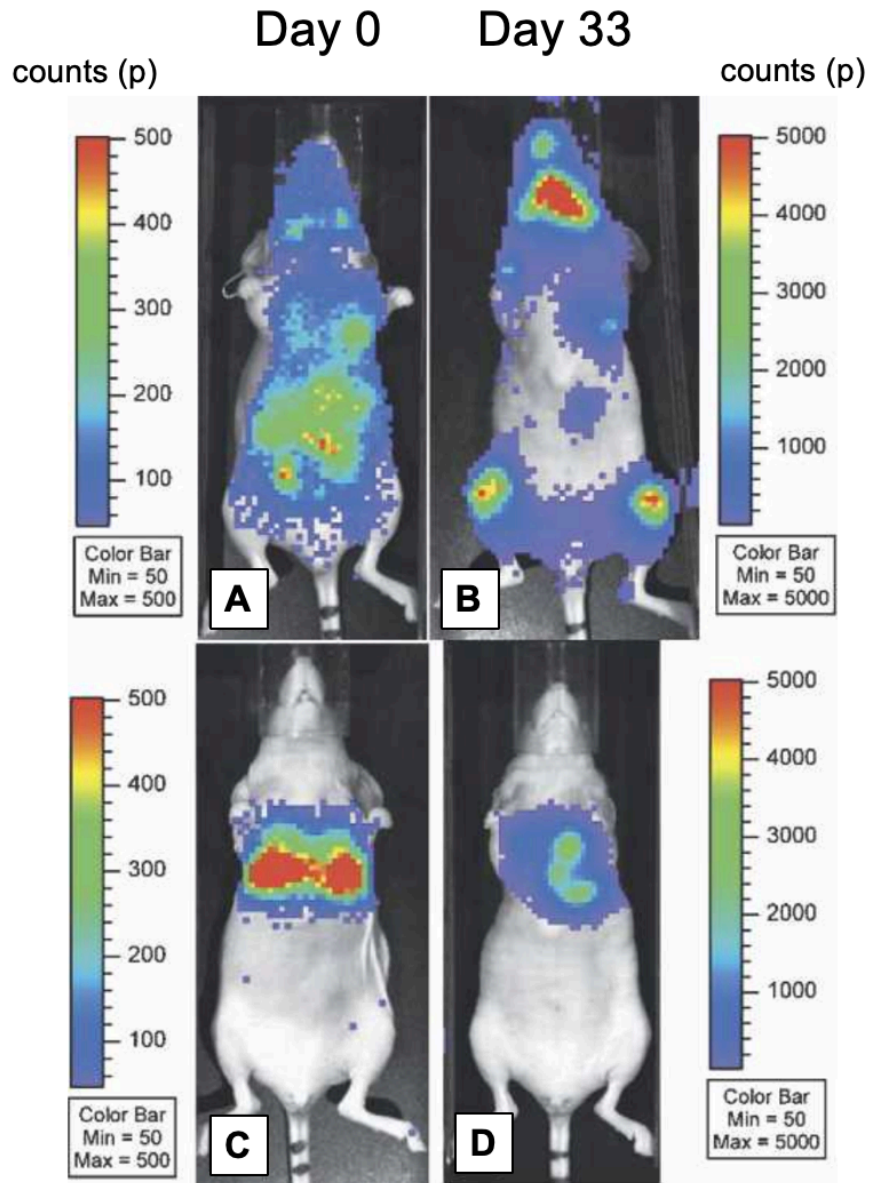


Figure 1.3. Bioluminescence Imaging of Preclinical Animal Models.

Bioluminescence imaging measurements in counts (photons) of 2×10^5 luciferase-expressing MDA-MB-435 cells immediately (A,C) or 33 days (B,D) after injection into the left (A,B) or right (C,D) ventricle. A 120-second acquisition was taken for Day 0 images (A,C); Day 33 images required only a 10-second duration (B,D). This figure was acquired from Zinn *et al.* (154).

1.4.4 Limitations of Bioluminescence Imaging

The ultimate goal of molecular imaging for cancer research is to detect cancer-associated molecular events as they occur within a biological system. Bioluminescence imaging provides a unique platform to track these events with high sensitivity and robustness, but light attenuation and light scattering from surrounding tissues limit the depth of detection and resolution of imaging, making it difficult to determine the precise location of the source of signal (155). A small number of superficial cells and a large number of deep-seated cells generate similar signals, which is particularly problematic when researching metastatic spread in preclinical animal models. A photograph or X-ray image overlaid on bioluminescence data, as is de rigueur on current imaging systems, can only qualitatively approximate the possible source location. Additionally, tissue scattering of bright sources of light emitted from larger tumours adjacent to weaker regions of light emission *i.e.* smaller metastases, may obscure the presence of smaller tumours or metastases in bioluminescence imaging, which may only become apparent during histological evaluation if the corresponding tissue is sampled (156).

Furthermore, imaging of larger animal models, and even humans, would be challenging as light attenuation from surrounding tissues would completely obscure any signals deeper than a few centimeters within the body of the subject (157). New image acquisition systems offering bioluminescence tomography have recently been developed, to generate multi-projection datasets overlaid onto CT images, but the long acquisition times and increased costs of these

systems counter some of the original benefits of bioluminescence imaging – its high throughput and cost-effectiveness (158). Complicating factors also exist with respect to the biochemical effects of luciferase expression on the biological system being studied; during imaging, ATP-dependent luciferases become a significant metabolic burden, and have been demonstrated to decrease ATP availability by a factor of two (159), which may have effects on the ability of the tumour to grow and progress. Along the same lines, metastasis has been shown to be seriously debilitated in murine breast cancer models when cells are engineered with luciferase, all things being equal (160). Reporter gene design requires relative inertness, and while its expression may not seriously alter the parameters of the study, the undesired effects of synthetic luciferase activity on the biological system should be acknowledged to some extent.

1.5 Magnetic Resonance Imaging

1.5.1 Magnetic Resonance Imaging in Medicine

Magnetic resonance imaging (MRI) is a versatile technology used to non-invasively acquire an increasing variety of imaging data. In addition to anatomy, images of physiological processes of the body can also be achieved (65). Proton (^1H) MRI, which represents the vast majority of scans acquired, and the imaging performed in this thesis, is largely used to identify disease on a macroscopic scale, such as a solid tumour. MRI also has potential for detection of events at the molecular scale, with high resolution 3-dimensional spatial information and surrounding anatomical context. The following sections provide a brief overview of the fundamental processes involved with generating a proton image. The information below is obtained from a combination of sources: *Magnetic Resonance Imaging: Physical Principles and Sequence Design*, Second Edition (2014), *MRI from Picture to Proton*, Third Edition (2017), and *MRIquestions.com* (2020), unless otherwise referenced.

1.5.2 Nuclear Magnetic Resonance

MRI was originally known as NMRI, “nuclear magnetic resonance imaging,” but the adjective, “nuclear” was dropped to avoid negative connotations wrongly associated with radiation exposure (161). Atomic nuclei possess an intrinsic property known as **spin** angular momentum (I , $\text{kg}\cdot\text{m}^2\cdot\text{s}^{-1}$) that interacts with electromagnetic fields. The particle is not actually spinning. Rather, like mass, spin is a fundamental property and does not arise from more

basic mechanisms. Spin angular momentum is quantized into integer or half-integer units e.g. ^1H has $I = \frac{1}{2}$. Only nuclei with non-zero spins ($I \neq 0$) can interact with electromagnetic fields and precess around the axis of an applied external magnetic field. The magnetic moment, $\vec{\mu}$ ($\text{A}\cdot\text{m}^2$) quantifying the interaction of the nuclei with this field is given by **Equation 1.2**.

Equation 1.2. The gyromagnetic ratio of an atomic species.

$$\vec{\mu} = \gamma \cdot \vec{I}$$

The proportionality constant, γ is known as the gyromagnetic ratio, which is unique for every nuclear isotope (**Table 1.1**). The nuclear magnetic dipole moment experiences a torque in the external magnetic field, B_0 which causes the dipole moment to precess around the field direction at a specific frequency known as the Larmor frequency, f_0 (**Equation 1.2**).

Equation 1.3. The Larmor Equation.

$$f_0 = \gamma \cdot B_0$$

When an animal or human is placed in the scanner, the distribution of cones of precession of the ensemble of spins becomes skewed towards the field direction, resulting in a net longitudinal equilibrium magnetization. This longitudinal magnetization is manipulated by application of additional alternating magnetic fields producing signal for magnetic resonance imaging.

Nucleus	$\frac{\gamma}{2\pi}$ (MHz·T ⁻¹)
¹ H	42.58
² H	6.536
³ H	45.42
³ He	-32.43
⁷ Li	16.55
¹³ C	10.71
¹⁴ N	3.077
¹⁵ N	-4.316
¹⁷ O	-5.772
¹⁹ F	40.05
²³ Na	11.26
²⁷ Al	11.10
²⁹ Si	-8.465
³¹ P	17.24
⁵⁷ Fe	1.382
⁶³ Cu	11.31
⁶⁷ Zn	2.669
¹²⁹ Xe	-11.78

Table 1.1. Gyromagnetic Ratios of Various Atomic Species. Nuclei and their corresponding gyromagnetic ratio, measured in MHz/T. Note that some species have negative gyromagnetic ratios, which results in an opposite precession direction.

We can see from **Table 1.1** that among common nuclear isotopes, ^1H has the highest gyromagnetic ratio, dictating that it has the highest precession frequency and, as a result, is the most “MR visible” nucleus. The Larmor equation also dictates that larger magnetic fields generate higher precessional frequencies. In a 1.5T field, the resonance frequency of ^1H would be $(42.58 \text{ MHz/T}) \cdot (1.5\text{T}) = 63.87 \text{ MHz}$. At 3.0T, the resonance frequency would be twice as large, or 127.74 MHz. For MRI, the net magnetization (\vec{M}) is a useful term to describe the vector sum of individual spins, \vec{I} obtained from millions of nuclei placed in an external field. \vec{M} can be displaced from its equilibrium state (\vec{M}_0) along the direction defined by B_0 through the application of a radiofrequency (RF) pulse, B_1 . This alternating magnetic field oscillates in a plane transverse to the static field at the Larmor frequency of the nuclei of interest *e.g.* ^1H . The application of B_1 produces a torque on \vec{M}_0 causing it to be tipped into the transverse plane and precess at the Larmor frequency around the external field. Following the RF excitation, the net magnetization returns to its equilibrium state according to the longitudinal (T_1) and transverse (T_2) relaxation times (**Figure 1.4**). The T_1 relaxation time (and its inverse rate, R_1) characterizes the re-growth of $|\vec{M}|$ along the direction of the B_0 field. This occurs through the transfer of energy from the excited nuclei to the lattice and is called spin-lattice relaxation for this reason. The T_2 relaxation time (and its inverse rate, R_2), referred to as spin-spin relaxation, characterizes the exponential decay of the excited magnetization, M_{xy} within the transverse plane through transfer of energy between spins.

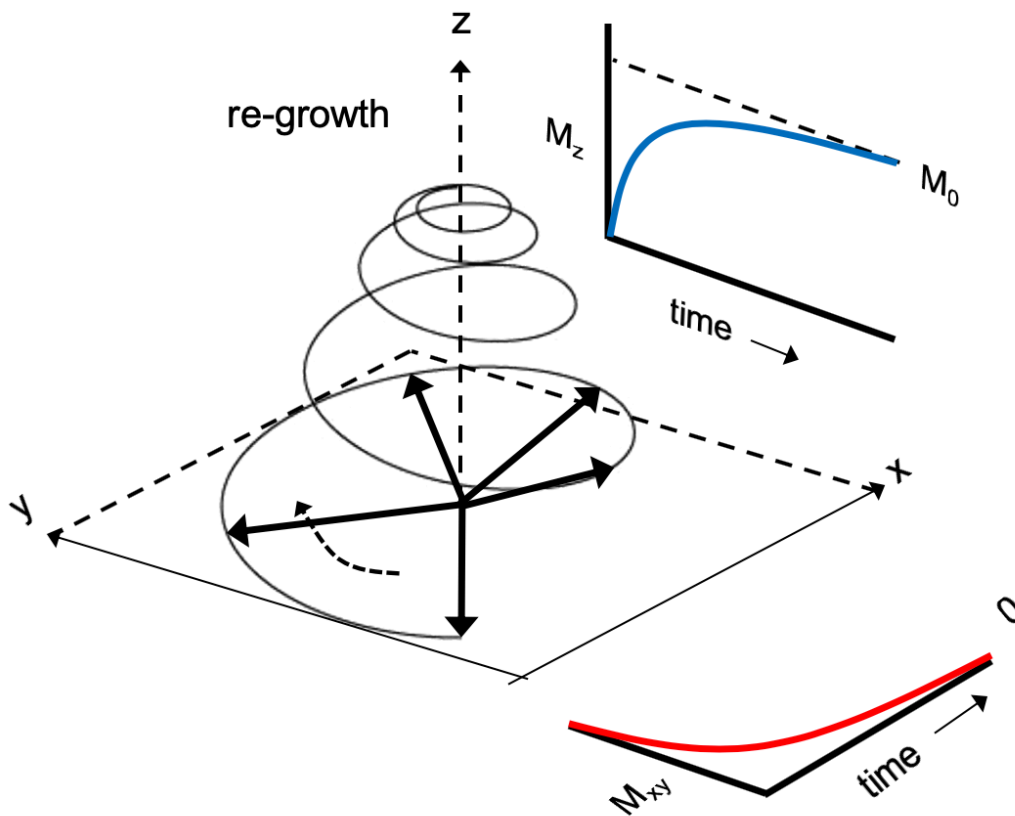


Figure 1.4. Transverse Decay and Longitudinal Restoration. When the net magnetization (\vec{M}_0) is tipped by a 90° radiofrequency pulse away from the magnetic field direction (\hat{z}), the longitudinal magnetization, M_z is completely transferred to the transverse (xy) plane, where the resulting transverse magnetization (M_{xy}) precesses at the Larmor frequency (f_0), about the axis of the external magnetic field (z). M_z regrows as a simple exponential with time constant T_1 . On the M_z graph, it corresponds to the time required for M_z to grow to approximately 63% ($1 - 1/e$) of its final value (M_0). Similarly, the transverse relaxation time T_2 represents the time required for M_x or M_y to decay to approximately 37% ($1/e$) of their initial maximum values. This image was adapted from MRIquestions.com, courtesy of Dr. Allen D. Elster.

1.5.3 Generating Image Contrast

A linear magnetic field z-gradient is imposed along each Cartesian axis to spatially encode signals from every voxel in the MR imaging matrix. These gradients are many orders of magnitude smaller than the main field and are used to modify the frequency and phase of proton spins as a function of spatial position. That is, spatial encoding is achieved by assigning a unique phase and frequency to each location of the imaging volume. A series of instructions known as a “pulse sequence” is used to synchronize the RF excitation of \vec{M}_0 and manipulate the gradient fields at specified time intervals.

After RF excitation, the transverse magnetization, M_{xy} induces a voltage in the RF coil, which is digitized and stored as the MR signal. MR signals arise from multiple voxels recorded all at once, each containing different tissues with different proton densities and relaxation times. The resulting total MR imaging data is thus the sum of many sinusoidal frequencies near the Larmor frequency with different phases, whose amplitudes rise or fall as a result of T_2 effects and magnetic field inhomogeneities. Fourier transform methods are applied to the MR imaging data to sort out the frequency components and accumulated phases for reconstruction of the physical image.

1.5.4 Contrast in Images

Imaging parameters such as time-to-repetition (TR), time-to-echo (TE) and flip or excitation angle (α) can be specifically chosen to highlight different physical properties of tissues within the imaging volume related to their relaxation

properties, which makes them more conspicuous. For example, using parameters to produce T_1 -weighted images, tissues with short T_1 values such as fat appear bright since they magnetize quickly while those with a long T_1 like water or air appear dark. Contrast in T_2 -weighted images depends on the rate of dephasing (spin-spin relaxation) in a particular voxel following an RF excitation. In T_2 -weighted images, tissues with a long T_2 , like cerebrospinal fluid, appear bright, while tissues with a short T_2 , such as fat, appear dark (**Table 1.2**).

Paramagnetic agents such as gadolinium (Gd)- and manganese (Mn)-based contrast agents (GBCAs, MBCAs, respectively) are not directly observed on MR images, but rather, enhance the relaxation of surrounding protons, effectively shortening the T_1 value of the tissue in which it accumulates, resulting in hyperintense volumes on T_1 -weighted images. The paramagnetic susceptibility of these elements is proportional to the number of unpaired electrons they possess *e.g.* seven for Gd. However, the ionic radius of free Gd^{+3} mimics that of Ca^{+2} , and this chemical mimicry is cause for toxicity. Free gadolinium becomes a competitive inhibitor in processes that depend on Ca^{+2} , including voltage-gated calcium channels and the activity of many vital enzymes. All GBCAs therefore require a ligand to chelate the free ion. This thesis specifically applies a clinically approved contrast agent, gadolinium ethoxybenzyl diethylene triamine pentaacetic acid (Gd-EOB-DTPA), known as Primovist, (Bayer, Inc.) as a probe for the development of a magnetic resonance imaging reporter gene.

Tissue	T_1 Time (ms)	T_2 Time (ms)
Water/CSF	3700 - 4000	2000
Gray Matter	1331 - 1485	80 - 96
White Matter	832 - 923	70 - 110
Muscle	898 - 1249	29 - 34
Liver	745 - 809	31 - 34
Fat	382 - 391	68 - 87

Table 1.2. Relaxation Times of Common Tissues at 3 Tesla. Spin-lattice relaxation (T_1) times, and spin-spin relaxation (T_2) times, in milliseconds of various human tissues at 3 Tesla (162).

1.5.5 Reporter Genes for Magnetic Resonance Imaging

Reporter genes for MRI include a diverse group of protein-based mechanisms through which contrast is enhanced. These can be separated into different classes based on the type of contrast produced: 1) negative contrast on ^1H MRI (106, 163-166), 2) positive contrast on ^1H MRI (110, 167), 3) hyperpolarization-based reporters (168, 169), 4) diffusion-weighted reporters (169, 170), and those based on 5) chemical exchange saturation transfer (CEST) (105, 168). Perhaps the most widely investigated class of MR reporter genes are those that generate negative contrast (hypointense signal), based on the principle of iron sequestration. High concentrations of iron cause magnetic susceptibility changes in tissues that, in turn, increase their *effective* spin-spin relaxation *i.e.* decrease T_2^* .

Negative contrast reporter genes include the iron storage molecule ferritin (163), the transferrin receptor (TfR) (164), the bacterial iron transporter magA (165), and the tyrosinase enzyme that produces iron-chelating melanin (166). Although negative contrast reporter genes have been demonstrated for various cancer-related applications, *e.g.* detection of dendritic cell migration to lymph nodes (171), presence of cancer cells in lymph nodes (172), regions of limited or no contrast already exist throughout the body at various major sites, making it difficult to definitively identify the location of engineered cells with accuracy and precision without serious reliance on pre-contrast images acquired at the start of the study.

Positive contrast mechanisms overcome this limitation by instead increasing the spin-lattice relaxation of tissues, or in other words decreasing T_1 , thereby causing increased local image intensity. Additionally, most of these positive contrast mechanisms depend on the administration of an agent for contrast enhancement, allowing for comparison of pre- and post-contrast images for increased conspicuity. Positive contrast reporter genes include the β -galactosidase enzyme capable of cleaving a caged synthetic Gd^{3+} probe (110), a divalent metal transporter capable of taking up Mn^{2+} (167), and an organic anion-transporting polypeptide transporter capable of taking up chelated Gd (173). This thesis focuses on the development of *organic anion-transporting polypeptides* as multimodality reporter genes that facilitate cancer cell tracking with magnetic resonance and photoacoustic imaging, with concomitant enhancement of bioluminescence signals in luciferase-expressing cells.

1.5.6 Organic Anion-Transporting Polypeptides

Organic anion-transporting polypeptides (Oatp) represent a large family of multispecific transporter proteins, differentially expressed on various mammalian tissues, including the kidneys, the liver, the heart, the brain, and the testis (174). Physiologically, they play a role in mediating the uptake of various compounds, including bile acids and steroid conjugates (175). Their presence in the body, however, have made them an important factor to consider in the design and development of several xenobiotics e.g. statins, some antibiotics, and anticancer drugs (176). Though the exact mechanism of *Oatp*-mediated transport remains

controversial, it is well established that transport is ATP- and sodium-independent. The driving force for its transport remains an active area of research in both pharmacology and hepatology. With respect to imaging, human *Oatp1b1* and *Oatp1b3* are exploited for detection of liver lesions with MRI using a clinical contrast agent, gadolinium-ethoxybenzyl-diethylenetriamine pentaacetic acid (Gd-EOB-DTPA), whose trade name is Primovist (Bayer, Inc) (177). Healthy liver cells expressing *Oatp1b1* and *Oatp1b3* are capable of taking up Gd-EOB-DTPA and appear bright on MRI after its administration. Diseased regions of the liver (e.g. hepatocellular carcinoma cells or fibrosis) do not express these transporters and are unable to take up Gd-EOB-DTPA, and appear hypointense relative to regions of healthy liver.

Motivated by this mechanism, work on *Oatp* reporter gene development began by scientists at the University of Cambridge who established rat-derived *Oatp1a1* as an MR reporter gene, based on its ability to transport Gd-EOB-DTPA into expressing cells (173). As the Gd concentration increases within engineered cells following injection of the contrast agent, the Gd interacts with the water protons in the intracellular environment, increasing the spin-lattice relaxation rate of those protons, which in turn, increases the signal intensity from those voxels on T_1 -weighted MR images. Longitudinal *in vivo* imaging has determined the optimal time to image is approximately 5 hours after administration of the contrast agent. At this time interval, most nonspecific (extracellular) contrast is cleared from the body and only cells engineered to express *Oatp1* retain the agent, thereby increasing the image contrast for those cells with up to a 7.8-fold

in vivo signal enhancement at 7 Tesla following an injection of 2-mmol/kg Gd-EOB-DTPA in mice. Contrast enhancement in the *Oatp1a1*-expressing xenografts returned to baseline levels by 60 hours (**Figure 1.5**). Since this initial publication, however, very little further research has been undertaken to develop this technology for gene and/or cell tracking applications. The unique combination of advantages presented by this reporter gene, which include its employment of a clinical probe as well as its reversibility, dose-dependent expression, positive contrast, and multimodal capabilities, warranted further study into its development as a reporter gene for whole-body tracking of engineered cells.

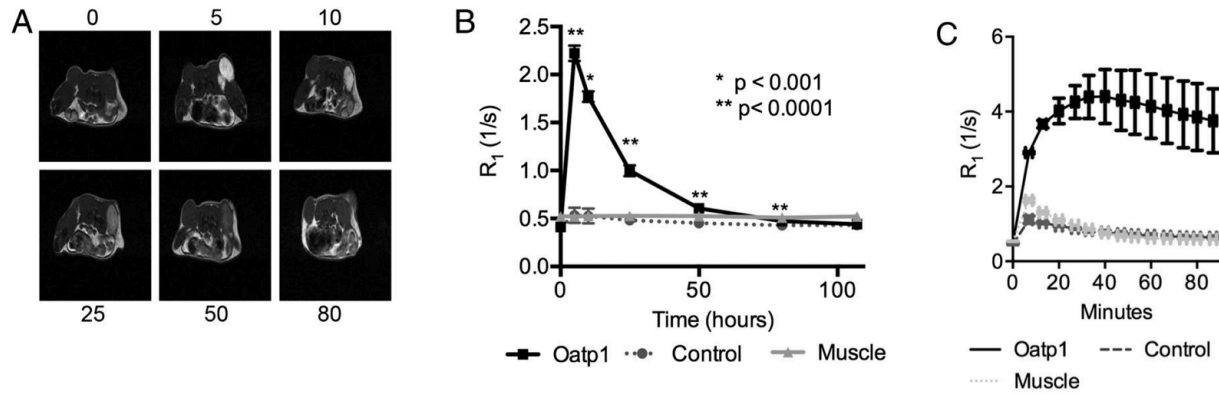


Figure 1.5. Magnetic Resonance Imaging of *Oatp1* Expression *In Vivo*. (A) T_1 -weighted images before (0) and 5, 10, 25, 50, and 80 hours after intravenous injection of Gd-EOB-DTPA, of a representative animal bearing 293T xenografts. Control xenograft (left flank) expressed luciferase and the xenografts on the right flank expressed luciferase and *Oatp1*. (B) Xenograft relaxation rates (R_1) before (0) and following intravenous injection of Gd-EOB-DTPA (0.664 mmoles/kg) were significantly greater compared with controls [$*P < 0.001$, $**P < 0.0001$, $n = 5$ ($n = 4$ at 107 h)]. (C) R_1 increased in control and *Oatp1*-expressing xenografts after repeated intravenous injection with Gd-EOB-DTPA (0.664 mmoles/kg), following washout of the original dose in A/B and injection and washout of Gd-DTPA. This figure was acquired from Patrick *et al.* (173).

1.6 Photoacoustic Imaging

1.6.1 Basic Principles

Light in the visible portion of the spectrum is highly scattered by tissues. Methods that attempt to form images from light passing through tissue fall into two categories: ballistic (minimally scattered) microscopy *e.g.* fluorescence microscopy, and diffuse (multi-scattered) imaging *e.g.* bioluminescence imaging. The former provides fine resolution but with a shallow imaging depth in tissue, up to approximately 1 mm, as defined by the optical diffusion limit (178). When incident photons reach this depth, most have undergone tens of scattering events, which randomize the photon paths and inhibit effective optical focusing and image formation. On the other hand, diffuse optical imaging can probe centimeters into tissue but with limited spatial resolution, equivalent to about one-third the imaging depth (179). Randomized paths of the diffuse photons render the image reconstruction difficult. It remains a challenge for conventional optical imaging to attain fine spatial resolution at depths beyond the optical diffusion limit.

Photoacoustic imaging (PAI), or optoacoustic imaging, is a hybrid imaging modality based on acoustic detection of optically-excited sources, thereby combining the advantages of optical contrast specificity with the spatial resolution of ultrasound (180). In the photoacoustic effect, endogenous molecules such as de-oxyhemoglobin and oxyhemoglobin, or exogenous contrast agents, are excited by nanosecond-pulsed laser beams and rapidly convert a fraction of that energy into heat during relaxation. This heat energy leads to a transient

thermoelastic expansion, resulting in the emission of ultrasonic waves that can be detected with ultrasound transducers to produce images. Photoacoustic imaging side steps the optical diffusion limit by exploiting low acoustic scattering in tissue, about three orders of magnitude less than optical scattering in tissue per unit path length (181). By exciting different molecules at different optical wavelengths, photoacoustic imaging reveals rich optical contrasts according to chemical composition, and provides inherently background-free detection because the photoacoustic amplitude is proportional to the optical absorption and quantum yield of the target molecules (182). In relation to other optical modalities (e.g., fluorescence imaging), photoacoustic imaging has the capability of improved resolution and increased depth of imaging (**Figure 1.6**).

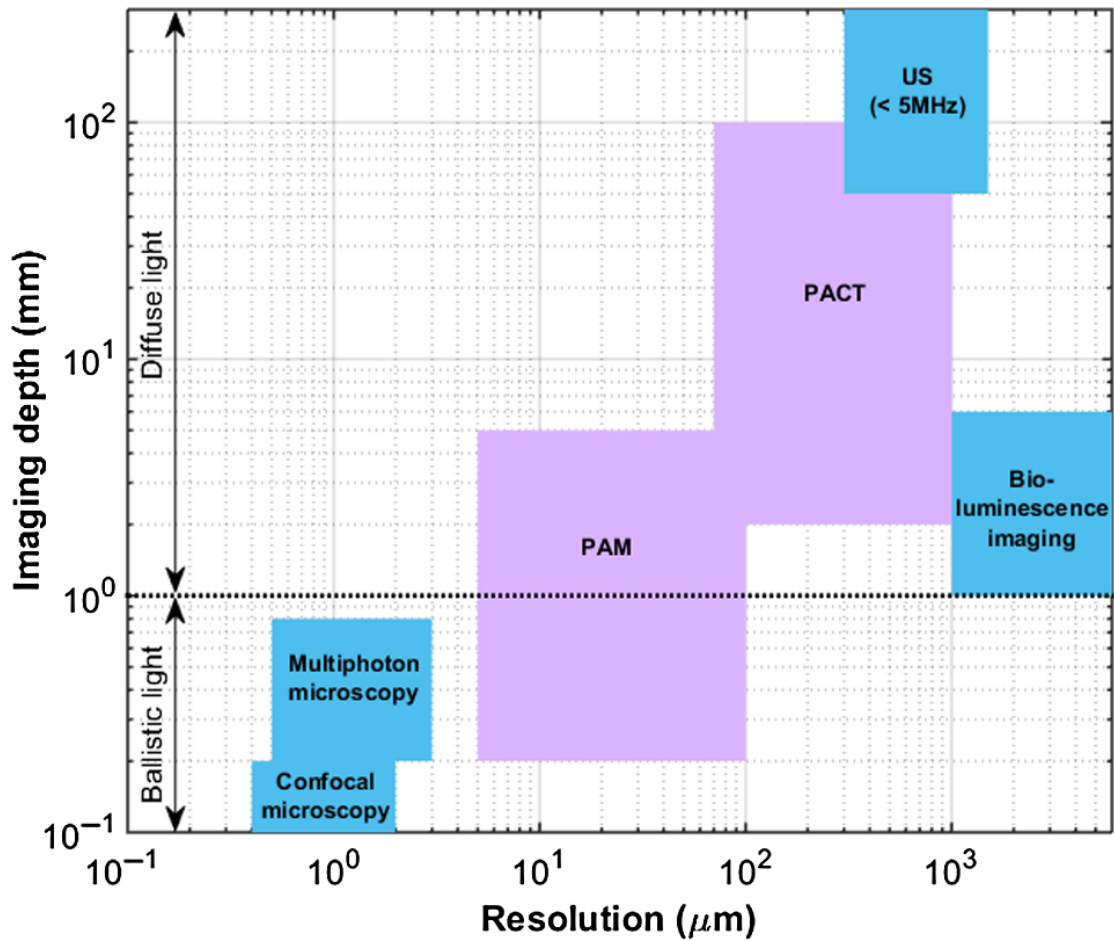


Figure 1.6. Imaging Resolution vs Imaging Depth of Optical or Optic-based Modalities. Comparison of the performance of photoacoustic imaging with that of optical and ultrasonic modalities, with respect to their imaging depth and spatial resolution. PAM, photoacoustic microscopy; PACT, photoacoustic computed tomography; US, ultrasound imaging. Figure was acquired from Brunker *et al.* (101).

1.6.2 Applications for Cancer Research

Photoacoustic imaging is a relatively nascent modality, first demonstrated in the late 1990s (183-185) and recent refinements have led to broad applications in biology and medicine. Major preclinical applications include imaging of angiogenesis, microcirculation, tumour microenvironments, drug response, biomarkers, and gene activities (186), while initial clinical applications include melanoma cancer imaging, gastrointestinal tract endoscopy, intravascular catheter imaging, neonatal brain imaging, breast and prostate cancer detection, sentinel lymph node needle guidance, imaging of early chemotherapy response, *in vivo* label-free histology, blood perfusion imaging, blood oxygenation imaging, and tissue metabolism imaging (186-188).

1.6.3 Photoacoustic Reporter Genes

Though the field of photoacoustic imaging is relatively new, the small number of endogenous contrast sources within biological tissues, and the ability to acquire real-time co-registered anatomical images with ultrasound, has spurred rapid development of several reporter genes for gene and/or cell tracking on photoacoustic imaging. Photoacoustic reporter genes can be classified as either direct or indirect, depending on whether the protein encoded is the source of contrast, or whether the protein instead processes an injected agent that, in turn, generates the contrast (101). Briefly, photoacoustic reporter genes with direct mechanisms include fluorescent, nonfluorescent/chromoprotein, and photoswitchable reporter genes. On the other hand, indirect mechanisms have

so far consisted of enzymatic proteins, including tyrosinase, β -galactosidase, and the VioA-E operon. Of these, tyrosinase and β -galactosidase have been more widely employed. Human-derived tyrosinase is responsible for the rate limiting step in the melanin synthesis pathway, that is, the oxidation of tyrosine to dopaquinone (189). Specifically, melanin exhibits a broad extinction coefficient spectrum, that spans the visible to near-infrared wavelength region and possesses a relatively low quantum yield, allowing for its detection on photoacoustic imaging (190, 191). The β -galactosidase reporter, encoded by the bacterial-derived *LacZ* gene, is naturally responsible for lactose metabolism, but is more widely known for its role in a chromogenic complementation assay, whereby the colourless lactose analog 5-bromo-4-chloro-3-indolyl- β -D-galactoside probe, known as X-gal, is cleaved, thereby yielding a stable dark blue product (192). In 2007, β -galactosidase was demonstrated as the first photoacoustic reporter gene for *in vivo* imaging, with significant contrast-to-noise at 650 nm wavelengths (193). Indirect mechanisms of genetically-encoded photoacoustic contrast present with several advantages over direct mechanisms, but primarily offer signal amplification, allowing for increased sensitivity for gene and/or cell tracking (194). Interestingly, both tyrosinase and β -galactosidase have also been previously established as MR reporter genes, thereby allowing for multi-modality molecular imaging for *in vivo* gene and/or cell tracking (195).

1.7 Purpose of Thesis

1.7.1 Rationale

The reporter gene approach for *in vivo* molecular imaging has significant potential for cell tracking applications in preclinical research and clinical medicine. Specifically, the ability of the *Oatp1* reporter gene to transport and concentrate specific clinical contrast agents within engineered cells, could allow for sensitive, high resolution imaging in 3D, with positive contrast with several imaging modalities. The overall objective of the work presented in this thesis is to develop and assess new methods of reporter gene imaging for tracking of engineered cancer cells in preclinical mouse models.

1.7.2 Hypothesis

In its development and assessment of *Oatp1* as a multimodality reporter gene for *in vivo* molecular imaging, this thesis is testing three primary hypotheses:

1. Rat-derived *Oatp1a1* will facilitate longitudinal imaging of viable cancer cell distributions within primary tumours on MRI at 3 Tesla, based on its *in vivo* ability to transport Gd-EOB-DTPA into cells.
2. Human-derived *Oatp1b3* will allow for longitudinal, whole-body imaging of spontaneous cancer cell metastasis on MRI at 3 Tesla, based on its ability to take up Gd-EOB-DTPA *in vivo*.
3. Human-derived *Oatp1b3* can be utilized as a photoacoustic imaging reporter gene, for detection of viable cancer cells, based on its ability to take up indocyanine green *in vivo*.

1.7.3 Overview of Studies

In our initial research, we strove to build on the seminal work first reported in *PNAS*, which established rat-derived *Oatp1a1* as an MRI reporter gene using the paramagnetic contrast agent, Gd-EOB-DTPA (173). We wanted to extend this work by establishing the feasibility of using *Oatp1a1* at clinical doses of Gd-EOB-DTPA and a clinical field strength of 3 Tesla. In **Chapter 2**, we demonstrated for the first time that *Oatp1a1* is able to provide high resolution, 3D information on the distribution of viable cancer cells in primary tumours, at clinical contrast agent dose and field strength. Importantly, we validated the local contrast enhancement exhibited on MRI with quantitative histology. This chapter has been peer-reviewed and accepted for publication as: Nyström NN, Hamilton AM, Xia W, Liu S, Scholl TJ, Ronald JA. “Longitudinal Visualization of Viable Cancer Cell Intratumoral Distribution in Mouse Models Using *Oatp1a1*-Enhanced Magnetic Resonance Imaging.” *Investigative Radiology*. 2019 May; 54(5): 302-311. DOI: 10.1097/RLI.0000000000 0000542. In **Chapter 3**, we worked with human-derived *Oatp1b3*, a closely-related transporter to the rat-derived *Oatp1a1*, and worked to establish its potential future use in humans as a clinical-grade reporter gene. This research validated that *Oatp1b3*, like *Oatp1a1*, can also transport Gd-EOB-DTPA with a significant efficiency for MR imaging. Importantly, we further demonstrated that *Oatp1b3* facilitates sensitive imaging of spontaneous metastasis in preclinical mouse models at the single lymph node, multi-lymph node, and distant organ metastatic stages on MRI at 3 Tesla. Chapter 3 is currently in preparation as a manuscript for submission to peer-

review. In **Chapter 4**, our research was focused on expanding the *Oatp1* imaging reporter gene “toolkit” beyond MR imaging to include photoacoustic imaging. This extension offers potential for cost-effective, 3D imaging at tissue depths of several centimeters. Here, we first demonstrated in *in vitro* experiments that *Oatp1b3* will transport indocyanine green resulting in increased signal-to-noise ratios for both fluorescence and photoacoustic imaging. Using *in vivo* fluorescence imaging, we determined the optimal imaging timepoint after administration of indocyanine green to be 24 hours post-intraperitoneal injection. And finally, we established in a murine breast cancer model that *in vivo* photoacoustic imaging can readily detect *Oatp1b3*-engineered cancer cells after injection of indocyanine green. This chapter has been peer-reviewed and accepted for publication as: NN Nyström, LCM Yip, JJJ Carson, TJ Scholl, JA Ronald. “Development of a Human Photoacoustic Imaging Reporter Gene Using the Clinical Dye Indocyanine Green.” *Radiology: Imaging Cancer* 1 (2), e190035. DOI: 10.1148/rycan.201919 0035.

1.8 References

1. Mortality GBD, Causes of Death C. Global, regional, and national life expectancy, all-cause mortality, and cause-specific mortality for 249 causes of death, 1980-2015: a systematic analysis for the Global Burden of Disease Study 2015. *Lancet* 2016;388(10053):1459-1544. doi: 10.1016/S0140-6736(16)31012-1
2. Mankoff DA, Farwell MD, Clark AS, Pryma DA. Making Molecular Imaging a Clinical Tool for Precision Oncology: A Review. *JAMA Oncol* 2017;3(5):695-701. doi: 10.1001/jamaoncol.2016.5084
3. Gambhir SS, Ge TJ, Vermesh O, Spitler R. Toward achieving precision health. *Sci Transl Med* 2018;10(430). doi: 10.1126/scitranslmed.aao3612
4. Keu KV, Witney TH, Yaghoubi S, Rosenberg J, Kurien A, Magnusson R, Williams J, Habte F, Wagner JR, Forman S, Brown C, Allen-Auerbach M, Czernin J, Tang W, Jensen MC, Badie B, Gambhir SS. Reporter gene imaging of targeted T cell immunotherapy in recurrent glioma. *Sci Transl Med* 2017;9(373). doi: 10.1126/scitranslmed.aag2196
5. Siegel RL, Miller KD, Jemal A. Cancer statistics, 2019. *CA Cancer J Clin* 2019;69(1):7-34. doi: 10.3322/caac.21551
6. Waks AG, Winer EP. Breast Cancer Treatment: A Review. *JAMA* 2019;321(3):288-300. doi: 10.1001/jama.2018.19323
7. Siegel RL, Miller KD, Jemal A. Cancer statistics, 2016. *CA Cancer J Clin* 2016;66(1):7-30. doi: 10.3322/caac.21332

8. Desai A, Small EJ. Treatment of advanced renal cell carcinoma patients with cabozantinib, an oral multityrosine kinase inhibitor of MET, AXL and VEGF receptors. *Future Oncol* 2019;15(20):2337-2348. doi: 10.2217/fon-2019-0021
9. Visan I. Tumor architecture. *Nat Immunol* 2018;19(3):206. doi: 10.1038/s41590-018-0061-y
10. Carmeliet P, Jain RK. Molecular mechanisms and clinical applications of angiogenesis. *Nature* 2011;473(7347):298-307. doi: 10.1038/nature10144
11. Bousso P, Moreau HD. Functional immunoimaging: the revolution continues. *Nat Rev Immunol* 2012;12(12):858-864. doi: 10.1038/nri3342
12. Zhang J, Liu J. Tumor stroma as targets for cancer therapy. *Pharmacol Ther* 2013;137(2):200-215. doi: 10.1016/j.pharmthera.2012.10.003
13. Glasner A, Levi A, Enk J, Isaacson B, Viukov S, Orlanski S, Scope A, Neuman T, Enk CD, Hanna JH, Sexl V, Jonjic S, Seliger B, Zitvogel L, Mandelboim O. NKp46 Receptor-Mediated Interferon-gamma Production by Natural Killer Cells Increases Fibronectin 1 to Alter Tumor Architecture and Control Metastasis. *Immunity* 2018;48(2):396-398. doi: 10.1016/j.immuni.2018.01.010
14. Siegel RL, Miller KD, Jemal A. Cancer statistics, 2020. *CA Cancer J Clin* 2020;70(1):7-30. doi: 10.3322/caac.21590
15. Lambert AW, Pattabiraman DR, Weinberg RA. Emerging Biological Principles of Metastasis. *Cell* 2017;168(4):670-691. doi: 10.1016/j.cell.2016.11.037
16. Gengenbacher N, Singhal M, Augustin HG. Preclinical mouse solid tumour models: status quo, challenges and perspectives. *Nat Rev Cancer* 2017;17(12):751-765. doi: 10.1038/nrc.2017.92

17. Leach DR, Krummel MF, Allison JP. Enhancement of antitumor immunity by CTLA-4 blockade. *Science* 1996;271(5256):1734-1736. doi: 10.1126/science.271.5256.1734
18. Walsh NC, Kenney LL, Jangalwe S, Aryee KE, Greiner DL, Brehm MA, Shultz LD. Humanized Mouse Models of Clinical Disease. *Annu Rev Pathol* 2017;12:187-215. doi: 10.1146/annurev-pathol-052016-100332
19. Sharkey FE, Fogh J. Incidence and pathological features of spontaneous tumors in athymic nude mice. *Cancer Res* 1979;39(3):833-839.
20. Carreno BM, Garbow JR, Kolar GR, Jackson EN, Engelbach JA, Becker-Hapak M, Carayannopoulos LN, Piwnica-Worms D, Linette GP. Immunodeficient mouse strains display marked variability in growth of human melanoma lung metastases. *Clin Cancer Res* 2009;15(10):3277-3286. doi: 10.1158/1078-0432.CCR-08-2502
21. Scherer WF, Syverton JT, Gey GO. Studies on the propagation in vitro of poliomyelitis viruses. IV. Viral multiplication in a stable strain of human malignant epithelial cells (strain HeLa) derived from an epidermoid carcinoma of the cervix. *J Exp Med* 1953;97(5):695-710. doi: 10.1084/jem.97.5.695
22. Rose RM. Informed consent: history, theory, and practice. *Am J Otol* 1986;7(1):82-85.
23. Cailleau R, Olive M, Cruciger QV. Long-term human breast carcinoma cell lines of metastatic origin: preliminary characterization. *In Vitro* 1978;14(11):911-915. doi: 10.1007/bf02616120
24. Ethier SP, Mahacek ML, Gullick WJ, Frank TS, Weber BL. Differential isolation of normal luminal mammary epithelial cells and breast cancer cells from primary and metastatic sites using selective media. *Cancer Res* 1993;53(3):627-635.

25. Miller FR, Miller BE, Heppner GH. Characterization of metastatic heterogeneity among subpopulations of a single mouse mammary tumor: heterogeneity in phenotypic stability. *Invasion Metastasis* 1983;3(1):22-31.
26. Miller FR. Tumor subpopulation interactions in metastasis. *Invasion Metastasis* 1983;3(4):234-242.
27. Ling X, Arlinghaus RB. Knockdown of STAT3 expression by RNA interference inhibits the induction of breast tumors in immunocompetent mice. *Cancer Res* 2005;65(7):2532-2536. doi: 10.1158/0008-5472.CAN-04-2425
28. Josefsson A, Nedrow JR, Park S, Banerjee SR, Rittenbach A, Jammes F, Tsui B, Sgouros G. Imaging, Biodistribution, and Dosimetry of Radionuclide-Labeled PD-L1 Antibody in an Immunocompetent Mouse Model of Breast Cancer. *Cancer Res* 2016;76(2):472-479. doi: 10.1158/0008-5472.CAN-15-2141
29. Borrell B. How accurate are cancer cell lines? *Nature* 2010;463(7283):858. doi: 10.1038/463858a
30. Weinstein JN. Drug discovery: Cell lines battle cancer. *Nature* 2012;483(7391):544-545. doi: 10.1038/483544a
31. Osborne CK, Hobbs K, Clark GM. Effect of estrogens and antiestrogens on growth of human breast cancer cells in athymic nude mice. *Cancer Res* 1985;45(2):584-590.
32. Gottardis MM, Robinson SP, Jordan VC. Estradiol-stimulated growth of MCF-7 tumors implanted in athymic mice: a model to study the tumoristatic action of tamoxifen. *J Steroid Biochem* 1988;30(1-6):311-314. doi: 10.1016/0022-4731(88)90113-6
33. Robertson JF, Osborne CK, Howell A, Jones SE, Mauriac L, Ellis M, Kleeberg UR, Come SE, Vergote I, Gertler S, Buzdar A, Webster A, Morris C. Fulvestrant versus

anastrozole for the treatment of advanced breast carcinoma in postmenopausal women: a prospective combined analysis of two multicenter trials. *Cancer* 2003;98(2):229-238.

doi: 10.1002/cncr.11468

34. Johnston SJ, Cheung KL. Fulvestrant - a novel endocrine therapy for breast cancer. *Curr Med Chem* 2010;17(10):902-914. doi: 10.2174/092986710790820633

35. Talmadge JE, Singh RK, Fidler IJ, Raz A. Murine models to evaluate novel and conventional therapeutic strategies for cancer. *Am J Pathol* 2007;170(3):793-804. doi: 10.2353/ajpath.2007.060929

36. Killion JJ, Radinsky R, Fidler IJ. Orthotopic models are necessary to predict therapy of transplantable tumors in mice. *Cancer Metastasis Rev* 1998;17(3):279-284. doi: 10.1023/a:1006140513233

37. Hackl C, Man S, Francia G, Milsom C, Xu P, Kerbel RS. Metronomic oral topotecan prolongs survival and reduces liver metastasis in improved preclinical orthotopic and adjuvant therapy colon cancer models. *Gut* 2013;62(2):259-271. doi: 10.1136/gutjnl-2011-301585

38. Hiroshima Y, Maawy A, Zhang Y, Zhang N, Murakami T, Chishima T, Tanaka K, Ichikawa Y, Bouvet M, Endo I, Hoffman RM. Patient-derived mouse models of cancer need to be orthotopic in order to evaluate targeted anti-metastatic therapy. *Oncotarget* 2016;7(44):71696-71702. doi: 10.18632/oncotarget.12322

39. Hiroshima Y, Zhang Y, Zhang N, Maawy A, Mii S, Yamamoto M, Uehara F, Miwa S, Yano S, Murakami T, Momiyama M, Chishima T, Tanaka K, Ichikawa Y, Bouvet M, Murata T, Endo I, Hoffman RM. Establishment of a patient-derived orthotopic Xenograft

(PDOX) model of HER-2-positive cervical cancer expressing the clinical metastatic pattern. PLoS One 2015;10(2):e0117417. doi: 10.1371/journal.pone.0117417

40. Hoffman RM. Patient-derived orthotopic xenografts: better mimic of metastasis than subcutaneous xenografts. Nat Rev Cancer 2015;15(8):451-452. doi: 10.1038/nrc3972

41. Segovia-Mendoza M, Morales-Montor J. Immune Tumor Microenvironment in Breast Cancer and the Participation of Estrogen and Its Receptors in Cancer Physiopathology. Front Immunol 2019;10:348. doi: 10.3389/fimmu.2019.00348

42. Tevaarwerk AJ, Gray RJ, Schneider BP, Smith ML, Wagner LI, Fetting JH, Davidson N, Goldstein LJ, Miller KD, Sparano JA. Survival in patients with metastatic recurrent breast cancer after adjuvant chemotherapy: little evidence of improvement over the past 30 years. Cancer 2013;119(6):1140-1148. doi: 10.1002/cncr.27819

43. Barker HE, Paget JT, Khan AA, Harrington KJ. The tumour microenvironment after radiotherapy: mechanisms of resistance and recurrence. Nat Rev Cancer 2015;15(7):409-425. doi: 10.1038/nrc3958

44. Christiansen A, Detmar M. Lymphangiogenesis and cancer. Genes Cancer 2011;2(12):1146-1158. doi: 10.1177/1947601911423028

45. Kaushik S, Pickup MW, Weaver VM. From transformation to metastasis: deconstructing the extracellular matrix in breast cancer. Cancer Metastasis Rev 2016;35(4):655-667. doi: 10.1007/s10555-016-9650-0

46. Bernards N, Creemers GJ, Nieuwenhuijzen GA, Bosscha K, Pruijt JF, Lemmens VE. No improvement in median survival for patients with metastatic gastric cancer despite increased use of chemotherapy. Ann Oncol 2013;24(12):3056-3060. doi: 10.1093/annonc/mdt401

47. Worni M, Guller U, White RR, Castleberry AW, Pietrobon R, Cerny T, Gloor B, Koeberle D. Modest improvement in overall survival for patients with metastatic pancreatic cancer: a trend analysis using the surveillance, epidemiology, and end results registry from 1988 to 2008. *Pancreas* 2013;42(7):1157-1163. doi: 10.1097/MPA.0b013e318291fbc5
48. Berry DA. Adaptive clinical trials in oncology. *Nat Rev Clin Oncol* 2011;9(4):199-207. doi: 10.1038/nrclinonc.2011.165
49. Gomez-Cuadrado L, Tracey N, Ma R, Qian B, Brunton VG. Mouse models of metastasis: progress and prospects. *Dis Model Mech* 2017;10(9):1061-1074. doi: 10.1242/dmm.030403
50. Smith-Bindman R, Kwan ML, Marlow EC, Theis MK, Bolch W, Cheng SY, Bowles EJA, Duncan JR, Greenlee RT, Kushi LH, Pole JD, Rahm AK, Stout NK, Weinmann S, Miglioretti DL. Trends in Use of Medical Imaging in US Health Care Systems and in Ontario, Canada, 2000-2016. *JAMA* 2019;322(9):843-856. doi: 10.1001/jama.2019.11456
51. Maurer T, Eiber M, Schwaiger M, Gschwend JE. Current use of PSMA-PET in prostate cancer management. *Nat Rev Urol* 2016;13(4):226-235. doi: 10.1038/nrurol.2016.26
52. de Rooij M, Hamoen EH, Futterer JJ, Barentsz JO, Rovers MM. Accuracy of multiparametric MRI for prostate cancer detection: a meta-analysis. *AJR Am J Roentgenol* 2014;202(2):343-351. doi: 10.2214/AJR.13.11046
53. Lecouvet FE, Talbot JN, Messiou C, Bourguet P, Liu Y, de Souza NM, Group EI. Monitoring the response of bone metastases to treatment with Magnetic Resonance

- Imaging and nuclear medicine techniques: a review and position statement by the European Organisation for Research and Treatment of Cancer imaging group. *Eur J Cancer* 2014;50(15):2519-2531. doi: 10.1016/j.ejca.2014.07.002
54. Dimitrakopoulou-Strauss A, Ronellenfitsch U, Cheng C, Pan L, Sachpekidis C, Hohenberger P, Henzler T. Imaging therapy response of gastrointestinal stromal tumors (GIST) with FDG PET, CT and MRI: a systematic review. *Clin Transl Imaging* 2017;5(3):183-197. doi: 10.1007/s40336-017-0229-8
55. Miles KA. Cancer imaging: is it cost-effective? *Cancer Imaging* 2004;4(2):97-103. doi: 10.1102/1470-7330.2004.0017
56. Yang Y, Czernin J. Contribution of imaging to cancer care costs. *J Nucl Med* 2011;52 Suppl 2:86S-92S. doi: 10.2967/jnumed.110.085621
57. Keshavarzi M, Darijani M, Momeni F, Moradi P, Ebrahimnejad H, Masoudifar A, Mirzaei H. Molecular Imaging and Oral Cancer Diagnosis and Therapy. *J Cell Biochem* 2017;118(10):3055-3060. doi: 10.1002/jcb.26042
58. Williams LE. Anniversary paper: nuclear medicine: fifty years and still counting. *Med Phys* 2008;35(7):3020-3029. doi: 10.1118/1.2936217
59. James ML, Gambhir SS. A molecular imaging primer: modalities, imaging agents, and applications. *Physiol Rev* 2012;92(2):897-965. doi: 10.1152/physrev.00049.2010
60. Chaney A, Cropper HC, Johnson EM, Lechtenberg KJ, Peterson TC, Stevens MY, Buckwalter MS, James ML. (11)C-DPA-713 Versus (18)F-GE-180: A Preclinical Comparison of Translocator Protein 18 kDa PET Tracers to Visualize Acute and Chronic Neuroinflammation in a Mouse Model of Ischemic Stroke. *J Nucl Med* 2019;60(1):122-128. doi: 10.2967/jnumed.118.209155

61. Gallagher FA, Woitek R, McLean MA, Gill AB, Manzano Garcia R, Provenzano E, Riemer F, Kaggie J, Chhabra A, Ursprung S, Grist JT, Daniels CJ, Zaccagna F, Laurent MC, Locke M, Hilborne S, Frary A, Torheim T, Boursnell C, Schiller A, Patterson I, Slough R, Carmo B, Kane J, Biggs H, Harrison E, Deen SS, Patterson A, Lanz T, Kingsbury Z, Ross M, Basu B, Baird R, Lomas DJ, Sala E, Wason J, Rueda OM, Chin SF, Wilkinson IB, Graves MJ, Abraham JE, Gilbert FJ, Caldas C, Brindle KM. Imaging breast cancer using hyperpolarized carbon-13 MRI. *Proc Natl Acad Sci U S A* 2020;117(4):2092-2098. doi: 10.1073/pnas.1913841117
62. Luo S, Zhang E, Su Y, Cheng T, Shi C. A review of NIR dyes in cancer targeting and imaging. *Biomaterials* 2011;32(29):7127-7138. doi: 10.1016/j.biomaterials.2011.06.024
63. Wester HJ. Nuclear imaging probes: from bench to bedside. *Clin Cancer Res* 2007;13(12):3470-3481. doi: 10.1158/1078-0432.CCR-07-0264
64. Wang ZJ, Ohliger MA, Larson PEZ, Gordon JW, Bok RA, Slater J, Villanueva-Meyer JE, Hess CP, Kurhanewicz J, Vigneron DB. Hyperpolarized (13)C MRI: State of the Art and Future Directions. *Radiology* 2019;291(2):273-284. doi: 10.1148/radiol.2019182391
65. Kurhanewicz J, Vigneron DB, Ardenkjaer-Larsen JH, Bankson JA, Brindle K, Cunningham CH, Gallagher FA, Keshari KR, Kjaer A, Laustsen C, Mankoff DA, Merritt ME, Nelson SJ, Pauly JM, Lee P, Ronen S, Tyler DJ, Rajan SS, Spielman DM, Wald L, Zhang X, Malloy CR, Rizi R. Hyperpolarized (13)C MRI: Path to Clinical Translation in Oncology. *Neoplasia* 2019;21(1):1-16. doi: 10.1016/j.neo.2018.09.006
66. Najac C, Chaumeil MM, Kohanbash G, Guglielmetti C, Gordon JW, Okada H, Ronen SM. Detection of inflammatory cell function using (13)C magnetic resonance

spectroscopy of hyperpolarized [6-(13)C]-arginine. *Sci Rep* 2016;6:31397. doi:
10.1038/srep31397

67. Chaumeil MM, Larson PE, Woods SM, Cai L, Eriksson P, Robinson AE, Lupo JM, Vigneron DB, Nelson SJ, Pieper RO, Phillips JJ, Ronen SM. Hyperpolarized [1-13C] glutamate: a metabolic imaging biomarker of IDH1 mutational status in glioma. *Cancer Res* 2014;74(16):4247-4257. doi: 10.1158/0008-5472.CAN-14-0680

68. Timm KN, Hu DE, Williams M, Wright AJ, Kettunen MI, Kennedy BW, Larkin TJ, Dzien P, Marco-Rius I, Bohndiek SE, Brindle KM. Assessing Oxidative Stress in Tumors by Measuring the Rate of Hyperpolarized [1-13C]Dehydroascorbic Acid Reduction Using 13C Magnetic Resonance Spectroscopy. *J Biol Chem* 2017;292(5):1737-1748. doi: 10.1074/jbc.M116.761536

69. Van Nostrand D, Abreu SH, Callaghan JJ, Atkins FB, Stoops HC, Savory CG. In-111-labeled white blood cell uptake in noninfected closed fracture in humans: prospective study. *Radiology* 1988;167(2):495-498. doi:
10.1148/radiology.167.2.3357961

70. Foster-Gareau P, Heyn C, Alejski A, Rutt BK. Imaging single mammalian cells with a 1.5 T clinical MRI scanner. *Magn Reson Med* 2003;49(5):968-971. doi:
10.1002/mrm.10417

71. Han S, Bouchard R, Sokolov KV. Molecular photoacoustic imaging with ultra-small gold nanoparticles. *Biomed Opt Express* 2019;10(7):3472-3483. doi:
10.1364/BOE.10.003472

72. Menk RH, Schultke E, Hall C, Arfelli F, Astolfo A, Rigon L, Round A, Ataelmannan K, MacDonald SR, Juurlink BH. Gold nanoparticle labeling of cells is a sensitive method

to investigate cell distribution and migration in animal models of human disease.

Nanomedicine 2011;7(5):647-654. doi: 10.1016/j.nano.2011.01.010

73. Bull E, Madani SY, Sheth R, Seifalian A, Green M, Seifalian AM. Stem cell tracking using iron oxide nanoparticles. *Int J Nanomedicine* 2014;9:1641-1653. doi: 10.2147/IJN.S48979

74. Kiessling F, Mertens ME, Grimm J, Lammers T. Nanoparticles for imaging: top or flop? *Radiology* 2014;273(1):10-28. doi: 10.1148/radiol.14131520

75. Heyn C, Ronald JA, Mackenzie LT, MacDonald IC, Chambers AF, Rutt BK, Foster PJ. In vivo magnetic resonance imaging of single cells in mouse brain with optical validation. *Magn Reson Med* 2006;55(1):23-29. doi: 10.1002/mrm.20747

76. Heyn C, Ronald JA, Ramadan SS, Snir JA, Barry AM, MacKenzie LT, Mikulis DJ, Palmieri D, Bronder JL, Steeg PS, Yoneda T, MacDonald IC, Chambers AF, Rutt BK, Foster PJ. In vivo MRI of cancer cell fate at the single-cell level in a mouse model of breast cancer metastasis to the brain. *Magn Reson Med* 2006;56(5):1001-1010. doi: 10.1002/mrm.21029

77. Li L, Jiang W, Luo K, Song H, Lan F, Wu Y, Gu Z. Superparamagnetic iron oxide nanoparticles as MRI contrast agents for non-invasive stem cell labeling and tracking. *Theranostics* 2013;3(8):595-615. doi: 10.7150/thno.5366

78. Chan JMS, Cheung MSH, Gibbs RGJ, Bhakoo KK. MRI detection of endothelial cell inflammation using targeted superparamagnetic particles of iron oxide (SPIO). *Clin Transl Med* 2017;6(1):1. doi: 10.1186/s40169-016-0134-1

79. Zanganeh S, Hutter G, Spitler R, Lenkov O, Mahmoudi M, Shaw A, Pajarinen JS, Nejadnik H, Goodman S, Moseley M, Coussens LM, Daldrup-Link HE. Iron oxide

nanoparticles inhibit tumour growth by inducing pro-inflammatory macrophage polarization in tumour tissues. *Nat Nanotechnol* 2016;11(11):986-994. doi: 10.1038/nnano.2016.168

80. Takasato M, Er PX, Becroft M, Vanslambrouck JM, Stanley EG, Elefanty AG, Little MH. Directing human embryonic stem cell differentiation towards a renal lineage generates a self-organizing kidney. *Nat Cell Biol* 2014;16(1):118-126. doi: 10.1038/ncb2894

81. Bajar BT, Wang ES, Zhang S, Lin MZ, Chu J. A Guide to Fluorescent Protein FRET Pairs. *Sensors (Basel)* 2016;16(9). doi: 10.3390/s16091488

82. Kobayashi H, Picard LP, Schonegge AM, Bouvier M. Bioluminescence resonance energy transfer-based imaging of protein-protein interactions in living cells. *Nat Protoc* 2019;14(4):1084-1107. doi: 10.1038/s41596-019-0129-7

83. Morsut L, Roybal KT, Xiong X, Gordley RM, Coyle SM, Thomson M, Lim WA. Engineering Customized Cell Sensing and Response Behaviors Using Synthetic Notch Receptors. *Cell* 2016;164(4):780-791. doi: 10.1016/j.cell.2016.01.012

84. Boone PG, Rochelle LK, Ginzler JD, Lubkov V, Roberts WL, Nicholls PJ, Bock C, Flowers ML, von Furstenberg RJ, Stripp BR, Agarwal P, Borowsky AD, Cardiff RD, Barak LS, Caron MG, Lyerly HK, Snyder JC. A cancer rainbow mouse for visualizing the functional genomics of oncogenic clonal expansion. *Nat Commun* 2019;10(1):5490. doi: 10.1038/s41467-019-13330-y

85. Xin G, Schauder DM, Jing W, Jiang A, Joshi NS, Johnson B, Cui W. Pathogen boosted adoptive cell transfer immunotherapy to treat solid tumors. *Proc Natl Acad Sci U S A* 2017;114(4):740-745. doi: 10.1073/pnas.1614315114

86. Yang JC, Rosenberg SA. Adoptive T-Cell Therapy for Cancer. *Adv Immunol* 2016;130:279-294. doi: 10.1016/bs.ai.2015.12.006
87. Dunbar CE, High KA, Joung JK, Kohn DB, Ozawa K, Sadelain M. Gene therapy comes of age. *Science* 2018;359(6372). doi: 10.1126/science.aan4672
88. Kelly J. J. S-MM, Nyström N. N., Chen Y., Evans M. M., Hamilton A. M., Ronald J. A. A Safe Harbor-Targeted CRISPR/Cas9 Homology Independent Targeted Integration (HITI) System for Multi-Modality Reporter Gene-Based Cell Tracking. *bioRxiv* 2020;2020.02.10.942672. doi: <https://doi.org/10.1101/2020.02.10.942672>
89. Riley MK, Vermerris W. Recent Advances in Nanomaterials for Gene Delivery-A Review. *Nanomaterials (Basel)* 2017;7(5). doi: 10.3390/nano7050094
90. Naldini L, Blomer U, Gallay P, Ory D, Mulligan R, Gage FH, Verma IM, Trono D. In vivo gene delivery and stable transduction of nondividing cells by a lentiviral vector. *Science* 1996;272(5259):263-267. doi: 10.1126/science.272.5259.263
91. Choi JG, Dang Y, Abraham S, Ma H, Zhang J, Guo H, Cai Y, Mikkelsen JG, Wu H, Shankar P, Manjunath N. Lentivirus pre-packed with Cas9 protein for safer gene editing. *Gene Ther* 2016;23(7):627-633. doi: 10.1038/gt.2016.27
92. Watson DJ, Kobinger GP, Passini MA, Wilson JM, Wolfe JH. Targeted transduction patterns in the mouse brain by lentivirus vectors pseudotyped with VSV, Ebola, Mokola, LCMV, or MuLV envelope proteins. *Mol Ther* 2002;5(5 Pt 1):528-537. doi: 10.1006/mthe.2002.0584
93. Georgiadis C, Preece R, Nickolay L, Etuk A, Petrova A, Ladon D, Danyi A, Humphries-Kirilov N, Ajetunmobi A, Kim D, Kim JS, Qasim W. Long Terminal Repeat

- CRISPR-CAR-Coupled "Universal" T Cells Mediate Potent Anti-leukemic Effects. *Mol Ther* 2018;26(5):1215-1227. doi: 10.1016/j.ymthe.2018.02.025
94. Gilad AA, Shapiro MG. Molecular Imaging in Synthetic Biology, and Synthetic Biology in Molecular Imaging. *Mol Imaging Biol* 2017;19(3):373-378. doi: 10.1007/s11307-017-1062-1
95. Weissleder R. Molecular imaging in cancer. *Science* 2006;312(5777):1168-1171. doi: 10.1126/science.1125949
96. Bhaumik S, Gambhir SS. Optical imaging of Renilla luciferase reporter gene expression in living mice. *Proc Natl Acad Sci U S A* 2002;99(1):377-382. doi: 10.1073/pnas.012611099
97. Brasier AR, Tate JE, Habener JF. Optimized use of the firefly luciferase assay as a reporter gene in mammalian cell lines. *Biotechniques* 1989;7(10):1116-1122.
98. Millar AJ, Carre IA, Strayer CA, Chua NH, Kay SA. Circadian clock mutants in *Arabidopsis* identified by luciferase imaging. *Science* 1995;267(5201):1161-1163. doi: 10.1126/science.7855595
99. Hall MP, Unch J, Binkowski BF, Valley MP, Butler BL, Wood MG, Otto P, Zimmerman K, Vidugiris G, Machleidt T, Robers MB, Benink HA, Eggers CT, Slater MR, Meisenheimer PL, Klaubert DH, Fan F, Encell LP, Wood KV. Engineered luciferase reporter from a deep sea shrimp utilizing a novel imidazopyrazinone substrate. *ACS Chem Biol* 2012;7(11):1848-1857. doi: 10.1021/cb3002478
100. Iwano S, Sugiyama M, Hama H, Watakabe A, Hasegawa N, Kuchimaru T, Tanaka KZ, Takahashi M, Ishida Y, Hata J, Shimozone S, Namiki K, Fukano T, Kiyama M, Okano H, Kizaka-Kondoh S, McHugh TJ, Yamamori T, Hioki H, Maki S, Miyawaki A.

Single-cell bioluminescence imaging of deep tissue in freely moving animals. *Science* 2018;359(6378):935-939. doi: 10.1126/science.aaq1067

101. Brunker J, Yao J, Laufer J, Bohndiek SE. Photoacoustic imaging using genetically encoded reporters: a review. *J Biomed Opt* 2017;22(7). doi: 10.1117/1.JBO.22.7.070901

102. Ray P, De A, Min JJ, Tsien RY, Gambhir SS. Imaging tri-fusion multimodality reporter gene expression in living subjects. *Cancer Res* 2004;64(4):1323-1330.

103. Gambhir SS, Bauer E, Black ME, Liang Q, Kokoris MS, Barrio JR, Iyer M, Namavari M, Phelps ME, Herschman HR. A mutant herpes simplex virus type 1 thymidine kinase reporter gene shows improved sensitivity for imaging reporter gene expression with positron emission tomography. *Proc Natl Acad Sci U S A* 2000;97(6):2785-2790. doi: 10.1073/pnas.97.6.2785

104. Gambhir SS, Barrio JR, Phelps ME, Iyer M, Namavari M, Satyamurthy N, Wu L, Green LA, Bauer E, MacLaren DC, Nguyen K, Berk AJ, Cherry SR, Herschman HR. Imaging adenoviral-directed reporter gene expression in living animals with positron emission tomography. *Proc Natl Acad Sci U S A* 1999;96(5):2333-2338. doi: 10.1073/pnas.96.5.2333

105. Gilad AA, McMahon MT, Walczak P, Winnard PT, Jr., Raman V, van Laarhoven HW, Skoglund CM, Bulte JW, van Zijl PC. Artificial reporter gene providing MRI contrast based on proton exchange. *Nat Biotechnol* 2007;25(2):217-219. doi: 10.1038/nbt1277

106. Patrick PS, Rodrigues TB, Kettunen MI, Lyons SK, Neves AA, Brindle KM. Development of Timd2 as a reporter gene for MRI. *Magn Reson Med* 2016;75(4):1697-1707. doi: 10.1002/mrm.25750

107. Hill PJ, Stritzker J, Scadeng M, Geissinger U, Haddad D, Basse-Lusebrink TC, Gbureck U, Jakob P, Szalay AA. Magnetic resonance imaging of tumors colonized with bacterial ferritin-expressing *Escherichia coli*. *PLoS One* 2011;6(10):e25409. doi: 10.1371/journal.pone.0025409
108. Ichikawa T, Hogemann D, Saeki Y, Tyminski E, Terada K, Weissleder R, Chiocca EA, Basilion JP. MRI of transgene expression: correlation to therapeutic gene expression. *Neoplasia* 2002;4(6):523-530. doi: 10.1038/sj.neo.7900266
109. Paproski RJ, Forbrich AE, Wachowicz K, Hitt MM, Zemp RJ. Tyrosinase as a dual reporter gene for both photoacoustic and magnetic resonance imaging. *Biomed Opt Express* 2011;2(4):771-780. doi: 10.1364/BOE.2.000771
110. Louie AY, Huber MM, Ahrens ET, Rothbacher U, Moats R, Jacobs RE, Fraser SE, Meade TJ. In vivo visualization of gene expression using magnetic resonance imaging. *Nat Biotechnol* 2000;18(3):321-325. doi: 10.1038/73780
111. Farhadi A, Ho GH, Sawyer DP, Bourdeau RW, Shapiro MG. Ultrasound imaging of gene expression in mammalian cells. *Science* 2019;365(6460):1469-1475. doi: 10.1126/science.aax4804
112. Tzeng SY, Patel KK, Wilson DR, Meyer RA, Rhodes KR, Green JJ. In situ genetic engineering of tumors for long-lasting and systemic immunotherapy. *Proc Natl Acad Sci U S A* 2020;117(8):4043-4052. doi: 10.1073/pnas.1916039117
113. Maddalo D, Manchado E, Concepcion CP, Bonetti C, Vidigal JA, Han YC, Ogdowski P, Crippa A, Rekhtman N, de Stanchina E, Lowe SW, Ventura A. In vivo engineering of oncogenic chromosomal rearrangements with the CRISPR/Cas9 system. *Nature* 2014;516(7531):423-427. doi: 10.1038/nature13902

114. Tabebordbar M, Zhu K, Cheng JKW, Chew WL, Widrick JJ, Yan WX, Maesner C, Wu EY, Xiao R, Ran FA, Cong L, Zhang F, Vandenberghe LH, Church GM, Wagers AJ. In vivo gene editing in dystrophic mouse muscle and muscle stem cells. *Science* 2016;351(6271):407-411. doi: 10.1126/science.aad5177
115. Patton JA, Townsend DW, Hutton BF. Hybrid imaging technology: from dreams and vision to clinical devices. *Semin Nucl Med* 2009;39(4):247-263. doi: 10.1053/j.semnuclmed.2009.03.005
116. Ehman EC, Johnson GB, Villanueva-Meyer JE, Cha S, Leynes AP, Larson PEZ, Hope TA. PET/MRI: Where might it replace PET/CT? *J Magn Reson Imaging* 2017;46(5):1247-1262. doi: 10.1002/jmri.25711
117. Sosa MS, Bragado P, Aguirre-Ghiso JA. Mechanisms of disseminated cancer cell dormancy: an awakening field. *Nat Rev Cancer* 2014;14(9):611-622. doi: 10.1038/nrc3793
118. Parkins KM, Hamilton AM, Makela AV, Chen Y, Foster PJ, Ronald JA. A multimodality imaging model to track viable breast cancer cells from single arrest to metastasis in the mouse brain. *Sci Rep* 2016;6:35889. doi: 10.1038/srep35889
119. Le TNT, Lim H, Hamilton AM, Parkins KM, Chen Y, Scholl TJ, Ronald JA. Characterization of an Orthotopic Rat Model of Glioblastoma Using Multiparametric Magnetic Resonance Imaging and Bioluminescence Imaging. *Tomography* 2018;4(2):55-65. doi: 10.18383/j.tom.2018.00012
120. Fritz V, Louis-Plence P, Apparailly F, Noel D, Voide R, Pillon A, Nicolas JC, Muller R, Jorgensen C. Micro-CT combined with bioluminescence imaging: a dynamic

approach to detect early tumor-bone interaction in a tumor osteolysis murine model. *Bone* 2007;40(4):1032-1040. doi: 10.1016/j.bone.2006.11.026

121. Yao Z, Zhang BS, Prescher JA. Advances in bioluminescence imaging: new probes from old recipes. *Curr Opin Chem Biol* 2018;45:148-156. doi: 10.1016/j.cbpa.2018.05.009

122. Dukhovich A, Sillero A, Sillero MA. Time course of luciferyl adenylate synthesis in the firefly luciferase reaction. *FEBS Lett* 1996;395(2-3):188-190. doi: 10.1016/0014-5793(96)01038-1

123. Rhodes WC, Mc EW. The synthesis and function of luciferyl-adenylate and oxyluciferyl-adenylate. *J Biol Chem* 1958;233(6):1528-1537.

124. Fraga H, Esteves da Silva JC, Fontes R. Identification of luciferyl adenylate and luciferyl coenzyme a synthesized by firefly luciferase. *Chembiochem* 2004;5(1):110-115. doi: 10.1002/cbic.200300735

125. Viviani VR. The origin, diversity, and structure function relationships of insect luciferases. *Cell Mol Life Sci* 2002;59(11):1833-1850. doi: 10.1007/pl00012509

126. DeLuca M, McElroy WD. Kinetics of the firefly luciferase catalyzed reactions. *Biochemistry* 1974;13(5):921-925. doi: 10.1021/bi00702a015

127. Wilson T, Hastings JW. Bioluminescence. *Annu Rev Cell Dev Biol* 1998;14:197-230. doi: 10.1146/annurev.cellbio.14.1.197

128. Hirano T, Nagai H, Matsushashi T, Hasumi Y, Iwano S, Ito K, Maki S, Niwa H, Viviani VR. Spectroscopic studies of the color modulation mechanism of firefly (beetle) bioluminescence with amino-analogs of luciferin and oxyluciferin. *Photochem Photobiol Sci* 2012;11(8):1281-1284. doi: 10.1039/c2pp25106j

129. Rhodes WC, Mc EW. Enzymatic synthesis of adenylyl-luciferin. *Science* 1958;128(3318):253-254. doi: 10.1126/science.128.3318.253
130. Belas R, Mileham A, Cohn D, Hilman M, Simon M, Silverman M. Bacterial bioluminescence: isolation and expression of the luciferase genes from *Vibrio harveyi*. *Science* 1982;218(4574):791-793. doi: 10.1126/science.10636771
131. de Wet JR, Wood KV, Helinski DR, DeLuca M. Cloning of firefly luciferase cDNA and the expression of active luciferase in *Escherichia coli*. *Proc Natl Acad Sci U S A* 1985;82(23):7870-7873. doi: 10.1073/pnas.82.23.7870
132. Keller GA, Gould S, DeLuca M, Subramani S. Firefly luciferase is targeted to peroxisomes in mammalian cells. *Proc Natl Acad Sci U S A* 1987;84(10):3264-3268. doi: 10.1073/pnas.84.10.3264
133. Contag CH, Contag PR, Mullins JI, Spilman SD, Stevenson DK, Benaron DA. Photonic detection of bacterial pathogens in living hosts. *Mol Microbiol* 1995;18(4):593-603. doi: 10.1111/j.1365-2958.1995.mmi_18040593.x
134. de Wet JR, Wood KV, DeLuca M, Helinski DR, Subramani S. Firefly luciferase gene: structure and expression in mammalian cells. *Mol Cell Biol* 1987;7(2):725-737. doi: 10.1128/mcb.7.2.725
135. Nakatsu T, Ichiyama S, Hiratake J, Saldanha A, Kobashi N, Sakata K, Kato H. Structural basis for the spectral difference in luciferase bioluminescence. *Nature* 2006;440(7082):372-376. doi: 10.1038/nature04542
136. Rehemtulla A, Stegman LD, Cardozo SJ, Gupta S, Hall DE, Contag CH, Ross BD. Rapid and quantitative assessment of cancer treatment response using in vivo bioluminescence imaging. *Neoplasia* 2000;2(6):491-495. doi: 10.1038/sj.neo.7900121

137. Berger F, Paulmurugan R, Bhaumik S, Gambhir SS. Uptake kinetics and biodistribution of ¹⁴C-D-luciferin--a radiolabeled substrate for the firefly luciferase catalyzed bioluminescence reaction: impact on bioluminescence based reporter gene imaging. *Eur J Nucl Med Mol Imaging* 2008;35(12):2275-2285. doi: 10.1007/s00259-008-0870-6
138. Sweeney TJ, Mailander V, Tucker AA, Olomu AB, Zhang W, Cao Y, Negrin RS, Contag CH. Visualizing the kinetics of tumor-cell clearance in living animals. *Proc Natl Acad Sci U S A* 1999;96(21):12044-12049. doi: 10.1073/pnas.96.21.12044
139. Paroo Z, Bollinger RA, Braasch DA, Richer E, Corey DR, Antich PP, Mason RP. Validating bioluminescence imaging as a high-throughput, quantitative modality for assessing tumor burden. *Mol Imaging* 2004;3(2):117-124. doi: 10.1162/1535350041464865
140. Wu JC, Sundaresan G, Iyer M, Gambhir SS. Noninvasive optical imaging of firefly luciferase reporter gene expression in skeletal muscles of living mice. *Mol Ther* 2001;4(4):297-306. doi: 10.1006/mthe.2001.0460
141. Cosette J, Ben Abdelwahed R, Donnou-Triffault S, Sautes-Fridman C, Flaud P, Fisson S. Bioluminescence-Based Tumor Quantification Method for Monitoring Tumor Progression and Treatment Effects in Mouse Lymphoma Models. *J Vis Exp* 2016(113). doi: 10.3791/53609
142. Chalfie M. GFP: Lighting up life. *Proc Natl Acad Sci U S A* 2009;106(25):10073-10080. doi: 10.1073/pnas.0904061106

143. Doyle TC, Burns SM, Contag CH. In vivo bioluminescence imaging for integrated studies of infection. *Cell Microbiol* 2004;6(4):303-317. doi: 10.1111/j.1462-5822.2004.00378.x
144. Burd CE, Sorrentino JA, Clark KS, Darr DB, Krishnamurthy J, Deal AM, Bardeesy N, Castrillon DH, Beach DH, Sharpless NE. Monitoring tumorigenesis and senescence in vivo with a p16(INK4a)-luciferase model. *Cell* 2013;152(1-2):340-351. doi: 10.1016/j.cell.2012.12.010
145. Vantaggiato C, Dell'Omo G, Ramachandran B, Manni I, Radaelli E, Scanziani E, Piaggio G, Maggi A, Ciana P. Bioluminescence imaging of estrogen receptor activity during breast cancer progression. *Am J Nucl Med Mol Imaging* 2016;6(1):32-41.
146. de Latouliere L, Manni I, Iacobini C, Pugliese G, Grazi GL, Perri P, Cappello P, Novelli F, Menini S, Piaggio G. A bioluminescent mouse model of proliferation to highlight early stages of pancreatic cancer: A suitable tool for preclinical studies. *Ann Anat* 2016;207:2-8. doi: 10.1016/j.aanat.2015.11.010
147. Ju HL, Calvisi DF, Moon H, Baek S, Ribback S, Dombrowski F, Cho KJ, Chung SI, Han KH, Ro SW. Transgenic mouse model expressing P53(R172H), luciferase, EGFP, and KRAS(G12D) in a single open reading frame for live imaging of tumor. *Sci Rep* 2015;5:8053. doi: 10.1038/srep08053
148. Benzekry S, Tracz A, Mastri M, Corbelli R, Barbolosi D, Ebos JM. Modeling Spontaneous Metastasis following Surgery: An In Vivo-In Silico Approach. *Cancer Res* 2016;76(3):535-547. doi: 10.1158/0008-5472.CAN-15-1389

149. Stacer AC, Fenner J, Cavnar SP, Xiao A, Zhao S, Chang SL, Salomonson A, Luker KE, Luker GD. Endothelial CXCR7 regulates breast cancer metastasis. *Oncogene* 2016;35(13):1716-1724. doi: 10.1038/onc.2015.236
150. Feng HY, Zhang Y, Liu HJ, Dong X, Yang SC, Lu Q, Meng F, Chen HZ, Sun P, Fang C. Characterization of an orthotopic gastric cancer mouse model with lymph node and organ metastases using bioluminescence imaging. *Oncol Lett* 2018;16(4):5179-5185. doi: 10.3892/ol.2018.9313
151. Zhang X, Wang J, Chen Z, Hu Q, Wang C, Yan J, Dotti G, Huang P, Gu Z. Engineering PD-1-Presenting Platelets for Cancer Immunotherapy. *Nano Lett* 2018;18(9):5716-5725. doi: 10.1021/acs.nanolett.8b02321
152. Yang Y, Hou W, Liu S, Sun K, Li M, Wu C. Biodegradable Polymer Nanoparticles for Photodynamic Therapy by Bioluminescence Resonance Energy Transfer. *Biomacromolecules* 2018;19(1):201-208. doi: 10.1021/acs.biomac.7b01469
153. Tan J, Li M, Zhong W, Hu C, Gu Q, Xie Y. Tyrosine kinase inhibitors show different anti-brain metastases efficacy in NSCLC: A direct comparative analysis of icotinib, gefitinib, and erlotinib in a nude mouse model. *Oncotarget* 2017;8(58):98771-98781. doi: 10.18632/oncotarget.21936
154. Zinn KR, Chaudhuri TR, Szafran AA, O'Quinn D, Weaver C, Dugger K, Lamar D, Kesterson RA, Wang X, Frank SJ. Noninvasive bioluminescence imaging in small animals. *ILAR J* 2008;49(1):103-115. doi: 10.1093/ilar.49.1.103
155. Welsh DK, Kay SA. Bioluminescence imaging in living organisms. *Curr Opin Biotechnol* 2005;16(1):73-78. doi: 10.1016/j.copbio.2004.12.006

156. Kubota SI, Takahashi K, Nishida J, Morishita Y, Ehata S, Tainaka K, Miyazono K, Ueda HR. Whole-Body Profiling of Cancer Metastasis with Single-Cell Resolution. *Cell Rep* 2017;20(1):236-250. doi: 10.1016/j.celrep.2017.06.010
157. Badr CE. Bioluminescence imaging: basics and practical limitations. *Methods Mol Biol* 2014;1098:1-18. doi: 10.1007/978-1-62703-718-1_1
158. Han W, Wang G. Bioluminescence Tomography: Biomedical Background, Mathematical Theory, and Numerical Approximation. *J Comput Math* 2008;26(3):324-335.
159. Yeh HW, Wu T, Chen M, Ai HW. Identification of Factors Complicating Bioluminescence Imaging. *Biochemistry* 2019;58(12):1689-1697. doi: 10.1021/acs.biochem.8b01303
160. Baklaushev VP, Kilpelainen A, Petkov S, Abakumov MA, Grinenko NF, Yusubalieva GM, Latanova AA, Gubskiy IL, Zabozaev FG, Starodubova ES, Abakumova TO, Isaguliantz MG, Chekhonin VP. Luciferase Expression Allows Bioluminescence Imaging But Imposes Limitations on the Orthotopic Mouse (4T1) Model of Breast Cancer. *Sci Rep* 2017;7(1):7715. doi: 10.1038/s41598-017-07851-z
161. Pohost GM, Elgavish GA, Evanochko WT. Nuclear magnetic resonance imaging: with or without nuclear? *J Am Coll Cardiol* 1986;7(3):709-710. doi: 10.1016/s0735-1097(86)80486-7
162. Bojorquez JZ, Bricq S, Acquitter C, Brunotte F, Walker PM, Lalande A. What are normal relaxation times of tissues at 3 T? *Magn Reson Imaging* 2017;35:69-80. doi: 10.1016/j.mri.2016.08.021

163. Cohen B, Dafni H, Meir G, Harmelin A, Neeman M. Ferritin as an endogenous MRI reporter for noninvasive imaging of gene expression in C6 glioma tumors. *Neoplasia* 2005;7(2):109-117. doi: 10.1593/neo.04436
164. Moore A, Josephson L, Bhorade RM, Basilion JP, Weissleder R. Human transferrin receptor gene as a marker gene for MR imaging. *Radiology* 2001;221(1):244-250. doi: 10.1148/radiol.2211001784
165. Zurkiya O, Chan AW, Hu X. MagA is sufficient for producing magnetic nanoparticles in mammalian cells, making it an MRI reporter. *Magn Reson Med* 2008;59(6):1225-1231. doi: 10.1002/mrm.21606
166. Weissleder R, Simonova M, Bogdanova A, Bredow S, Enochs WS, Bogdanov A, Jr. MR imaging and scintigraphy of gene expression through melanin induction. *Radiology* 1997;204(2):425-429. doi: 10.1148/radiology.204.2.9240530
167. Bartelle BB, Szulc KU, Suero-Abreu GA, Rodriguez JJ, Turnbull DH. Divalent metal transporter, DMT1: a novel MRI reporter protein. *Magn Reson Med* 2013;70(3):842-850. doi: 10.1002/mrm.24509
168. Shapiro MG, Ramirez RM, Sperling LJ, Sun G, Sun J, Pines A, Schaffer DV, Bajaj VS. Genetically encoded reporters for hyperpolarized xenon magnetic resonance imaging. *Nat Chem* 2014;6(7):629-634. doi: 10.1038/nchem.1934
169. Patrick PS, Kettunen MI, Tee SS, Rodrigues TB, Serrao E, Timm KN, McGuire S, Brindle KM. Detection of transgene expression using hyperpolarized ¹³C urea and diffusion-weighted magnetic resonance spectroscopy. *Magn Reson Med* 2015;73(4):1401-1406. doi: 10.1002/mrm.25254

170. Mukherjee A, Wu D, Davis HC, Shapiro MG. Non-invasive imaging using reporter genes altering cellular water permeability. *Nat Commun* 2016;7:13891. doi: 10.1038/ncomms13891
171. Kim HS, Woo J, Lee JH, Joo HJ, Choi Y, Kim H, Moon WK, Kim SJ. In vivo Tracking of Dendritic Cell using MRI Reporter Gene, Ferritin. *PLoS One* 2015;10(5):e0125291. doi: 10.1371/journal.pone.0125291
172. Choi SH, Cho HR, Kim HS, Kim YH, Kang KW, Kim H, Moon WK. Imaging and quantification of metastatic melanoma cells in lymph nodes with a ferritin MR reporter in living mice. *NMR Biomed* 2012;25(5):737-745. doi: 10.1002/nbm.1788
173. Patrick PS, Hammersley J, Loizou L, Kettunen MI, Rodrigues TB, Hu DE, Tee SS, Hesketh R, Lyons SK, Soloviev D, Lewis DY, Aime S, Fulton SM, Brindle KM. Dual-modality gene reporter for in vivo imaging. *Proc Natl Acad Sci U S A* 2014;111(1):415-420. doi: 10.1073/pnas.1319000111
174. Hagenbuch B, Meier PJ. The superfamily of organic anion transporting polypeptides. *Biochim Biophys Acta* 2003;1609(1):1-18. doi: 10.1016/s0005-2736(02)00633-8
175. Kalliokoski A, Niemi M. Impact of OATP transporters on pharmacokinetics. *Br J Pharmacol* 2009;158(3):693-705. doi: 10.1111/j.1476-5381.2009.00430.x
176. Roth M, Obaidat A, Hagenbuch B. OATPs, OATs and OCTs: the organic anion and cation transporters of the SLCO and SLC22A gene superfamilies. *Br J Pharmacol* 2012;165(5):1260-1287. doi: 10.1111/j.1476-5381.2011.01724.x

177. Pastor CM, Mullhaupt B, Stieger B. The role of organic anion transporters in diagnosing liver diseases by magnetic resonance imaging. *Drug Metab Dispos* 2014;42(4):675-684. doi: 10.1124/dmd.113.055707
178. Kothapalli SR, Sakadzic S, Kim C, Wang LV. Imaging optically scattering objects with ultrasound-modulated optical tomography. *Opt Lett* 2007;32(16):2351-2353. doi: 10.1364/ol.32.002351
179. Culver JP, Ntziachristos V, Holboke MJ, Yodh AG. Optimization of optode arrangements for diffuse optical tomography: A singular-value analysis. *Opt Lett* 2001;26(10):701-703. doi: 10.1364/ol.26.000701
180. Zhou Y, Yao J, Wang LV. Tutorial on photoacoustic tomography. *J Biomed Opt* 2016;21(6):61007. doi: 10.1117/1.JBO.21.6.061007
181. Wang LV. Multiscale photoacoustic microscopy and computed tomography. *Nat Photonics* 2009;3(9):503-509. doi: 10.1038/nphoton.2009.157
182. Wang LV. Prospects of photoacoustic tomography. *Med Phys* 2008;35(12):5758-5767. doi: 10.1118/1.3013698
183. Kruger RA, Liu P, Fang YR, Appledorn CR. Photoacoustic ultrasound (PAUS)--reconstruction tomography. *Med Phys* 1995;22(10):1605-1609. doi: 10.1118/1.597429
184. Hoelen CG, de Mul FF, Pongers R, Dekker A. Three-dimensional photoacoustic imaging of blood vessels in tissue. *Opt Lett* 1998;23(8):648-650. doi: 10.1364/ol.23.000648
185. Kruger RA, Miller KD, Reynolds HE, Kiser WL, Jr., Reinecke DR, Kruger GA. Breast cancer in vivo: contrast enhancement with thermoacoustic CT at 434 MHz-

feasibility study. *Radiology* 2000;216(1):279-283. doi:
10.1148/radiology.216.1.r00jl30279

186. Valluru KS, Wilson KE, Willmann JK. Photoacoustic Imaging in Oncology: Translational Preclinical and Early Clinical Experience. *Radiology* 2016;280(2):332-349. doi: 10.1148/radiol.16151414

187. Mehrmohammadi M, Yoon SJ, Yeager D, Emelianov SY. Photoacoustic Imaging for Cancer Detection and Staging. *Curr Mol Imaging* 2013;2(1):89-105. doi: 10.2174/2211555211302010010

188. Wong TTW, Zhang R, Hai P, Zhang C, Pleitez MA, Aft RL, Novack DV, Wang LV. Fast label-free multilayered histology-like imaging of human breast cancer by photoacoustic microscopy. *Sci Adv* 2017;3(5):e1602168. doi: 10.1126/sciadv.1602168

189. Iozumi K, Hoganson GE, Pennella R, Everett MA, Fuller BB. Role of tyrosinase as the determinant of pigmentation in cultured human melanocytes. *J Invest Dermatol* 1993;100(6):806-811. doi: 10.1111/1523-1747.ep12476630

190. Nighswander-Rempel SP, Riesz J, Gilmore J, Meredith P. A quantum yield map for synthetic eumelanin. *J Chem Phys* 2005;123(19):194901. doi: 10.1063/1.2075147

191. Paproski RJ, Heinmiller A, Wachowicz K, Zemp RJ. Multi-wavelength photoacoustic imaging of inducible tyrosinase reporter gene expression in xenograft tumors. *Sci Rep* 2014;4:5329. doi: 10.1038/srep05329

192. Langley KE, Villarejo MR, Fowler AV, Zamenhof PJ, Zabin I. Molecular basis of beta-galactosidase alpha-complementation. *Proc Natl Acad Sci U S A* 1975;72(4):1254-1257. doi: 10.1073/pnas.72.4.1254

193. Li L, Zemp RJ, Lungu G, Stoica G, Wang LV. Photoacoustic imaging of lacZ gene expression in vivo. *J Biomed Opt* 2007;12(2):020504. doi: 10.1117/1.2717531

194. Jathoul AP, Laufer J, Ogunlade O, Treeby B, Cox B, Zhang E, Johnson P, Pizzey AR, Philip B, Marafioti T, Lythgoe MF, Pedley RB, Pule MA, Beard P. Deep in vivo photoacoustic imaging of mammalian tissues using a tyrosinase-based genetic reporter. *Nature Photonics* 2015;9(4):239-246. doi: 10.1038/Nphoton.2015.22

195. Qin C, Cheng K, Chen K, Hu X, Liu Y, Lan X, Zhang Y, Liu H, Xu Y, Bu L, Su X, Zhu X, Meng S, Cheng Z. Tyrosinase as a multifunctional reporter gene for Photoacoustic/MRI/PET triple modality molecular imaging. *Sci Rep* 2013;3:1490. doi: 10.1038/srep01490

CHAPTER 2 Intratumoral Distribution of Viable Cancer Cells over Time

Rationale. Multimodality reporter gene imaging provides valuable, non-invasive information on the fate of engineered cell populations. To complement magnetic resonance imaging (MRI) measures of tumour volume and 2-dimensional reporter-based optical measures of cell viability, reporter-based MRI may offer 3-dimensional information on the distribution of viable cancer cells in deep tissues. **Methods.** Here, we engineered human and murine triple-negative breast cancer cells with lentivirus encoding tdTomato and firefly luciferase for fluorescence imaging and bioluminescence imaging (BLI). A subset of these cells was additionally engineered with lentivirus encoding *organic anion transporting polypeptide 1a1* (*Oatp1a1*) for MRI. *Oatp1a1* operates by transporting gadolinium ethoxybenzyl diethylenetriamine pentaacetic acid (Gd-EOB-DTPA) into cells, and it concomitantly improves BLI substrate uptake. After orthotopic implantation of engineered cells expressing or not expressing *Oatp1a1*, longitudinal fluorescence imaging, BLI, and 3-Tesla MRI were performed. **Results.** *Oatp1a1*-expressing tumours displayed significantly increased BLI signals relative to control tumours at all time points ($p < 0.05$). On MRI, post-Gd-EOB-DTPA T_1 -weighted images of *Oatp1a1*-expressing tumours exhibited significantly increased contrast-to-noise ratios compared with control tumours and pre-contrast images ($p < 0.05$). At endpoint, tumours expressing *Oatp1a1* displayed intratumoral MR signal heterogeneity not present at earlier time points. Pixel-based analysis of matched *in vivo* MR and *ex vivo* fluorescence microscopy images revealed a strong, positive correlation between MR intensity and tdTomato intensity for *Oatp1a1*-expressing tumours ($p < 0.05$), but not control tumours. **Conclusions.** These results characterize *Oatp1a1* as a sensitive,

quantitative, positive contrast MRI reporter gene for 3-dimensional assessment of viable cancer cell intratumoral distribution and concomitant BLI enhancement. This multimodality reporter gene system can provide new insights into the influence of viable cancer cell intratumoral distribution on tumour progression and metastasis, as well as improved assessments of anticancer therapies.

2.1 Introduction

Fluorescent reporter genes have provided valuable insight towards the understanding of molecular processes occurring in cancer, from the role of regulatory RNA (1, 2), to new knowledge on cancer stem cells (3), and the intercellular interactions involved in metastasis (4). Although fluorescence imaging (FLI) produces excellent resolution, it is restricted to superficial tissue depth due to light scattering in deep tissues. Bioluminescence imaging (BLI) allows for sensitive whole-body imaging of *luciferase*-engineered cells in preclinical animal models with increased detection depth compared to FLI but presents data with low two-dimensional resolution and minimal anatomic information. Similar to FLI, BLI still suffers from light scattering, often preventing researchers from pinpointing precise locations of reporter gene expression in deep tissues. Additionally, light attenuation by surrounding tissues may fully impede the detection of weaker signals from deeply-located and/or smaller populations of engineered cells (5). Multimodality imaging can ameliorate inherent limitations present in a single imaging modality (6-8). For example, reporter genes for magnetic resonance imaging (MRI) would provide the high resolution, 3-dimensional and quantitative information needed to complement data provided by more affordable and time-efficient optical modalities such as FLI and BLI. Hence, development of a multimodality FLI/BLI/MRI reporter system could be used to provide a more complete picture of the cellular and molecular changes occurring *in vivo* over time, including its use in studying longitudinal cancer progression and treatment response in preclinical animal models.

In recent years, MRI reporter gene development has largely focused on negative contrast technologies based on iron-accumulating proteins such as ferritin heavy chain

(FTH) and the transferrin receptor (TfR) (9). However, negative contrast in tumour microenvironments can be the result of other processes such as hemorrhage, thereby generating uncertainty in the source of the loss of contrast on MRI (10). Moreover, regions of low signal naturally exist in MR images throughout the body (e.g., lungs). Alternatively, positive contrast MRI reporter genes are also being developed (11-13). Recently, a member of the organic anion-transporting polypeptide (OATP) family of proteins, namely *Oatp1a1* (slco1a1, slc21a1, slc21a3, oatp1, OATP-1), has been established as a positive contrast MRI reporter gene based on its ability to take up a clinically-approved, liver-specific paramagnetic contrast agent called gadolinium ethoxybenzyl diethylenetriamine pentaacetic acid (Gd-EOB-DTPA; Primovist/Eovist, Bayer-Schering Pharma, Berlin, Germany) (14). Gd-EOB-DTPA-enhanced MRI performed on high-field 7-Tesla and 9.4-Tesla scanners showed contrast enhancement of *Oatp1a1*-expressing xenografts in mice following administration of high Gd-EOB-DTPA doses (approximately 25-fold greater than clinical doses) (14). An added advantage of this system is that *Oatp1a1* co-expression with *firefly luciferase* also increased BLI signal generation in engineered cells through increased intracellular uptake of the luciferase substrate D-luciferin (15). Further development and characterization of *Oatp1a1* as an MRI reporter gene with concomitant BLI enhancement would allow for its widespread use in longitudinal imaging studies of preclinical cancer models, as well as clinical MRI applications such as tracking of gene- or cell-based therapies.

Here, we established a multimodality reporter gene system composed of two distinct lentiviruses: the first lentivirus was built to co-express the fluorescence reporter *tdTomato* (tdT) with the BLI reporter human codon-optimized *firefly luciferase* (FLuc2);

and the second encoded the fluorescence reporter *zsGreen1* (zsG) co-expressed with *Oatp1a1*. Human and murine triple negative breast cancer (TNBC) cells were engineered with this system and imaged both *in vitro* and *in vivo*. Following cell implantation, orthotopic TNBC tumours in mice were longitudinally imaged for three weeks with BLI and MRI using a clinical 3-Tesla MRI scanner. Each week, pre-contrast MRI was performed on mice, followed by administration of Gd-EOB-DTPA (0.1 mmol/kg) at a dose deemed safe for use in humans (16) and post-contrast MRI. Significant MRI and BLI enhancement of *Oatp1a1*-expressing tumours was observed relative to control tumours. Moreover, as tumour growth progressed, *Oatp1a1*-based high-resolution, 3-dimensional MRI revealed intratumoral heterogeneity in signal enhancement, with enhanced MR regions containing viable fluorescent TNBC cells according to *ex vivo* microscopic analysis, and non-enhanced MR regions composed of necrotic tissue, hemorrhage, and/or non-fluorescent cells. Our studies highlight the utility of this tri-modality reporter gene system for tracking the fate of viable cancer cells over time using complementary imaging modalities. We posit that this imaging approach will have significant impact for improved monitoring of viable cancer cell growth across a broad range of preclinical solid tumour models.

2.2 Materials and Methods

2.2.1 Lentiviral Construction and Production

Third generation packaging and envelope-expression plasmids pMDLg/pRRE, pRSV-Rev, and pMD2.G were obtained (gifts from Didier Trono; Addgene plasmids #12251, #12253, and #12259, respectively), in addition to a third-generation lentiviral transfer vector encoding tdT and *firefly luciferase* (FLuc) separated by a P2A self-cleaving peptide sequence (pUltra-Chili-Luc; gift from Malcolm Moore; Addgene plasmid #48688). All cloning was performed using In-Fusion HD Cloning (Takara Bio USA, Inc.). In the pUltra-Chili-Luc vector, we first replaced FLuc with FLuc2 and then replaced the Ubiquitin C promoter with a human elongation factor 1 alpha promoter (pEF1 α) obtained from the pSelect-Zeo-SEAP Vector (Cat. psetz-seap, InvivoGen). This latter transfer vector was called pEF1 α -tdT/FLuc2. The resultant transfer vector was further cloned, using the same protocol described above, to replace *tdTomato* with the *zsGreen1* fluorescence reporter gene (zsG) sequence, obtained from the pLVX-ZsGreen1-N1 Vector (Cat. 632565, Takara Bio USA, Inc.), generating an intermediary pEF1 α -zsG/FLuc2 transfer plasmid. The LV-PGK-SO plasmid co-expressing *mStrawberry*- and *Oatp1a1* (14) was kindly provided by Dr. Kevin Brindle (University of Cambridge). The E2A-*Oatp1a1* sequence was amplified and cloned, as described above, replacing the P2A-FLuc2 sequence within pEF1 α -zsG/FLuc2 to obtain a pEF1 α -zsG/*Oatp1a1* lentiviral transfer plasmid. To produce pEF1 α -tdT/FLuc2 and pEF1 α -zsG/*Oatp1a1* lentiviruses, the packaging, envelope and one of the transfer plasmids were co-transfected into human embryonic kidney (HEK 293T) cells

using Lipofectamine 3000 (ThermoFisher Scientific) according to the manufacturer's lentiviral production protocol. Lentivirus-containing supernatants were harvested 24h and 48h post transfection, filtered through a 0.45- μ m filter, and stored at -80°C prior to use.

2.2.2 Cell Culture and Stable Cell Generation

Human embryonic kidney cells (HEK 293T), human TNBC cells (MDA-MB-231), and murine TNBC cells (4T1) were obtained from a commercial supplier (American Type Culture Collection; ATCC) and cultured in Dulbecco's Modified Eagle's Medium (DMEM) supplemented with 10% fetal bovine serum at 37°C and 5% CO₂. All cells were routinely verified as free of mycoplasma contamination using the MycoAlert mycoplasma detection kit (Lonza Group). For stable cell generation, MDA-MB-231 and 4T1 cells were first transduced with pEF1 α -tdT/FLuc2 lentivirus overnight in the presence of 4- to 8- μ g/mL polybrene. Transduced cells were washed, collected, and tdT-positive cells were sorted using a FACSAria III fluorescence-activated cell sorter (BD Biosciences), thereby generating *luciferase*-expressing cells. These *luciferase*-expressing cells were expanded, and a subset of this population was additionally transduced with pEF1 α -zsG/Oatp1a1 lentivirus and zsG-positive cells were sorted. The resulting population will be referred to as *luciferase/Oatp1a1*-expressing cells. During sorting for zsG, cells were also sorted for tdTomato fluorescence intensity that was equivalent to the original *luciferase*-expressing cells to maintain equivalent *luciferase* expression. Fluorescence intensity of expanded cell populations was

evaluated via flow cytometry using a FACSCanto flow cytometer (BD Biosciences). Fluorescence was analyzed using FlowJo software (FlowJo LLC) to validate *luciferase*- and *luciferase/Oatp1a1*-expressing cells had matched tdT fluorescence signal (i.e., matched FLuc2 expression), and sorted and validated cells were utilized for all experiments.

2.2.3 Immunofluorescence Staining

Luciferase- and *luciferase/Oatp1a1*-expressing cells were grown on glass coverslips, rinsed with PBS, and fixed with 4% paraformaldehyde (PFA) for 10 minutes. Cells were then permeabilized via 0.02% Tween 20 (Sigma-Aldrich) for 20 minutes, incubated overnight at 4°C with rabbit anti-OATP1A1 primary antibody (20 µg/ml, LS-C113034, LifeSpan BioSciences Inc.), followed by incubation with goat anti-rabbit AlexaFluor 647-conjugated secondary antibodies for two hours at room temperature (1:500 dilution, ab150079, Abcam). Coverslips were counterstained with DAPI, mounted, and imaged using a LSM Meta 510 microscope (Zeiss).

2.2.4 Proliferation Assays

Non-transduced, *luciferase*-, and *luciferase/Oatp1a1*-expressing cells (5×10^4) were seeded in 96-well plates and cell proliferation was evaluated using a tetrazolium salt (3-(4,5-dimethylthiazol-2-yl)-2,5-diphenyltetrazolium bromide, MTT) assay. Optical absorbance measurements at 590 nm were made on a

spectrophotometer at 0h, 24h and 48h post initial seeding. Measures at 24h and 48h were normalized to seeding values obtained at 0h to evaluate cell proliferation.

2.2.5 *In Vitro* Luciferase Assays

Total intracellular luciferase activity was measured on cell lysates using the Dual-Luciferase Reporter Assay System (E1910, Promega). Light production in relative light units (RLU) was measured on a GloMax 20/20 Luminometer (Promega) after mixing of 10 μ L of lysate and 5 μ L of LARII substrate. Protein concentrations were calculated using a Pierce BCA Protein Assay Kit for normalization of light production (ThermoFisher Scientific). For BLI of intact cells, 1×10^5 cells/well were seeded in 6-well plates and grown for 3 days, after which 0.15 mg/ml D-luciferin was added to each well, and plates were imaged on an IVIS Lumina XRMS *In Vivo* Imaging System (PerkinElmer). Following BLI, cells from each well were harvested and protein concentrations were measured using a Pierce BCA Protein Assay Kit. Average radiance values in photons/s/cm²/sr were measured from each well using the software LivingImage (PerkinElmer) and normalized to protein levels as a surrogate measure of cell number.

2.2.6 *In Vitro* Magnetic Resonance Imaging

Non-transduced, *luciferase*-, and *luciferase/Oatp1a1*-expressing cells (2×10^6) were seeded in T-175 flasks and grown for 3 days. Cells were incubated with media containing 1.6-mM Gd-EOB-DTPA or with media containing an equivalent volume of PBS for 90 minutes at 37°C and 5% CO₂. Cells were then

washed 3 times with PBS, trypsinized and pelleted in 0.2-mL tubes, and placed into a 2% agarose phantom mold that was incubated in a 37°C chamber for two hours to mimic body temperature. MRI was performed on a 3-T GE clinical MR scanner (General Electric Healthcare Discovery MR750 3.0 T, Milwaukee WI, U.S.A.) and a 3.5-cm diameter birdcage RF coil (Morris Instruments, Ottawa, ON, Canada). A fast spin echo inversion recovery (FSE-IR) pulse sequence was used with the following parameters: field of view (FOV) = 256×256, repetition time (TR) = 5000 ms, echo time (TE) = 19.1 ms, echo train length (ETL) = 4, number of excitations (NEX) = 1, receiver bandwidth (rBW) = 12.50 MHz, inversion times (TI) = 50, 100, 125, 150, 175, 200, 250, 350, 500, 750, 1000, 1500, 2000, 2500, 3000, in-plane resolution = 0.27 mm², slice thickness = 2.0 mm, scan time = 5 min and 25 s per inversion time. Spin-lattice relaxation rates (R_1) were determined by non-linear least-squares fitting (MATLAB, MathWorks, Natick, Massachusetts, United States) of signal intensities across the series of variable inversion time images on a pixel by pixel basis. The most common inversion recovery equation presented in the literature is as follows:

$$S = k \cdot (1 - 2e^{-\frac{TI}{T_1}} + e^{-\frac{TR}{T_1}})$$

Here, S represents the acquired signal, and k is the proportionality constant, which depends on the specific coil used, the main magnetic field, the proton density, and the temperature, amongst other factors (17). However, two practical obstacles exist that render this equation impractical for real-world applications: first, a perfect 180° pulse is never truly achieved, and second, the signal is not acquired immediately after the RF pulse (18). In practice, these real-

world limitations produce a different behavior at $TI = 0$ and $TI = \infty$ than predicted theoretical outputs dictated by the equation above. To address these limitations, and assuming $TR \gg TI$, the equation above was adjusted to the following:

$$S = M_{ss} - (M_{ss} - M_i) \cdot e^{-TI/T_1}$$

Here, if $TI = 0$, then $S = -M_i$ where M_i is simply the first value of the inversion recovery curve, independent of the final, steady state magnetization M_{ss} . Additionally, if $TI = \infty$, then $S = M_{ss}$. Finally, we use the absolute value of this last equation because the DICOM images acquired provided magnitude (non-phase) information:

$$S = \left| M_{ss} - (M_{ss} - M_i) \cdot e^{-TI/T_1} \right|$$

The zero-crossing point, the TI at which point $S = 0$, is extrapolated from the data and the R_1 of each pixel can be determined via the following relationship:

$$R_1 = \ln 2 / TI_{null}$$

2.2.7 Orthotopic Tumour Model

Animals were cared for in accordance with the standards of the Canadian Council on Animal Care, and experiments were undertaken with an approved protocol of the University of Western Ontario's Council on Animal Care (AUP 2016-026). One million *luciferase*- ($n=4$) or *luciferase/Oatp1a1*-expressing ($n=5$) MDA-

MB-231 cells, or 0.3×10^6 *luciferase*- ($n=5$) or *luciferase/Oatp1a1*-expressing ($n=5$) 4T1 cells were implanted orthotopically into the right fourth mammary fat pad of immunocompromised (Nu/Foxn1-nu) female mice (Charles River). Fluorescence imaging for *tdTomato*, BLI for *luciferase* with or without co-expression of *Oatp1a1*, and Gd-EOB-DTPA enhanced MRI for *Oatp1a1* was performed on mice according to the imaging timelines specified below. Non-specific Gd-DTPA-enhanced MRI was also performed on mice bearing *luciferase*-expressing tumours ($n=2$) or *luciferase/Oatp1a1*-expressing tumours ($n=2$) at endpoint.

2.2.8 *In Vivo* Fluorescence and Bioluminescence Imaging

FLI and BLI were performed on an IVIS Lumina XRMS *In Vivo* Imaging System (PerkinElmer). For MDA-MB-231 mice, FLI and BLI was performed on days 0, 4, 8, 12, and 16 after cell implantation. For 4T1 mice, FLI and BLI was performed on days 0, 4 and 8 after cell implantation. Mice were anesthetized with 1-2% isoflurane using a nose cone attached to an activated carbon charcoal filter for passive scavenging. FLI for *tdTomato* was performed using 554-nm excitation and 581-nm emission filters. Images were acquired with a 0.15-s exposure time. Mice were then administered 150 μ L of 30-mg/mL D-luciferin intraperitoneally and BLI images with 0.15-s exposure times were captured every 30 s for 30 minutes. Regions of interest (ROIs) were manually drawn around tumour borders using LivingImage software (PerkinElmer) to measure fluorescence radiance efficiency (μ W/cm²). The ROI of the *tdTomato* fluorescence image for each mouse on each day was then overlaid onto the corresponding BLI image, that was acquired

subsequently, to measure bioluminescent average radiance (p/s/cm²/sr). The ratio of BLI average radiance to fluorescence radiance efficiency, which we called normalized radiance in accordance with previous literature (19), was then calculated for each tumour on each day.

2.2.9 *In Vivo* Magnetic Resonance Imaging

Scans were performed on a 3-T GE clinical MR scanner (General Electric Healthcare Discovery MR750 3.0 T, Milwaukee WI, U.S.A.) using a custom-built gradient insert and a bespoke 5-cm-diameter solenoidal radiofrequency coil. For MDA-MB-231 mice, MRI was performed on days 7, 9, 14, 16, 21, and 23 after cell implantation. 4T1 mice were imaged on days 7 and 9. Mice were anesthetized with 1-2% isoflurane using a nose cone attached to an activated carbon charcoal filter for passive scavenging. T_1 -weighted images were acquired using a Spoiled Gradient Recalled Acquisition in Steady State (SPGR) pulse sequence using the following parameters: FOV = 50mm, TR = 15.8 ms, TE = 10.5 ms, rBW = 31.25 MHz, ETL = 4, Frequency and Phase 500×500, Flip Angle: 60°, NEX = 1, v 100- μ m isotropic voxels, scan time = approximately 22-24 minutes per mouse (dependent on mouse size). Pre-contrast images were acquired approximately 48 hours prior to post-Gd-EOB-DTPA imaging, on days 7, 14, and 21. For post-Gd-EOB-DTPA imaging on days 9, 16, and 23, mice were administered 0.1 mmol/kg Gd-EOB-DTPA via the tail vein and imaged on MRI 5 hours post-injection. (See timeline in **Supplementary Figure 1.**) Additionally, mice bearing *luciferase*- (n=2) and *luciferase/Oatp1a1*-expressing (n=2) MDA-MB-231 tumours at endpoint were

administered 0.1 mmol/kg gadolinium-diethylenetriamine pentaacetic acid (Gd-DTPA; Magnevist, Bayer-Schering Pharma, Berlin, Germany) and imaged 10 minutes post-injection using the scanning parameters described above. Following imaging, whole-tumours were manually segmented in three-dimensions using ITK-SNAP software and contrast-to-noise ratios relative to hind-leg muscle in all images were calculated (20).

2.2.10 Histology

Following *in vivo* experiments, mice were sacrificed via isoflurane overdose, perfused with 4% PFA through the left heart ventricle and tumours were excised from mammary fat pads. Tumours were then frozen in OCT medium (Sakura Finetek) and 10- μ m frozen sections were collected. Whole-tumour microscopy images of tdTomato fluorescence were taken using an EVOS FL Auto 2 Imaging System (Invitrogen) prior to hematoxylin/eosin (H&E) staining of the same and/or adjacent histology sections and subsequent imaging with the same microscope. For pixel-by-pixel analysis of MRI intensity to tdTomato fluorescence intensity, fluorescence microscopy images of whole-tumours were converted to the Neuroimaging Informatics Technology Initiative (NIfTI) data format (21). A blinded participant matched fluorescence microscopy images to a corresponding Gd-EOB-DTPA-enhanced MRI image plane for a *luciferase-* and *luciferase/Oatp1a1* mouse, and utilized a 15-fiducial system per image set on 3D Slicer (Version 4.31, Surgical Planning Laboratory, Brigham & Women's Hospital Boston MA, U.S.A.) to perform a non-rigid image registration using with a custom software plugin (22). Following

registration, fluorescence microscopy and Gd-EOB-DTPA-enhanced MR images of each tumour were imported into MATLAB, overlaid, and MR intensity and fluorescence intensity were each binned into 256 values. Pixels with zero-values for MR intensity and/or tdTomato fluorescence intensity were excluded from the analysis. Once MR intensity and fluorescence intensity were obtained for each pixel, the mean fluorescence intensity for each MR intensity bin was then calculated. MR intensity bins with fewer than 100 pixels were excluded from the analysis to eliminate bins with insufficient sampling numbers for meaningful calculations.

2.2.11 Statistics

Unpaired two-tailed t tests were performed using Graphpad Prism software (Version 7.00 for Mac OS X, GraphPad Software Inc., La Jolla California USA, www.graphpad.com) for cell characterization and luciferase studies. Two-way Analysis of Variance (ANOVA) and Tukey's post-hoc multiple comparisons were performed for MRI results. For pixel-by-pixel MRI-to-fluorescence image analysis, Pearson correlation tests were performed. For all tests, a nominal p -value less than 0.05 was considered statistically significant.

2.3 Results

2.3.1 Lentiviral expression of reporter genes in human and murine TNBC cells

Lentiviral transfer plasmids encoding pEF1 α -tdT/FLuc2 and pEF1 α -zsG/Oatp1a1 were successfully engineered and utilized to produce lentiviral vectors (**Figure 2.1A**). Human (MDA-MB-231) and murine (4T1) TNBC cell lines were transduced with pEF1 α -tdT/FLuc2 lentivirus and subsequently sorted for tdTomato fluorescence with >95% purity to obtain *luciferase*-expressing cells. Following sorting and expansion, a subset of *luciferase*-expressing cells was transduced a second time with pEF1 α -zsG/Oatp1a1 lentivirus and sorted again for zsGreen1 fluorescence with >95% purity whilst also matching the tdTomato intensity to that of the original *luciferase*-expressing cells (**Figure 2.1B**). OATP1A1 immunostaining confirmed absence of *Oatp1a1* expression in *luciferase*-expressing cells, whereas positive OATP1A1 staining was present in cells double transduced with the pEF1 α -zsG/Oatp1a1 lentivirus (**Figure 2.1C**), hereafter referred to as *luciferase/Oatp1a1*-expressing cells. Proliferation assays showed no difference in growth rates between non-transduced cells, *luciferase*-expressing cells, and *luciferase/Oatp1a1*-expressing cells for both human and murine TNBC cell lines.

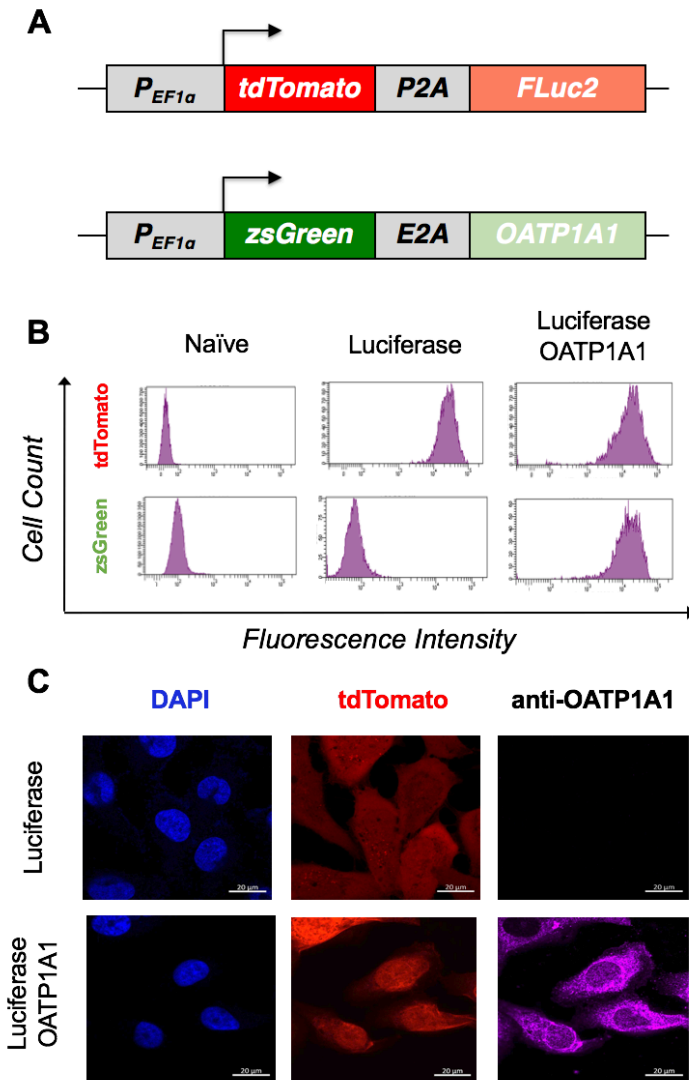


Figure 2.1. Lentiviral Engineering of Triple-Negative Breast Cancer Cells with a Multimodality Reporter Gene System. A, Reporter gene constructs for co-expression of tdT and human codon-optimized firefly luciferase (*luciferase*), and zsG and organic anion-transporting polypeptide 1a1 (*Oatp1a1*). B, Histograms of 4T1 cells engineered with the reporter gene constructs and fluorescence-activated cell sorted for tdT and zsG fluorescence. C, Anti-Oatp1a1 immunofluorescence staining of MDA-MB-231 cells engineered with tdT/luciferase lentivirus alone (Luciferase Control) or additionally engineered with zsG/Oatp1a1 lentivirus (Luciferase OATP1A1). Scale bar = 20 μm .

2.3.2 Increased BLI signal and Gd-EOB-DTPA-enhanced MRI contrast of TNBC cells co-expressing *luciferase/Oatp1a1*

To first compare luciferase activity across engineered cells excluding any contribution from OATP1A1, cell lysates were prepared and luciferase activity assays exhibited no significant difference in intracellular luciferase activity between *luciferase*- and *luciferase/Oatp1a1*-expressing cells (n=3 per group). By contrast, for cells with intact membranes, where OATP1A1 functions, MDA-MB-231 cells co-expressing *luciferase* and *Oatp1a1* exhibited a significant 5.5-fold increase in BLI signal ($4.072 \pm 0.145 \times 10^{11}$ p/s/cm²/sr/μg) relative to cells expressing *luciferase* alone ($7.432 \pm 0.515 \times 10^{10}$ p/s/cm²/sr/μg) (n=3, $p < 0.05$; **Figure 2.2A-B**). Similarly, 4T1 cells co-expressing *luciferase* and *Oatp1a1* exhibited a significant 2.6-fold increase in BLI signal ($4.091 \pm 0.383 \times 10^7$ p/s/cm²/sr/μg) relative to cells expressing *luciferase* alone ($1.603 \pm 0.068 \times 10^7$ p/s/cm²/sr/μg) (n=3, $p < 0.05$).

Next, non-transduced, *luciferase*-, and *luciferase/Oatp1a1*-expressing cells were incubated with or without Gd-EOB-DTPA (1.6 mM) for 90 minutes, washed thoroughly, and pelleted before being placed into an agarose cell phantom (**Figure 2.2C-D**). Inversion recovery MRI of the phantom was performed at 3T and 37°C, and spin-lattice relaxation rate (R_1) maps were generated. In the absence of Gd-EOB-DTPA, neither MDA-MB-231 (**Figure 2.2C-D**), nor 4T1 cells, displayed differences in R_1 rates between non-transduced and transduced genotypes. Further, control non-transduced and *luciferase*-expressing cells treated with Gd-EOB-DTPA did not exhibit differences in R_1 rates relative to untreated controls or

to each other. Exclusively, cells engineered to express *Oatp1a1* exhibited significantly increased R_1 rate following Gd-EOB-DTPA incubation compared to all other conditions. MDA-MB-231 cells co-expressing *Oatp1a1* demonstrated a significant 3.7-fold increase in R_1 rate following treatment with Gd-EOB-DTPA ($2.898 \pm 0.484 \text{ s}^{-1}$) relative to *luciferase*-expressing MDA-MB-231 cells ($0.848 \pm 0.011 \text{ s}^{-1}$) ($n=3$, $p<0.01$; **Figure 2.2C-D**). 4T1 cells co-expressing *Oatp1a1* demonstrated a 16.1-fold increase in R_1 rate following incubation with Gd-EOB-DTPA ($14.325 \pm 6.01 \text{ s}^{-1}$) relative to *luciferase*-expressing 4T1 cells ($0.859 \pm 0.023 \text{ s}^{-1}$) ($n=3$, $p<0.01$).

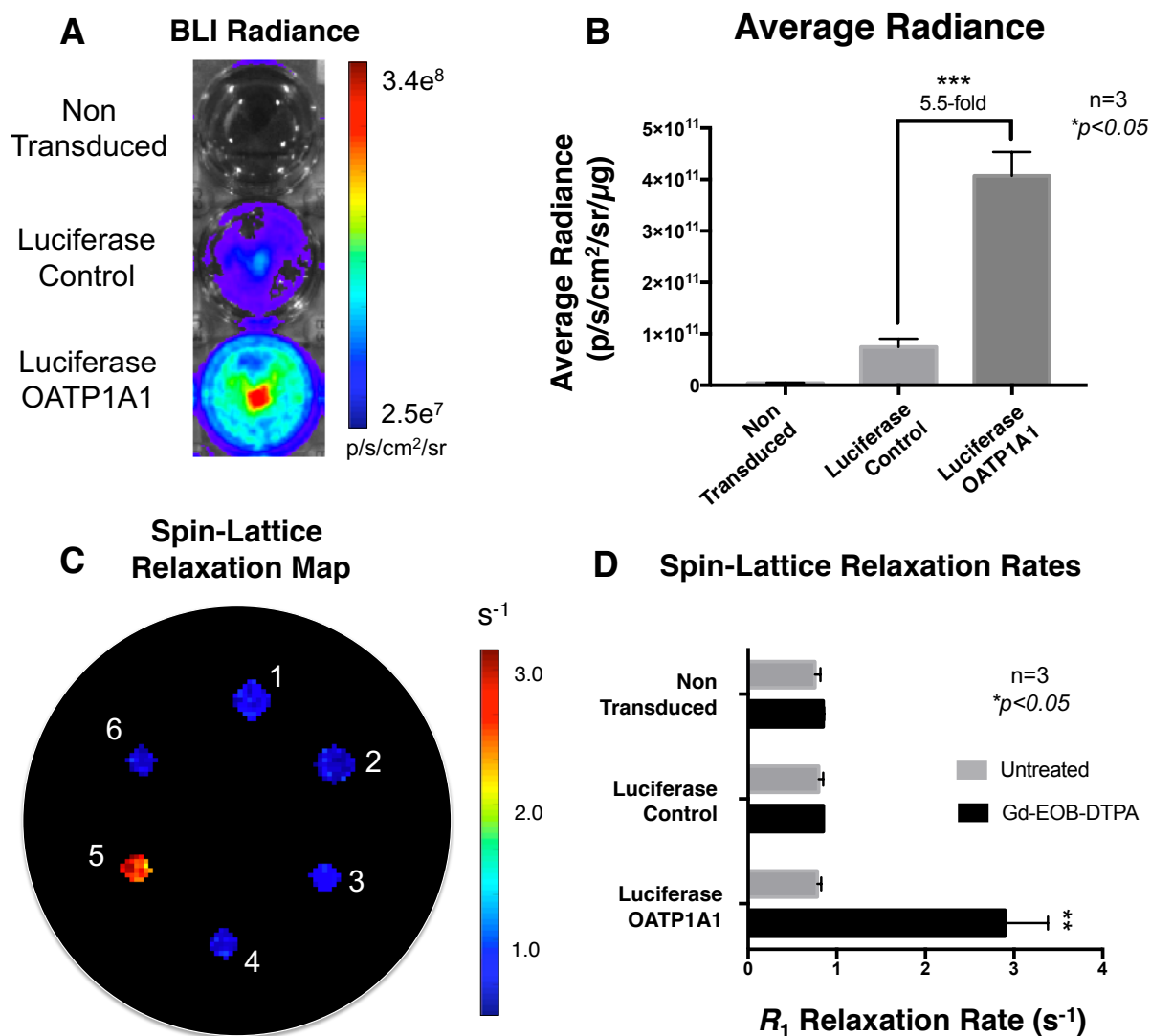


Figure 2.2. *In Vitro* Functional Characterization of Triple-Negative Breast Cancer Cells Engineered with Reporter Genes. (A) Representative well plate of non transduced, *luciferase*- (Luciferase Control), and *luciferase/Oatp1a1*-expressing (Luciferase OATP1A1) MDA-MB-231 cells imaged following administration of 1 μ L of 150 mg/mL D-Luciferin. (B) Normalized average radiance (p/s/cm²/sr/ μ g) of MDA-MB-231 cells following administration of 1 μ L of 150 mg/mL D-Luciferin (n=3, *p<0.05). (C) Spin-lattice relaxation map of representative phantom containing cell pellets of MDA-MB-231

cells either treated or untreated with 1.6 mM Gd-EOB-DTPA as follows: 1 treated non-transduced, 2 untreated non-transduced, 3 treated Luciferase Control, 4 untreated Luciferase Control, 5 treated Luciferase OATP1A1, 6 untreated Luciferase OATP1A1. (D) Spin-lattice relaxation rates (s^{-1}) of engineered and non-engineered MDA-MB-231 cells either treated or untreated with 1.6 mM Gd-EOB-DTPA ($n=3$, $*p<0.05$). Error bars indicate standard deviation.

2.3.3 *Oatp1a1* expression increases *in vivo* BLI and MRI signal of orthotopic TNBC tumours over time

Immunocompromised female mice were implanted with *luciferase*- or *luciferase/Oatp1a1*-expressing cells into the fourth mammary fat pad to generate orthotopic tumours for longitudinal FLI, BLI, and MRI. tdTomato FLI was performed to obtain relative measures of the total number of viable cells within each tumour in order to normalize BLI signals across time. As a result, average radiance measures ($\text{p/s/cm}^2/\text{sr}$) from BLI images were normalized to fluorescence efficiency measures ($\mu\text{W/cm}^2$) in FLI images to obtain measures of normalized radiance. *Luciferase/Oatp1a1*-expressing MDA-MB-231 tumours that had near-equivalent FLI signals displayed higher BLI signals than *luciferase*-expressing tumours without *Oatp1a1* (**Figure 2.3A**). At each time point, MDA-MB-231 tumours expressing both *luciferase* and *Oatp1a1* ($n=5$) exhibited significantly increased normalized radiance, relative to tumours expressing *luciferase* alone ($n=4$; $p<0.05$) (**Figure 2.3B-C**). Similarly, 4T1 tumours expressing both *luciferase* and *Oatp1a1* ($n=5$) also exhibited significantly increased normalized radiance relative to *luciferase*-expressing tumours not expressing *Oatp1a1*, averaging a 2.9-fold increase in normalized radiance ($n=5$; $p<0.05$). Collectively, pooled imaging data across all time points for MDA-MB-231 tumours were significantly higher for tumours co-expressing *Oatp1a1* compared to tumours without, averaging a 4.0-fold increase in normalized radiance.

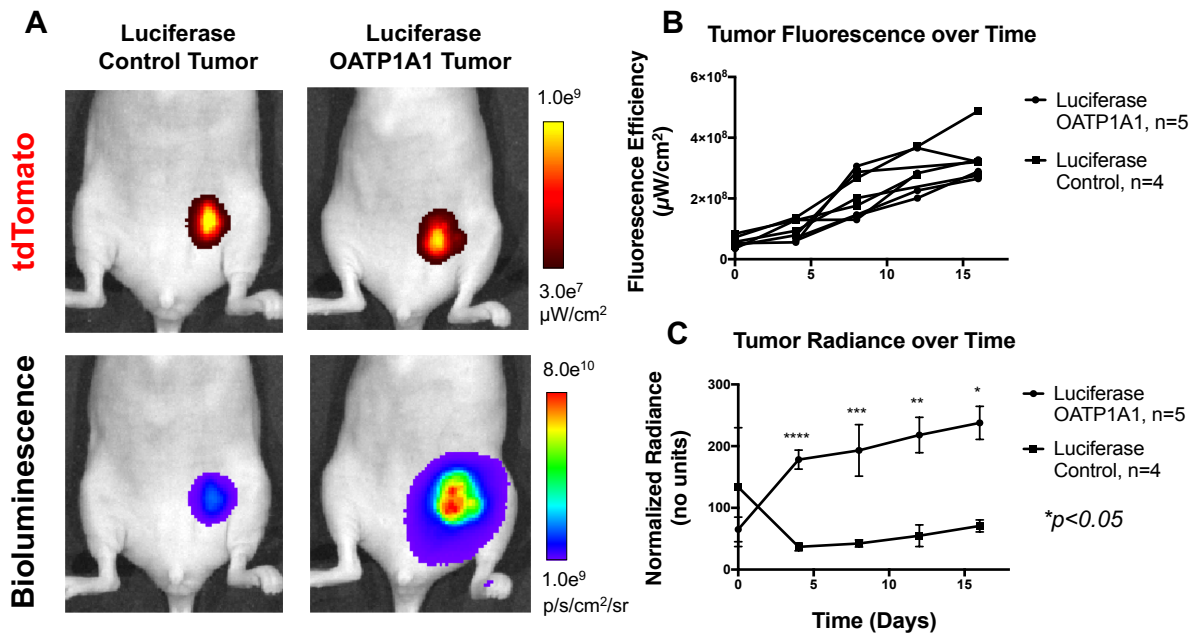


Figure 2.3. *In Vivo* Bioluminescence Enhancement via *Oatp1a1*. (A) Representative fluorescence (*top panel*) and bioluminescence (*bottom panel*) images of mice bearing MDA-MB-231 *luciferase*-expressing tumours (*left*; Luciferase Control) or MDA-MB-231 *luciferase/Oatp1a1*-expressing tumours (*right*; Luciferase OATP1A1). (B) tdTomato fluorescence efficiency ($\mu\text{W}/\text{cm}^2$) of MDA-MB-231 tumours over time. (C) Normalized radiance (no units) of MDA-MB-231 tumours over time ($*p<0.05$). Error bars indicate standard deviation.

Next, we performed Gd-EOB-DTPA-enhanced MRI of these mice on a 3 Tesla MRI scanner. Pre-contrast images of MDA-MB-231 tumours (**Figure 2.4A and 2.4C**) and 4T1 tumours exhibited no difference in CNR between *luciferase* and *luciferase/Oatp1a1* tumours across all time points. Conversely, following administration of Gd-EOB-DTPA, *luciferase/Oatp1a1* tumours showed significantly elevated CNR across all time points compared to all other conditions ($p < 0.05$; **Figure 2.4B, 2.4D, 2.4E**). Mice bearing 4T1 tumours imaged at days 7 and 9 after cell implantation showed a significant 2.6-fold increase in CNR after Gd-EOB-DTPA administration in mice bearing *luciferase/Oatp1a1* tumours relative to *luciferase*-expressing tumours ($n=5$; $p < 0.05$). Collectively, pooled data across all time points showed a significant 2.2-fold average increase in CNR for *luciferase/Oatp1a1* MDA-MB-231 tumours ($n=5$) post-contrast images relative to *luciferase* tumours ($n=4$; $p < 0.05$). Contrast enhancement consistently returned to baseline levels within 5 days following administration of Gd-EOB-DTPA (**Figure 2.4E**).

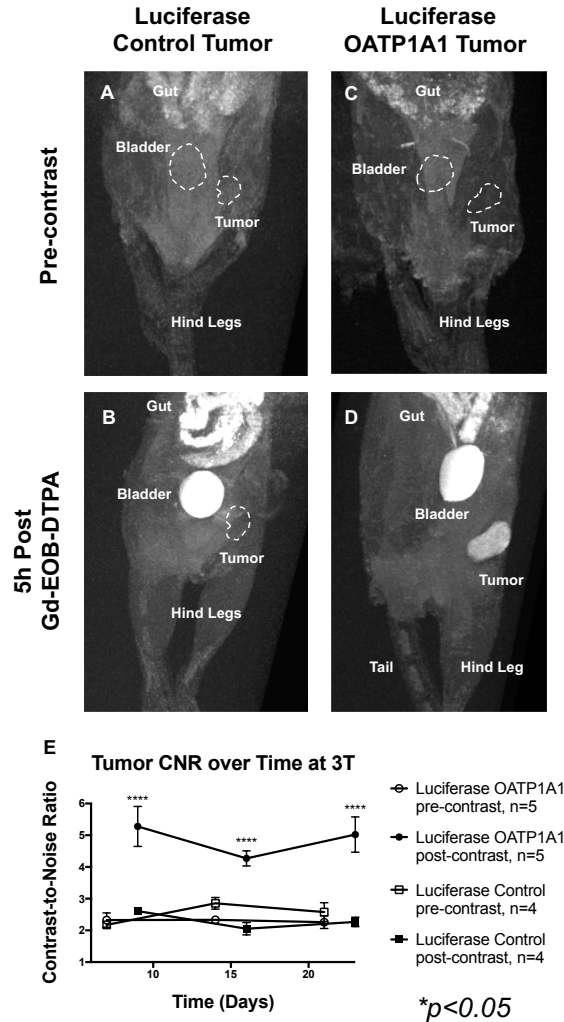


Figure 2.4. *In Vivo* MR Signal Enhancement via *Oatp1a1*. Representative T_1 -weighted 3-dimensional reconstruction of mouse bearing *luciferase*-expressing MDA-MB-231 tumour (Luciferase Control) at Day 7 (A) before and (B) 5-hours following administration of 0.1-mmol/kg Gd-EOB-DTPA at Day 9. Representative T_1 -weighted 3-dimensional reconstruction of mouse bearing *luciferase/Oatp1a1*-expressing MDA-MB-231 tumour (Luciferase OATP1A1) at Day 7 (C) before and (D) 5-hours following administration of 0.1-mmol/kg Gd-EOB-DTPA at Day 9. (E) Mean contrast-to-noise ratios (CNR) of MDA-MB-231 tumours over time (* $p < 0.05$, **** $p < 0.0001$). Error bars indicate standard deviation.

2.3.4 Bright regions in Gd-EOB-DTPA-enhanced MR images of *Oatp1a1*-expressing tumours correspond to areas of viable cancer cells in matched histological sections

Upon sacrifice, tumours were harvested and whole-tumour sections were imaged for tdTomato fluorescence, followed by H&E staining (**Figure 2.5**). *Luciferase* tumours did not display contrast enhancement and/or any patterns of heterogeneity in post-Gd-EOB-DTPA images (**Figure 2.5A**). By comparison, as in **Figure 2.4**, *luciferase/Oatp1a1* tumours imaged following Gd-EOB-DTPA (0.1 mmol/kg) administration were brighter than in pre-contrast images, and in some tumours (n=2), both enhancing and non-enhancing regions were notable (**Figure 2.5E**). Qualitatively, enhancing regions on Gd-EOB-DTPA-enhanced MRI of *luciferase/Oatp1a1* tumours corresponded to regions of increased tdTomato fluorescence intensity on matched and co-registered confocal microscopy images (**Figure 2.5H**), whereas non-enhancing regions corresponded to areas that either lacked tdTomato fluorescence or displaying overtly bright fluorescence, which were subsequently shown to be either acellular, necrotic regions (no fluorescence) or hemorrhagic regions (autofluorescence) on H&E stained sections, respectively (**Figure 2.5G**). For mice in **Figure 2.5**, MR images approximately 10 minutes post-administration of Gd-DTPA (0.1 mmol/kg) were acquired to compare contrast-enhancement distribution patterns to that with *Oatp1a1*-based Gd-EOB-DTPA enhancement (**Figure 2.5B and 2.5F**). In Gd-DTPA-enhanced images, control tumours did display heterogeneous contrast enhancement (**Figure 2.5B**, yellow contour), with enhancing regions identified to be largely lacking tdTomato fluorescence and acellular according to histology (**Figure 2.5C-D**). Importantly,

maximum contrast enhancement within *Oatp1a1*-expressing tumours is acquired 5-hours following administration of Gd-EOB-DTPA (12), once non-specific contrast enhancement has already cleared, as demonstrated by the absence of enhancement on MRI in the central region of the tumour evidently occupied by a hemorrhagic core (**Figure 2.5G**).

For quantitative pixel-by-pixel analysis, post-Gd-EOB-DTPA MR images and whole-tumour tdTomato fluorescence microscopy images of a *luciferase*- and *luciferase/Oatp1a1*-expressing tumour were successfully co-registered (**Figure 2.6**). Using the exclusion criteria described in the methods, 0.86% of pixels were eliminated from the analysis of the control *luciferase* tumour (99.14% pixels analyzed), and 0.72% of pixels from the *luciferase/Oatp1a1*-expressing tumour image analysis were eliminated (99.28% pixels analyzed). Fluorescence intensity of the *luciferase/Oatp1a1*-expressing tumour exhibited a non-zero background signal ($S_{\text{background}} = 28.8$) as well as a point of saturation in the fluorescence signal ($S_{\text{saturation}} = 53.3$); linear regression analysis was thus performed within these limits. The *luciferase/Oatp1a1*-expressing tumour exhibited a significant strong, positive correlation between MR intensity on *in vivo* Gd-EOB-DTPA-enhanced images and tdTomato fluorescence intensity on *ex vivo* histology, with a goodness-of-fit (R^2) coefficient of 0.9821 ($n=18,368$ pixels, $p<0.0001$) (**Figure 2.6A-C**). The control *luciferase*-expressing tumour did not exhibit any significant correlation between MR intensity and fluorescence intensity, with a goodness-of-fit (R^2) coefficient of 0.1992 ($n=17,270$ pixels, $p=0.17$) (**Figure 2.6D-F**).

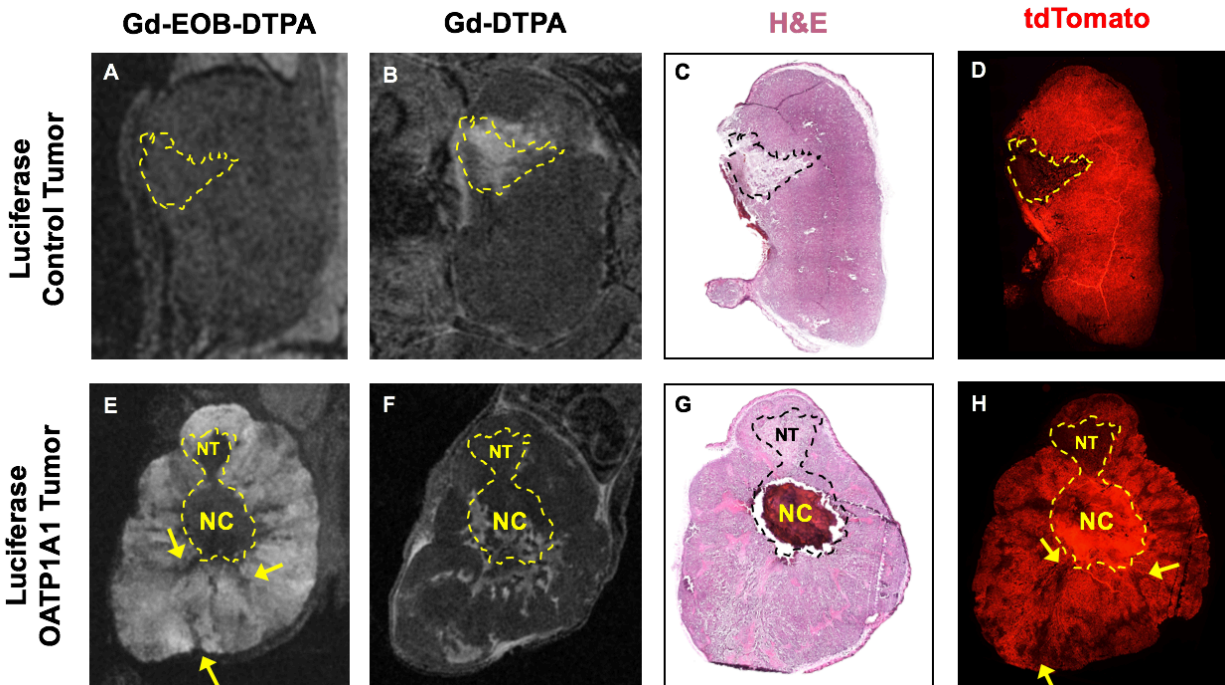


Figure 2.5. *In Vivo* Magnetic Resonance Imaging of TNBC Tumours with Corresponding Histology. *Luciferase*-expressing MDA-MB-231 tumour (Luciferase Control) (A) on Day 23, 5-hours following administration of 0.1-mmol/kg Gd-EOB-DTPA; (B) on Day 25, approximately 10 minutes following administration of 0.1-mmol/kg Gd-DTPA; along with corresponding (C) H&E staining and (D) tdTomato fluorescence microscopy. Note that this is the same tumour presented in Figure 4A-B. MDA-MB-231 tumour co-expressing *luciferase* and *Oatp1a1* (Luciferase OATP1A1) (E) on Day 23, 5-hours following administration of 0.1-mmol/kg Gd-EOB-DTPA; (F) on Day 25, approximately 10 minutes following administration of 0.1-mmol/kg Gd-DTPA; along with corresponding (G) H&E staining and (H) tdTomato fluorescence microscopy. Note that this same tumour is presented in Figure 4C-D at an earlier timepoint. Yellow contours and arrows indicate comparative features of interest. NT, non-transduced cells. NC, necrotic core hemorrhaging, which is autofluorescent in the tdTomato image.

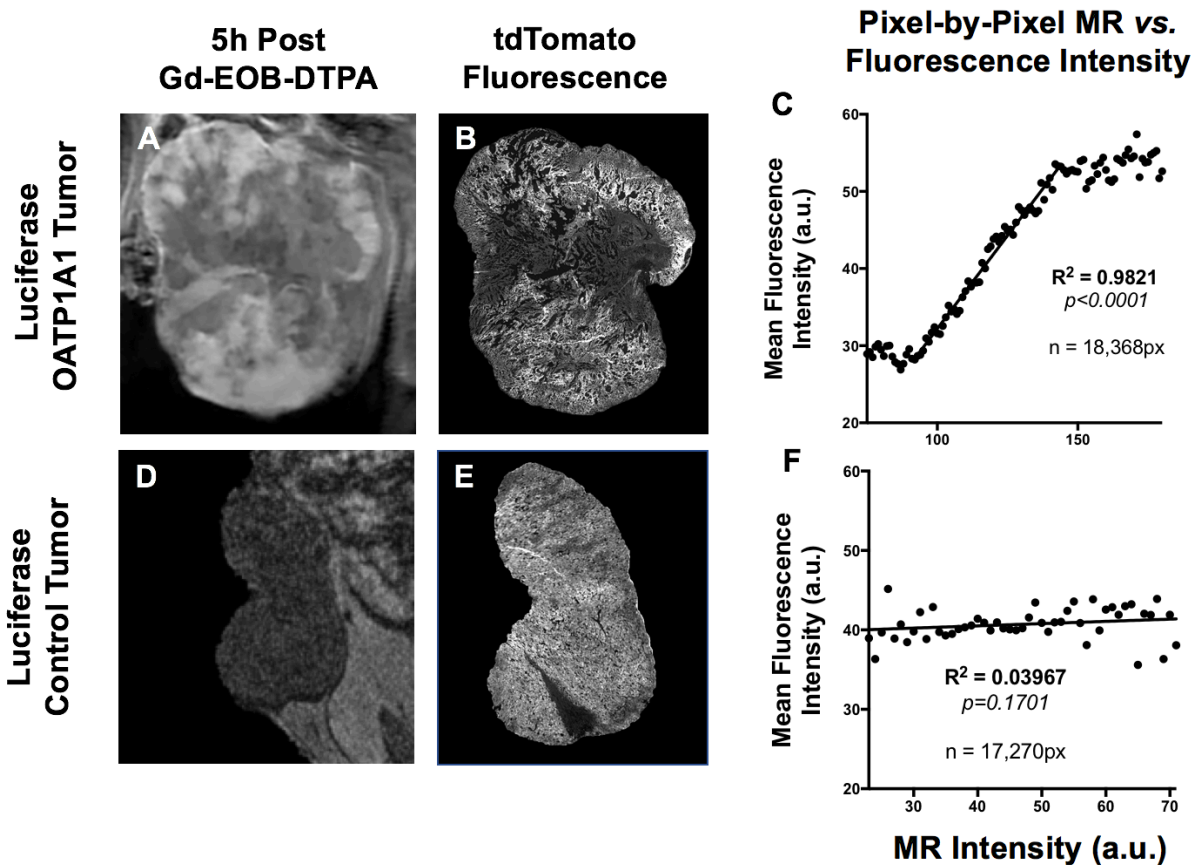


Figure 2.6. Pixelwise Analysis of *In Vivo* MR Intensity to *Ex Vivo* Fluorescence Intensity of TNBC Tumours Engineered with Reporter Genes. (A) T_1 -weighted image of MDA-MB-231 tumour co-expressing *luciferase* and *Oatp1a1* (Luciferase OATP1A1) 5-hours following administration of 0.1-mmol/kg Gd-EOB-DTPA acquired on Day 23. (B) Corresponding tdTomato fluorescence microscopy of same tumour, and (C) MR intensity vs fluorescence intensity correlation plot ($R^2=0.9821$, $p<0.0001$, $n=18,368$ pixels). (D) T_1 -weighted image of *luciferase*-expressing MDA-MB-231 tumour (Luciferase Control) 5-hours following administration of 0.1-mmol/kg Gd-EOB-DTPA acquired on Day 23. (E) Corresponding tdTomato fluorescence microscopy of same tumour, and (F) MR intensity vs fluorescence intensity correlation plot ($R^2=0.03967$, $p=0.1701$, $n=17,270$ pixels) ($*p<0.05$).

2.4 Discussion

In this study, we present a robust approach for sensitive *in vivo* multimodality tracking of viable engineered cancer cells based on *Oatp1a1*-mediated BLI and MRI contrast agent uptake. This integrated system enables time-efficient, low cost BLI for 2D monitoring of cancer cell viability, as well as 3D intratumoural cell viability measures with Gd-EOB-DTPA-enhanced MRI that is not provided by traditional MRI techniques (**Figures 2.4 and 2.5**). Gd-EOB-DTPA-enhancing regions of T_1 -weighted images of *Oatp1a1*-expressing tumours matched remarkably well with areas of viable cancer cells in matched histological images (**Figure 2.5**), which was further validated via pixel-by-pixel correlational analysis (**Figure 2.6**). The resulting strong, positive correlation between *in vivo* MRI intensity and *ex vivo* fluorescence intensity reveals a quantitative ability of *Oatp1a1*-dependent MRI to convey surrogate information on viable cancer cell distributions and densities within tumours. These tools therefore provide the ability to obtain important tumour characteristics for a better understanding of tumour architecture over time (23-25) and would be valuable for evaluating the efficacy of candidate therapies in the future.

Arguments can be made on the benefits of reporter genes operating on other modalities, particularly positron emission tomography (PET), such as the mutant herpes simplex virus type 1 thymidine kinase (HSV1-sr39tk), which offers relatively high SNR with respect to the trace amounts of contrast agent administered into the biological system (26-28). However, the spatial resolution of PET signals from reporter genes (~1 mm) are relatively poor compared to MRI

(~100 μm in-plane) (29). The strength and utility of MRI lies in its ability to generate highly resolved anatomical information in 3-dimensions. Reporter genes operating on MRI can contribute a unique advantage to this modality by providing information on precise locations of viable, specific engineered cell populations. However, many established MRI reporter genes, such as those that operate through iron-sequestration, generate undesirable negative contrast that can spread beyond precise locations of where the iron resides (i.e., a blooming artifact), obscuring underlying anatomy. Negative contrast in tumour microenvironments can be produced through other processes such as hemorrhage, thereby causing uncertainty in the source of the signal (10). Additionally, negative contrast already exists at major sites of oncogenesis and metastasis such as the lungs, hindering the ability to image ectopic negative contrast within important regions of the body (30). Iron-sequestering reporter genes have also been reported to alter phenotype and differentiation patterns in therapeutic cells, likely due to their physiologically central role in iron homeostasis and protection from oxidative stress (31). Positive contrast reporter genes for MRI have also been described in the literature. The most established class comprises of lysine-rich proteins capable of chemical exchange saturation transfer (CEST), affording the unique ability to toggle between detection and silencing of CEST signals through selective radiofrequency (RF) pulses (12). The *Oatp1a1* system operates via an entirely different contrast mechanism relative to CEST, which opens potential to track two different cell populations, or different genetic information within a single cell population, by using both CEST and *Oatp1a1* positive-contrast reporters within the same study.

Gd-EOB-DTPA and *Oatp1a1* as a positive contrast probe-reporter system offers a unique combination of advantages, which include physiological compatibility, specificity in contrast enhancement, reversibility, as well as mammalian-origin. With respect to physiological compatibility, *Oatp1a1* is biologically derived from a liver transporter protein that takes up bile acids (BAs) and specific exogenous drugs for further metabolism and/or clearance by the liver; in itself, the protein has not been reported to exhibit enzymatic or physiologically-central activity, though studies describing effects of altered *Oatp1a1* expression are very limited in number (32, 33). In our study, we did not find any quantitative differences in cell proliferation, or qualitative observations in morphology that distinguished *Oatp1a1*-expressing cells from their parental lines, supporting the notion that physiological effects are negligible as a result of its synthetic expression, though more studies are needed and are being pursued. Thus, biological imaging studies can be performed using *Oatp1a1* with little concern over any confounding effects. It is important to caution, however, that candidate therapies should be tested *in vitro* for specific uptake by *Oatp1a1* prior to performing a full preclinical animal study. Unanticipated uptake of a drug by *Oatp1a1* may result in its concentration within the tumour and, thus, a pronounced therapeutic effect may be observed that would not have occurred in the absence of *Oatp1a1* expression. For example, methotrexate has been shown to be taken up specifically by a human transporter, *Oatp1b3*, that overlaps in function with rat *Oatp1a1*, while other anti-tumour drugs such as tyrosine kinase inhibitors exhibit no uptake through this transporter (34).

The Gd-EOB-DTPA and *Oatp1a1* system additionally provides the benefits of specificity in contrast enhancement and reversibility. Traditional contrast-enhanced MRI methods for measuring tumour response to therapy in preclinical animal models are largely based on blood-pooling contrast agents such as Gd-DTPA. Though these agents offer powerful means to detect cancerous lesions, they fall short in conveying information pertaining to the distribution of viable cancer cells within the enhancing mass. For example, reduction in tumour size as measured by Gd-DTPA-enhanced MRI may be caused by eradication of non-cancerous volumes by the candidate therapy, thereby generating false positive treatment outcomes in preclinical animal studies. This is plausible when considering that it is difficult to differentiate between important, antagonistic parameters on Gd-DTPA-enhanced MRI, such as tumour recurrence and treatment necrosis (35), or vasogenic edema and infiltrative tumour (36). With *Oatp1a1*, images are acquired prior to and 5 hours post administration of Gd-EOB-DTPA, long after any non-specific contrast enhancement is cleared, allowing for a comparison of the two images for detection of engineered cancer cells with high specificity. Further, the contrast enhancement returns to baseline approximately 40 hours post-administration of Gd-EOB-DTPA, as the contrast agent washes out (14), demonstrating its reversibility, unlike other genetically-encoded reporters such as ferritin heavy chain for example, which exhibits signal persistence for more than seven days following inactivation of an established inducible promoter driving its expression (37). It is important to note, however, that these timepoints for maximal tumour CNR and washout kinetics of Gd-EOB-DTPA by *Oatp1a1*-

expressing cells are based on previous publications (12) and have not been verified in our study. The point of maximum contrast agent retention and contrast agent washout may differ between different engineered cell types and will also likely depend on the site of implantation. We do show that tumour CNR enhancement of *Oatp1a1*-expressing mammary fat pad tumours does return to pre-contrast baseline levels five days after Gd-EOB-DTPA administration (**Figure 4E**). Further, *Oatp1a1*-expressing tumours were imaged immediately following Gd-DTPA administration (n=2) two days following Gd-EOB-DTPA imaging (**Figure 2.5F**), where CNR in non-dynamic contrast enhancing regions was observed to be similar to baseline (*i.e.* pre-contrast) values. Though only anecdotal, this finding supports previous reports that Gd-EOB-DTPA contrast enhancement within *Oatp1a1*-expressing cells returns to baseline approximately two days post-administration (14).

In comparison to previous studies using high-field scanners and relatively high Gd-EOB-DTPA doses (14), we demonstrate the feasibility of the system using a 3-Tesla scanner and Gd-EOB-DTPA doses (0.1 mmol/kg) that, while approximately 4-fold the traditional dose (0.025 mmol/kg) used in the clinic, was deemed safe for patients who do not have renal impairments (16, 38). Doses up to 0.5 mmol/kg have also been used in patients (39). Recent work has been performed on a human transporter that overlaps in function with rat-derived *Oatp1a1*, namely *Oatp1b3*, where xenografts engineered to express *Oatp1b3* showed contrast enhancement following administration of Gd-EOB-DTPA using a 7-Tesla scanner (40). This human variant may mitigate immunogenicity concerns

over introducing a non-human protein into human cells for clinical translation or when performing imaging of patient-derived tumour xenografts in humanized mice (41). Future work should also evaluate the utility of rat (i.e., *Oatp1a1*) and mouse (i.e., *Oatp1* (42)) transporter proteins for performing longitudinal MRI of cancer cell viability in immunocompetent rat and mouse models, respectively. Such advances could help alleviate the use of immunogenic reporters such as GFP and luciferases for monitoring tumour progression in syngeneic immunocompetent experimental models or transgenic models.

This technology could also be applied to monitor oncotherapies in real-time, including the viability and location of engineered therapeutic cells targeting cancerous tissue (43-45), and for tracking the activation of gene-based therapies directed toward cancers (46-50). In conclusion, the promising sensitivity, specificity, positive contrast, reversibility, high resolution, and 3D spatial information generated by this multimodality reporter gene system warrant the application of *Oatp1a1* to uncover new dynamic insights about how tumours develop and respond to therapies through simultaneous fluorescence, bioluminescence, and magnetic resonance imaging.

2.5 References

1. Conn SJ, Pillman KA, Toubia J, Conn VM, Salmanidis M, Phillips CA, Roslan S, Schreiber AW, Gregory PA, Goodall GJ. The RNA binding protein quaking regulates formation of circRNAs. *Cell* 2015;160(6):1125-1134. doi: 10.1016/j.cell.2015.02.014
2. Mukherji S, Ebert MS, Zheng GXY, Tsang JS, Sharp PA, van Oudenaarden A. MicroRNAs can generate thresholds in target gene expression. *Nat Genet* 2011;43(9):854-U860. doi: 10.1038/ng.905
3. Liu H, Patel MR, Prescher JA, Patsialou A, Qian D, Lin J, Wen S, Chang YF, Bachmann MH, Shimono Y, Dalerba P, Adorno M, Lobo N, Bueno J, Dirbas FM, Goswami S, Somlo G, Condeelis J, Contag CH, Gambhir SS, Clarke MF. Cancer stem cells from human breast tumors are involved in spontaneous metastases in orthotopic mouse models. *Proc Natl Acad Sci U S A* 2010;107(42):18115-18120. doi: 10.1073/pnas.1006732107
4. Zhao M, Geller J, Ma HY, Yang M, Penman S, Hoffman RM. Monotherapy with a tumor-targeting mutant of *Salmonella typhimurium* cures orthotopic metastatic mouse models of human prostate cancer. *P Natl Acad Sci USA* 2007;104(24):10170-10174. doi: 10.1073/pnas.0703867104
5. Mezzanotte L, van 't Root M, Karatas H, Goun EA, Lowik C. In Vivo Molecular Bioluminescence Imaging: New Tools and Applications. *Trends Biotechnol* 2017;35(7):640-652. doi: 10.1016/j.tibtech.2017.03.012
6. Ray P, De A, Min JJ, Tsien RY, Gambhir SS. Imaging tri-fusion multimodality reporter gene expression in living subjects. *Cancer Res* 2004;64(4):1323-1330.

7. Giraudo C, Raderer M, Karanikas G, Weber M, Kiesewetter B, Dolak W, Simonitsch-Klupp I, Mayerhoefer ME. 18F-Fluorodeoxyglucose Positron Emission Tomography/Magnetic Resonance in Lymphoma: Comparison With 18F-Fluorodeoxyglucose Positron Emission Tomography/Computed Tomography and With the Addition of Magnetic Resonance Diffusion-Weighted Imaging. *Invest Radiol* 2016;51(3):163-169. doi: 10.1097/RLI.0000000000000218
8. Seith F, Gatidis S, Schmidt H, Bezrukov I, la Fougere C, Nikolaou K, Pfannenbergl C, Schwenzer N. Comparison of Positron Emission Tomography Quantification Using Magnetic Resonance- and Computed Tomography-Based Attenuation Correction in Physiological Tissues and Lesions: A Whole-Body Positron Emission Tomography/Magnetic Resonance Study in 66 Patients. *Invest Radiol* 2016;51(1):66-71. doi: 10.1097/RLI.0000000000000208
9. Gilad AA, Ziv K, McMahon MT, van Zijl PC, Neeman M, Bulte JW. MRI reporter genes. *J Nucl Med* 2008;49(12):1905-1908. doi: 10.2967/jnumed.108.053520
10. Grimm SA, DeAngelis LM. Intratumoral hemorrhage after thrombolysis in a patient with glioblastoma multiforme. *Neurology* 2007;69(9):936. doi: 10.1212/01.wnl.0000265392.03231.ac
11. Vande Velde G, Himmelreich U, Neeman M. Reporter gene approaches for mapping cell fate decisions by MRI: promises and pitfalls. *Contrast Media Mol Imaging* 2013;8(6):424-431. doi: 10.1002/cmml.1590
12. Gilad AA, McMahon MT, Walczak P, Winnard PT, Jr., Raman V, van Laarhoven HW, Skoglund CM, Bulte JW, van Zijl PC. Artificial reporter gene providing MRI contrast based on proton exchange. *Nat Biotechnol* 2007;25(2):217-219. doi: 10.1038/nbt1277

13. Yang C, Tian R, Liu T, Liu G. MRI Reporter Genes for Noninvasive Molecular Imaging. *Molecules* 2016;21(5). doi: 10.3390/molecules21050580
14. Patrick PS, Hammersley J, Loizou L, Kettunen MI, Rodrigues TB, Hu DE, Tee SS, Hesketh R, Lyons SK, Soloviev D, Lewis DY, Aime S, Fulton SM, Brindle KM. Dual-modality gene reporter for in vivo imaging. *Proc Natl Acad Sci U S A* 2014;111(1):415-420. doi: 10.1073/pnas.1319000111
15. Patrick PS, Lyons SK, Rodrigues TB, Brindle KM. Oatp1 enhances bioluminescence by acting as a plasma membrane transporter for D-luciferin. *Mol Imaging Biol* 2014;16(5):626-634. doi: 10.1007/s11307-014-0741-4
16. Dohr O, Hofmeister R, Treher M, Schweinfurth H. Preclinical safety evaluation of Gd-EOB-DTPA (Primovist). *Invest Radiol* 2007;42(12):830-841. doi: 10.1097/RLI.0b013e318137a471
17. Rydberg JN, Hammond CA, Huston J, 3rd, Jack CR, Jr., Grimm RC, Riederer SJ. T1-weighted MR imaging of the brain using a fast inversion recovery pulse sequence. *J Magn Reson Imaging* 1996;6(2):356-362. doi: 10.1002/jmri.1880060216
18. Bydder GM, Young IR. MR imaging: clinical use of the inversion recovery sequence. *J Comput Assist Tomogr* 1985;9(4):659-675.
19. Gregor C, Gwosch KC, Sahl SJ, Hell SW. Strongly enhanced bacterial bioluminescence with the lux operon for single-cell imaging. *Proc Natl Acad Sci U S A* 2018;115(5):962-967. doi: 10.1073/pnas.1715946115
20. Yushkevich PA, Yang G, Gerig G. ITK-SNAP: An interactive tool for semi-automatic segmentation of multi-modality biomedical images. *Conf Proc IEEE Eng Med Biol Soc* 2016;2016:3342-3345. doi: 10.1109/EMBC.2016.7591443

21. Li X, Morgan PS, Ashburner J, Smith J, Rorden C. The first step for neuroimaging data analysis: DICOM to NIfTI conversion. *J Neurosci Methods* 2016;264:47-56. doi: 10.1016/j.jneumeth.2016.03.001
22. Gibson E, Crukley C, Gaed M, Gomez JA, Moussa M, Chin JL, Bauman GS, Fenster A, Ward AD. Registration of prostate histology images to ex vivo MR images via strand-shaped fiducials. *J Magn Reson Imaging* 2012;36(6):1402-1412. doi: 10.1002/jmri.23767
23. Visan I. Tumor architecture. *Nat Immunol* 2018;19(3):206. doi: 10.1038/s41590-018-0061-y
24. Kaushik S, Pickup MW, Weaver VM. From transformation to metastasis: deconstructing the extracellular matrix in breast cancer. *Cancer Metastasis Rev* 2016;35(4):655-667. doi: 10.1007/s10555-016-9650-0
25. Glasner A, Levi A, Enk J, Isaacson B, Viukov S, Orlanski S, Scope A, Neuman T, Enk CD, Hanna JH, Sexl V, Jonjic S, Seliger B, Zitvogel L, Mandelboim O. NKp46 Receptor-Mediated Interferon-gamma Production by Natural Killer Cells Increases Fibronectin 1 to Alter Tumor Architecture and Control Metastasis. *Immunity* 2018;48(2):396-398. doi: 10.1016/j.immuni.2018.01.010
26. Yaghoubi SS, Gambhir SS. PET imaging of herpes simplex virus type 1 thymidine kinase (HSV1-tk) or mutant HSV1-sr39tk reporter gene expression in mice and humans using [¹⁸F]FHBG. *Nat Protoc* 2006;1(6):3069-3075. doi: 10.1038/nprot.2006.459
27. Keu KV, Witney TH, Yaghoubi S, Rosenberg J, Kurien A, Magnusson R, Williams J, Habte F, Wagner JR, Forman S, Brown C, Allen-Auerbach M, Czernin J, Tang W, Jensen MC, Badie B, Gambhir SS. Reporter gene imaging of targeted T cell

- immunotherapy in recurrent glioma. *Sci Transl Med* 2017;9(373). doi:
10.1126/scitranslmed.aag2196
28. Yaghoubi SS, Campbell DO, Radu CG, Czernin J. Positron emission tomography reporter genes and reporter probes: gene and cell therapy applications. *Theranostics* 2012;2(4):374-391. doi: 10.7150/thno.3677
29. Moses WW. Fundamental Limits of Spatial Resolution in PET. *Nucl Instrum Methods Phys Res A* 2011;648 Supplement 1:S236-S240. doi:
10.1016/j.nima.2010.11.092
30. Ferlay J, Shin HR, Bray F, Forman D, Mathers C, Parkin DM. Estimates of worldwide burden of cancer in 2008: GLOBOCAN 2008. *Int J Cancer* 2010;127(12):2893-2917. doi: 10.1002/ijc.25516
31. Pereira SM, Moss D, Williams SR, Murray P, Taylor A. Overexpression of the MRI Reporter Genes Ferritin and Transferrin Receptor Affect Iron Homeostasis and Produce Limited Contrast in Mesenchymal Stem Cells. *Int J Mol Sci* 2015;16(7):15481-15496. doi: 10.3390/ijms160715481
32. Zhang Y, Csanaky IL, Lehman-McKeeman LD, Klaassen CD. Loss of organic anion transporting polypeptide 1a1 increases deoxycholic acid absorption in mice by increasing intestinal permeability. *Toxicol Sci* 2011;124(2):251-260. doi:
10.1093/toxsci/kfr236
33. Xu C, Zhu L, Chan T, Lu X, Shen W, Gillies MC, Zhou F. The altered renal and hepatic expression of solute carrier transporters (SLCs) in type 1 diabetic mice. *PLoS One* 2015;10(3):e0120760. doi: 10.1371/journal.pone.0120760

34. Durmus S, van Hoppe S, Schinkel AH. The impact of Organic Anion-Transporting Polypeptides (OATPs) on disposition and toxicity of antitumor drugs: Insights from knockout and humanized mice. *Drug Resist Updat* 2016;27:72-88. doi: 10.1016/j.drug.2016.06.005
35. Verma N, Cowperthwaite MC, Burnett MG, Markey MK. Differentiating tumor recurrence from treatment necrosis: a review of neuro-oncologic imaging strategies. *Neuro Oncol* 2013;15(5):515-534. doi: 10.1093/neuonc/nos307
36. Artzi M, Liberman G, Blumenthal DT, Aizenstein O, Bokstein F, Ben Bashat D. Differentiation between vasogenic edema and infiltrative tumor in patients with high-grade gliomas using texture patch-based analysis. *J Magn Reson Imaging* 2018. doi: 10.1002/jmri.25939
37. He X, Cai J, Li H, Liu B, Qin Y, Zhong Y, Wang L, Liao Y. In Vivo magnetic resonance imaging of xenografted tumors using FTH1 reporter gene expression controlled by a tet-on switch. *Oncotarget* 2016;7(48):78591-78604. doi: 10.18632/oncotarget.12519
38. Runge VM. Safety of the Gadolinium-Based Contrast Agents for Magnetic Resonance Imaging, Focusing in Part on Their Accumulation in the Brain and Especially the Dentate Nucleus. *Invest Radiol* 2016;51(5):273-279. doi: 10.1097/RLI.0000000000000273
39. Schuhmann-Giampieri G, Mahler M, Roll G, Maibauer R, Schmitz S. Pharmacokinetics of the liver-specific contrast agent Gd-EOB-DTPA in relation to contrast-enhanced liver imaging in humans. *J Clin Pharmacol* 1997;37(7):587-596.

40. Wu MR, Liu HM, Lu CW, Shen WH, Lin IJ, Liao LW, Huang YY, Shieh MJ, Hsiao JK. Organic anion-transporting polypeptide 1B3 as a dual reporter gene for fluorescence and magnetic resonance imaging. *FASEB J* 2018;32(3):1705-1715. doi: 10.1096/fj.201700767R
41. Ansari AM, Ahmed AK, Matsangos AE, Lay F, Born LJ, Marti G, Harmon JW, Sun Z. Cellular GFP Toxicity and Immunogenicity: Potential Confounders in in Vivo Cell Tracking Experiments. *Stem Cell Rev* 2016;12(5):553-559. doi: 10.1007/s12015-016-9670-8
42. Hagenbuch B, Adler ID, Schmid TE. Molecular cloning and functional characterization of the mouse organic-anion-transporting polypeptide 1 (Oatp1) and mapping of the gene to chromosome X. *Biochem J* 2000;345 Pt 1:115-120.
43. Joyce JA, Fearon DT. T cell exclusion, immune privilege, and the tumor microenvironment. *Science* 2015;348(6230):74-80. doi: 10.1126/science.aaa6204
44. Fesnak AD, June CH, Levine BL. Engineered T cells: the promise and challenges of cancer immunotherapy. *Nat Rev Cancer* 2016;16(9):566-581. doi: 10.1038/nrc.2016.97
45. Yin PT, Shah S, Pasquale NJ, Garbuzenko OB, Minko T, Lee KB. Stem cell-based gene therapy activated using magnetic hyperthermia to enhance the treatment of cancer. *Biomaterials* 2016;81:46-57. doi: 10.1016/j.biomaterials.2015.11.023
46. Naldini L. Gene therapy returns to centre stage. *Nature* 2015;526(7573):351-360. doi: 10.1038/nature15818
47. Qiu N, Liu X, Zhong Y, Zhou Z, Piao Y, Miao L, Zhang Q, Tang J, Huang L, Shen Y. Esterase-Activated Charge-Reversal Polymer for Fibroblast-Exempt Cancer Gene Therapy. *Adv Mater* 2016;28(48):10613-10622. doi: 10.1002/adma.201603095

48. Morgan RA, Chinnasamy N, Abate-Daga D, Gros A, Robbins PF, Zheng Z, Dudley ME, Feldman SA, Yang JC, Sherry RM, Phan GQ, Hughes MS, Kammula US, Miller AD, Hessman CJ, Stewart AA, Restifo NP, Quezado MM, Alimchandani M, Rosenberg AZ, Nath A, Wang T, Bielekova B, Wuest SC, Akula N, McMahon FJ, Wilde S, Mosetter B, Schendel DJ, Laurencot CM, Rosenberg SA. Cancer regression and neurological toxicity following anti-MAGE-A3 TCR gene therapy. *J Immunother* 2013;36(2):133-151. doi: 10.1097/CJI.0b013e3182829903
49. Duarte S, Carle G, Faneca H, de Lima MC, Pierrefite-Carle V. Suicide gene therapy in cancer: where do we stand now? *Cancer Lett* 2012;324(2):160-170. doi: 10.1016/j.canlet.2012.05.023
50. Lewin M, Clement O, Belguise-Valladier P, Tran L, Cuenod CA, Siauve N, Frija G. Hepatocyte targeting with Gd-EOB-DTPA: potential application for gene therapy. *Invest Radiol* 2001;36(1):9-14.

CHAPTER 3 Whole-Body, Sensitive Visualization of Spontaneous Metastasis in Mice using the *Oatp1b3* MRI Reporter System

Rationale. Metastasis is the leading cause of cancer-related deaths. However, 75% of preclinical cancer studies do not examine metastasis, focusing only on primary tumour growth, in part due to a lack of technologies for accurate quantification of metastatic spread over time. To better understand the metastatic process and advance our ability to test therapies targeting metastatic disease, tools for accurate spatiotemporal quantification of metastasis are needed. Our objective was to assess *Oatp1b3* for whole-body *in vivo* tracking of cancer cells in a spontaneous metastasis model.

Methods. Breast cancer cells were engineered with lentivirus to express *luciferase* for bioluminescence imaging (BLI). A subset of these cells was additionally engineered to co-express *Oatp1b3* for MRI. Luciferase control (Luc-CTL) or luciferase/*Oatp1b3* (Luc-1B3) cells were implanted into the 4th mammary fat pad of female mice. BLI and T_1 -weighted 3T-MRI was performed before and after 1-mmol/kg Gd-EOB-DTPA injection.

Results. Macro-metastases ($>1\text{mm}^3$) located at axillary lymph nodes exhibited significantly increased MR signal intensity in Luc-1B3 mice on post-contrast images relative to pre-contrast images, and to Luc-CTL mice both pre- and post-contrast ($n=3$, $p<0.0001$). Importantly, numerous micro-metastases ($<1\text{mm}^3$) were detected throughout lungs of Luc-1B3 mice on post-contrast MRI, which were not detected in corresponding pre-contrast MRI, with BLI, nor on post-contrast images of Luc-CTL mice. Analyzing mean signal intensity and volume of individual foci ($N=60$ across 3 mice) demonstrated that lesions around 0.01mm^3 , correlating to $\sim 10^4$ cells, could be detected. A Luc-1B3 cohort ($n=7$) was imaged over time, and metastasis was first detected at the ipsilateral

axillary lymph node, with significantly increased MR signal intensity relative to surrounding muscle tissue ($p < 0.0001$). Follow-up MRI at 20-days post-implantation revealed tumor growth at the initial ipsilateral axillary lymph node lesion, as well as subsequent metastases at other loci, including the contralateral axillary and ipsilateral brachial lymph nodes. These subsequent metastases were not at all detectable with BLI. **Conclusions.** BLI provides whole-body information on locations of engineered cells, but smaller populations can go undetected. *Oatp1b3*-MRI mitigates these limitations for effective tracking of metastatic spread. We show that this reporter can dynamically track the metastatic process at its earliest stages, including small single lymph node lesions. At late stages, we demonstrate its superiority over BLI to track cancer spread to multiple lymph nodes and other organs such as the lungs. *Oatp1b3* fulfills a long-standing gap in our ability to accurately study metastatic disease over time, and offers a path towards deep-tissue tracking of any *Oatp1b3*-engineered cell type with combined high resolution, sensitivity, 3D spatial information, and surrounding anatomical context.

3.1 Introduction

Metastatic disease is responsible for over 90% of cancer-related mortalities (1). Preclinical animal models provide an essential platform for the study of metastasis, intermediate to reductionist *in vitro* research and clinical investigations. Yet, approximately 75% of preclinical animal studies do not investigate metastasis to any extent, and instead focus only on primary tumour models. This is often due to a lack of technologies for sensitive longitudinal quantification of metastatic spread (2). Bioluminescence imaging (BLI) is frequently used for assessing metastatic burden because of its high throughput and sensitivity; however, assessing total burden with BLI, particularly in spontaneous metastasis models, remains challenging due to light scatter and attenuation by surrounding tissues (3). Small superficial lesions cannot be readily differentiated from larger lesions in deep tissues, and light from large superficial tumors complicates detection of deeper lesions. To address these limitations, preclinical oncology studies focused on examining metastatic disease have supplemented BLI observations with parallel methods, such as multi-modality imaging (4-6) and/or *ex vivo* analysis of whole-body or whole-organ systems (7, 8). For example, BLI has been paired with tissue clearing protocols, light-sheet microscopy and computational methods for sensitive imaging of metastatic cells at endpoint (9). In contrast, sensitive, high resolution, 3-dimensional dynamic tracking of metastatic spread in alive animals remains an elusive goal (10).

To better understand the metastatic process and advance our ability to test therapies targeting metastatic disease, tools for accurate spatiotemporal

quantification of metastasis are needed. As a modality, magnetic resonance imaging (MRI) uniquely provides versatile, high resolution, 3-dimensional spatial information, with surrounding anatomical context. Further, MRI is the standard of care for detection and monitoring of cancer and many other diseases. Contrast-enhanced MRI can be used to visualize tumours due to leaky vasculature, however small tumours often go undetected with these methods. The use of reporter genes to enhance the conspicuity of engineered cancer cells may improve our ability to track these cells dynamically. Several MRI reporter genes have been developed including those providing either positive (11, 12) or negative (13-16) contrast on proton-MRI, diffusion-weighted MRI (17), chemical-exchange saturation transfer MRI (18), or hyperpolarized MRI (19, 20). Despite these efforts, MRI reporter genes have often been overlooked in cancer cell tracking applications due to a perception that they provide limited imaging sensitivity, *i.e.* labelled metastatic lesions would have to be quite large before enough signal is generated for detection (21). Recent development of *Organic Anion-Transporting Polypeptide 1 (Oatp1)* has demonstrated the possibility for sensitive, positive contrast MRI of engineered cells (22-24). Specifically, *Oatp1* encodes expression of a transporter on the surface of cells that is capable of taking up the paramagnetic contrast agent gadolinium ethoxybenzyl diethylene triamine pentaacetic acid (Gd-EOB-DTPA), thereby generating positive contrast on T_1 -weighted images. Although previous studies have focused on primary tumour models, optimization of experimental parameters including contrast agent concentration, field strength and choice of pulse sequence could facilitate

sensitive whole-body *in vivo* detection of metastasizing cells. The objective of this study therefore was to evaluate the use of whole-body MRI to track *Oatp1b3*-expressing cancer cells in a spontaneous murine breast cancer metastasis model. The ability to track spontaneously metastasizing cancer cells in preclinical animal models in real-time, with sensitivity, high resolution, and 3-dimensional spatial information could offer new insights into complex metastatic mechanisms, and provide a new approach towards assessing the efficacy of candidate therapies for treatment of metastatic disease.

3.2 Materials and Methods

3.2.1. Lentiviral Construction and Production

Lentiviral transfer plasmids co-encoding *tdTomato* fluorescent protein with *firefly luciferase 2* (25), and *zsGreen* fluorescent protein with *Oatp1b3* (26) were previously cloned. The cDNA for *Organic anion transporting polypeptide 1b1* (*Oatp1b1*) was acquired from the hOATP1B1/SLCO1B1 VersaClone cDNA Vector (Cat. RDC1113, R&D Systems, Minneapolis, Minnesota, United States). A lentiviral transfer plasmid co-encoding *zsGreen* with *Oatp1b1* was cloned using the In-Fusion HD Cloning kit (Takara Bio USA Inc, Madison, Wisconsin, United States). Third-generation packaging and envelope-expression plasmids (pMDLg/pRRE, pRSV-Rev, and pMD2.G, Addgene plasmids: #12251, #12253, and #12259, respectively; gifts from Didier Trono) were co-transfected with each of the three transfer plasmids (*tdTomato/Luciferase*, *zsGreen/Oatp1b1*, *zsGreen/Oatp1b3*) into human embryonic kidney (HEK 293T) cells using Lipofectamine 3000 according to the manufacturer's lentiviral production protocol (Thermo Fisher Scientific Inc., Waltham, Massachusetts, United States). Lentivirus-containing supernatants were harvested 24h and 48h post transfection, filtered through a 0.45- μ m filter, and used immediately for transductions.

3.2.2. Cell Culture and Stable Cell Generation

Human embryonic kidney (HEK 293T) and human triple negative breast cancer cells (MDA-MB-231) were obtained from a commercial supplier (American

Type Culture Collection, Manassas, Virginia, United States) and cultured in Dulbecco's Modified Eagle's Medium (DMEM) supplemented with 10% fetal bovine serum at 37°C and 5% CO₂. All cells were routinely verified as free of mycoplasma contamination using the MycoAlert mycoplasma detection kit (Lonza Group, Basel, Switzerland). MDA-MB-231 cells were first transduced with lentivirus co-encoding *tdTomato* and *Firefly Luciferase*, and fluorescence-activated cell sorting was performed to sort for *tdTomato*-positive cells using a FACSAria III cell sorter (BD Biosciences, Mississauga, Ontario, Canada). The sorted cells were expanded and transduced again with lentivirus co-encoding *zsGreen* with either *Oatp1b1* or *Oatp1b3* and fluorescence-activated cell sorting was performed to select for *tdTomato* and *zsGreen* double-positive cells using equivalent intensity-gating for each colour. Sorted cells, hereon referred to as either *Luc-CTL*, *Luc-1B1* or *Luc-1B3* cells, were utilized for all experiments.

3.2.3. *In Vitro* Bioluminescence Imaging

Luciferase- and *Oatp1b3*-expressing cells were seeded into 24-well plates with the following numbers of cells per well: 1×10^6 , 5×10^5 , 3×10^5 , 1×10^5 , and 5×10^4 . Immediately after seeding, 0.15 mg/ml D-luciferin was added to each well, and plates were imaged on an IVIS Lumina XRMS *In Vivo* Imaging System (PerkinElmer, Waltham, Massachusetts, United States). Average radiance values in photons/s/cm²/sr were measured from each well using LivingImage software (PerkinElmer, Waltham, Massachusetts, United States).

3.2.4. Western Blot

A million *Luc-CTL*, *Luc-1B1* or *Luc-1B3* cells were washed three times in PBS and incubated with 200- μ L 4°C RIPA buffer and protease inhibitors for 30 minutes. Lysates were collected and sonicated with five 5.0-s 40 kHz bursts before being centrifuged at 13,000G for 20 minutes at 4°C. Supernatants were collected, quantified and 40 μ g of protein from each sample was loaded into an acrylamide gel composed of a 4.0% stacking layer buffered at pH 6.8 and a 15% separation layer buffered at pH 8.8. Gel electrophoresis was performed for 20 minutes at 90V and 1 hour at 110V. Protein was transferred to a nitrocellulose membrane for 7.5 minutes via the iBlot™ 2 Gel Transfer Device (IB21001, Thermo Fisher Scientific, Waltham, Massachusetts, United States) and blocked with 0.05% Tween-20, 3% BSA solution for 30 minutes. Rabbit anti-Oatp1b3 antibody (1:1000 dilution, ab139120, Abcam, Cambridge, United Kingdom) was added and incubated overnight at 4°C. The blot was washed 3x with 0.05% Tween-20 solution for 10 minutes and Goat anti-Rabbit 790-nm antibody (1:10,000 dilution, A11369, Thermo Fisher Scientific, Waltham, Massachusetts, United States) was added for 45 minutes at room temperature. The blot was washed again 3x with 0.05% Tween-20 solution for 10 minutes and imaged on the Odyssey CLx Imaging System (LI-COR Biosciences, Lincoln, Nebraska, United States).

3.2.5. *In Vitro* Magnetic Resonance Imaging

Luciferase- and *Oatp1b3*-expressing cells (1×10^6) were seeded in individual 15-cm dishes and grown for 3 days. Cells were incubated with media containing 1.6-mM Gd-EOB-DTPA or 1.6-mM Gd-DTPA (control) for 60 minutes at 37°C and 5% CO₂. In a separate experiment, cells were also incubated with media containing 16-mM Gd-EOB-DTPA or 16-mM Gd-DTPA (control) for 60 minutes at 37°C and 5% CO₂. Cells were subsequently washed 3 times with PBS, trypsinized and pelleted in 0.2-mL tubes. MRI was performed on a 3-T GE clinical MR scanner (General Electric Healthcare Discovery MR750 3.0 T, Milwaukee, Wisconsin, United States) using a 3.5-cm-diameter birdcage RF coil (Morris Instruments, Ottawa, Ontario, Canada). Imaging data were acquired at 19.5°C with a fast spin echo inversion recovery (FSE-IR) pulse sequence using the following parameters: Matrix size = 256×256, repetition time (TR) = 5000 ms, echo time (TE) = 19.1 ms, echo train length (ETL) = 4, number of excitations (NEX) = 1, receiver bandwidth (rBW) = 12.50 kHz, inversion times (TI) = 20, 35, 50, 100, 125, 150, 175, 200, 250, 350, 500, 750, 1000, 1500, 2000, 2500, 3000, in-plane resolution = 0.2×0.2 mm², slice thickness = 2.0 mm, acquisition time = 5 min and 25 s (per inversion time). Spin-lattice relaxation rates (R_1) were determined by non-linear least-squares fitting (MATLAB, MathWorks, Natick, Massachusetts, United States) of signal intensities across the series of variable inversion time images on a pixel by pixel basis. The most common inversion recovery equation presented in the literature is as follows:

$$S = k \cdot \left(1 - 2e^{-\frac{TI}{T_1}} + e^{-\frac{TR}{T_1}}\right)$$

Here, S represents the acquired signal, and k is the proportionality constant, which depends on the specific coil used, the main magnetic field, the proton density, and the temperature, amongst other factors (27). However, two practical obstacles exist that render this equation impractical for real-world applications: first, a perfect 180° pulse is never truly achieved, and second, the signal is not acquired immediately after the RF pulse (28). In practice, these real-world limitations produce a different behavior at $TI = 0$ and $TI = \infty$ than predicted theoretical outputs dictated by the equation above. To address these limitations, and assuming $TR \gg TI$, the equation above was adjusted to the following:

$$S = M_{SS} - (M_{SS} - M_i) \cdot e^{-TI/T_1}$$

Here, if $TI = 0$, then $S = -M_i$ where M_i is simply the first value of the inversion recovery curve, independent of the final, steady state magnetization M_{SS} . Additionally, if $TI = \infty$, then $S = M_{SS}$. Finally, we use the absolute value of this last equation because the DICOM images acquired provided magnitude (non-phase) information:

$$S = \left| M_{SS} - (M_{SS} - M_i) \cdot e^{-TI/T_1} \right|$$

The zero-crossing point, the TI at which point $S = 0$, is extrapolated from the data and the R_1 of each pixel can be determined via the following relationship:

$$R_1 = \ln 2 / TI_{null}$$

3.2.6. Spontaneous Metastasis Model

Animals were cared for in accordance with the standards of the Canadian Council on Animal Care, and experiments were undertaken with an approved protocol of the University of Western Ontario's Council on Animal Care (AUP 2016-026). Luc-CTL or Luc-1B3 cells (3×10^5) were implanted into the left 4th mammary fat pad of female nod scid gamma mice (Jackson Laboratory, Bar Harbor, Maine, United States). BLI was performed after 150-mg/kg D-luciferin injection. T_1 -weighted 3T-MRI was performed before and 5h post 1-mmol/kg Gd-EOB-DTPA injection. Detectability of widespread metastases was evaluated by imaging Luc-CTL and Luc-1B3 mice (n=3 each) 30 days after cell implantation. Subsequently, a second Luc-1B3 cohort (n=7) was imaged over time until endpoint (up to Day 24) to assess ability to monitor metastasis dynamically.

3.2.7. *In Vivo* Bioluminescence Imaging

Bioluminescence imaging was performed on an IVIS Lumina XRMS *In Vivo* Imaging System (PerkinElmer). Mice were anesthetized with 1-2% isoflurane using a nose cone attached to an activated carbon charcoal filter for passive scavenging, and administered 150 μ L of 30-mg/mL D-luciferin intraperitoneally. Whole-body bioluminescent images were acquired with repeated 1.0-s exposure times every minute for approximately 15 minutes. Once the maximum signal plateaued, the lower half of the mouse *i.e.* location of primary tumour, was shielded with opaque black cloth and the front limbs of the mice were taped down to fully expose the surface area of the thoracic region.

The field-of-view was adjusted to fit the upper body of the mouse and an image was captured with a 5-minute exposure time to detect spontaneous metastases. Regions-of-interest (ROIs) were manually drawn around primary tumour borders using LivingImage software (PerkinElmer, Waltham, Massachusetts, United States) to measure bioluminescent average radiance (p/s/cm²/sr). For analysis of spontaneous metastases, ROIs were automatically generated with LivingImage software (PerkinElmer, Waltham, Massachusetts, United States).

3.2.8. *In Vivo* Magnetic Resonance Imaging

Scans were performed on a 3-T GE clinical MR scanner (General Electric Healthcare Discovery MR750 3.0 T, Milwaukee, Wisconsin, United States) using a custom-built gradient insert and a bespoke 5-cm-diameter solenoidal radiofrequency coil. Mice were anesthetized with 1-2% isoflurane using a nose cone attached to an activated carbon charcoal filter for passive scavenging. T_1 -weighted images were acquired using a 2D Spoiled Gradient Recalled Acquisition in Steady State (SPGR) pulse sequence using the following parameters: FOV = 40mm, TR = 15.8 ms, TE = 10.5 ms, rBW = 31.25 kHz, ETL = 4, Matrix size 400×400, Flip Angle: 60°, NEX = 3, $v = 0.1\text{-}\mu\text{m}^3$ isotropic voxels, scan time = approximately 20 minutes per mouse, dependent on mouse size. Volumes-of-interest (VOIs) were manually delineated around metastatic lesions in post-contrast images using both ITK-SNAP (29) and Horos Project software (horosproject.org, Nimble Co LLC d/b/a Purview, Annapolis, Maryland, United

States). VOIs were manually segmented to acquire measures of signal intensity on both pre-contrast and post-contrast images.

3.2.9. Statistics

Analysis of Variance (ANOVA) and Tukey's post-hoc multiple comparisons were performed for all MRI results. For all tests, a nominal p-value less than 0.05 was considered statistically significant.

3.3 Results

3.3.1 Lentiviral-mediated integration of reporter genes in cancer cells

Lentiviral transfer plasmids encoding pEF1 α -tdTomato/Luciferase, pEF1 α -zsGreen/Oatp1b1, and pEF1 α -zsGreen/Oatp1b3, each separated by self-cleaving 2A peptide sequences, were successfully cloned and utilized to produce lentiviral vectors (**Figure 3.1B, 3.1C**). A human triple-negative breast cancer cell line (MDA-MB-231) was transduced with pEF1 α -tdTomato/Luciferase lentivirus and subsequently sorted for tdTomato fluorescence with >95% purity to obtain luciferase-expressing control cells, hereafter referred to as Luc-CTL cells. Following sorting and expansion, a subset of Luc-CTL cells was transduced a second time with either zsGreen/Oatp1b1 or pEF1 α -zsGreen/Oatp1b3 lentivirus and sorted again for zsGreen fluorescence with >95% purity whilst also matching the tdTomato intensity to that of the sorted Luc-CTL cells. These resulting cell lines are hereafter referred to as Luc-1B1 and Luc-1B3 cells, respectively. *In vitro* bioluminescence imaging demonstrated a significant linear correlation with cell number for both Luc-CTL ($R^2=0.9916$) and Luc-1B3 ($R^2=0.9893$) with slopes that were not considerably different between cell lines (**Figure 3.1D, 3.1E**). Immunoblotting for OATP1B3 protein confirmed absence of *Oatp1b3* expression in both Luc-CTL and Luc-1B1 cells, whereas bands correlating with the molecular weight of glycosylated (100 kDa) and unmodified (77 kDa) OATP1B3 protein (30) were observed in the lane containing lysates from Luc-1B3 cells (**Figure 3.1F**). Non-specific bands across all cell types were observed at about 65 kDa and 72 kDa.

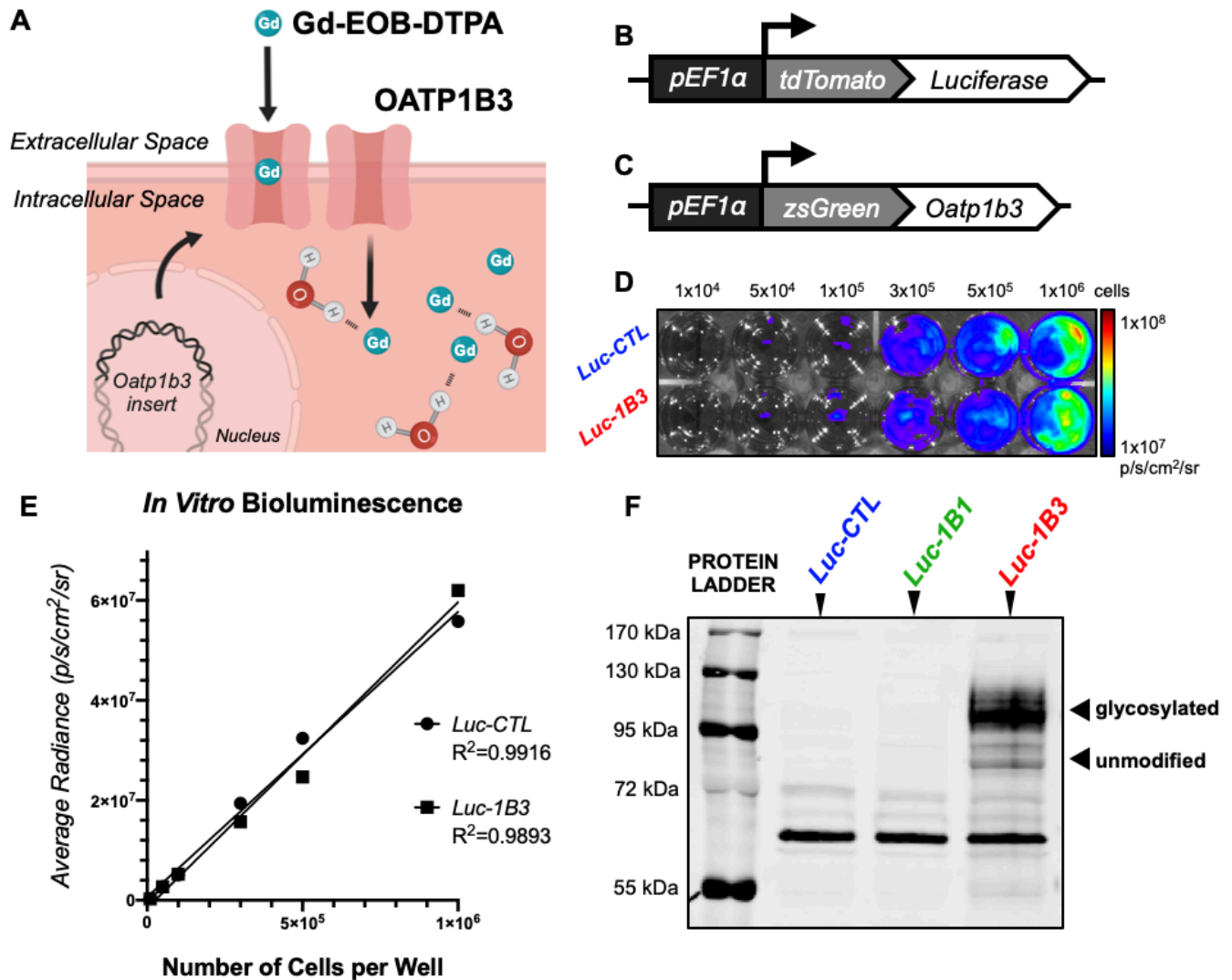


Figure 3.1. Imaging Principle and *In Vitro* Reporter Gene Expression. A, Illustration of the *Oatp1b3* reporter gene mechanism. Cells engineered to express *Oatp1b3* encode a transporter capable of taking up Gd-EOB-DTPA, a paramagnetic agent that interacts with proton spins to increase the spin-lattice relaxation rate of the intracellular environment, which in turn, allows those cells to exhibit increased signal intensity on T_1 -weighted magnetic resonance images. B, Reporter gene cassette constitutively encoding *tdTomato* and *firefly luciferase*. C, Reporter gene cassette constitutively expressing *zsGreen* and *Oatp1b3*. D, Bioluminescence radiance (p/s/cm²/sr) of various

numbers of MDA-MB-231 cells per well expressing *luciferase* (Luc-CTL) or co-expressing *luciferase* and *Oatp1b3* (Luc-1B3). E, Quantification of average radiance (p/s/cm²/sr) of wells containing various numbers of Luc-CTL or Luc-1B3 cells. F, Western blot of cells expressing *luciferase* (Luc-CTL), co-expressing *luciferase* and *Oatp1b1* (Luc-1B1, a closely related transporter), or co-expressing *luciferase* and *Oatp1b3* (Luc-1B3).

3.3.2 Increased spin-lattice relaxation rates of cells expressing *Oatp1b3*

Luc-CTL cells treated with low and high doses of Gd-DTPA did not exhibit significant differences in R_1 rates (0.5827 ± 0.04658 , 0.7464 ± 0.009090 s⁻¹, respectively) to Luc-CTL cells treated with low and high doses of Gd-EOB-DTPA (0.6166 ± 0.05755 , 0.7568 ± 0.03942 s⁻¹, respectively), nor to Luc-1B3 cells treated with low and high doses of Gd-DTPA (0.5821 ± 0.04658 , 0.7494 ± 0.1061 s⁻¹) (**Figure 3.2**). Only Luc-1B3 cells incubated with low and high Gd-EOB-DTPA doses exhibited significantly increased R_1 rates compared to all other conditions (1.320 ± 0.2229 , 3.797 ± 0.1353 s⁻¹) (n=3, p<0.05).

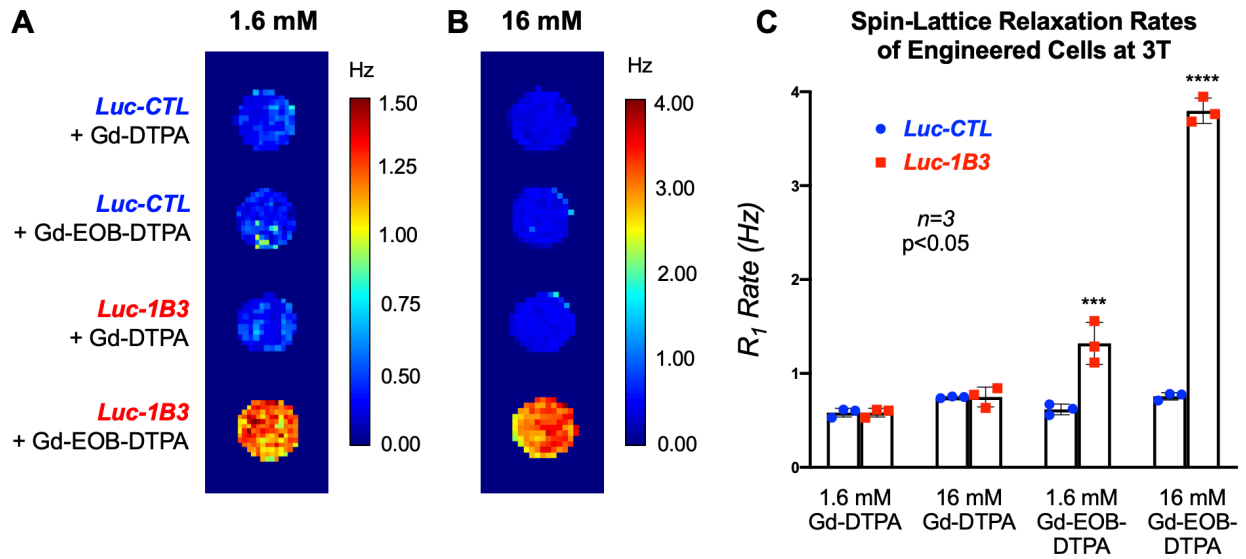


Figure 3.2. Spin-lattice Relaxation Rates of *Oatp1b3*-engineered cells at 3 Tesla. A, Map of spin-lattice relaxation rates (Hz) for MDA-MB-231 cells expressing *luciferase* (*Luc-CTL*) or co-expressing *luciferase* and *Oatp1b3* (*Luc-1B3*) treated with 1.6 mM of either Gd-DTPA (control probe) or Gd-EOB-DTPA. B, Map of spin-lattice relaxation rates (Hz) for MDA-MB-231 cells expressing *luciferase* (*Luc-CTL*) or co-expressing *luciferase* and *Oatp1b3* (*Luc-1B3*) treated with 16 mM of either Gd-DTPA (control probe) or Gd-EOB-DTPA. C) Quantification of spin-lattice relaxation (R_1) rates (Hz) at 3 Tesla of cells treated with either Gd-DTPA or Gd-EOB-DTPA ($n=3$, *** $p<0.001$, **** $p<0.0001$).

3.3.3 Increased contrast enhancement of macro-metastatic lesions, and detection of micro-metastatic lesions with *Oatp1b3*

Macro-metastases ($>1\text{mm}^3$) located at axillary lymph node regions exhibited significantly increased MR signal intensity in Luc-1B3 mice on post-contrast images (4631 ± 968.6 arbitrary units, a.u.) relative to pre-contrast images (766.7 ± 234.7 a.u.), and to Luc-CTL mice both pre- (840.1 ± 122.2 a.u.) and post-contrast (1058 ± 198.0 a.u.) ($n=3$ mice per group, $p<0.0001$) (**Figure 3.3A, 3.3B**). Importantly, numerous micro-metastases ($<1\text{mm}^3$) were detected throughout lungs of Luc-1B3 mice on post-contrast MRI, which were not detected in corresponding pre-contrast MRI, with BLI, nor on post-contrast images of Luc-CTL mice. It was particularly surprising that micro-metastases could be detected in the lungs, because motion artifacts from breathing and susceptibility artifacts from the air-tissue interface were anticipated to present a serious challenge to imaging lung micro-metastases on MRI. Analyzing mean signal intensity and volume of individual foci ($N=60$ across 3 mice) demonstrated that several lesions as small as $\sim 0.01\text{mm}^3$ could be detected on Day 30 post-implantation of the primary tumour (**Figure 3.3C**). The smallest volume that demonstrated mean intensity (3332 a.u.) considerably above the mean intensity of lungs in control animals (236.08 ± 172.9 a.u.), was measured at 0.0043mm^3 , but a more reproducible minimal volume of detection was highlighted by a cluster of lesions ($N=7$) around 0.01mm^3 .

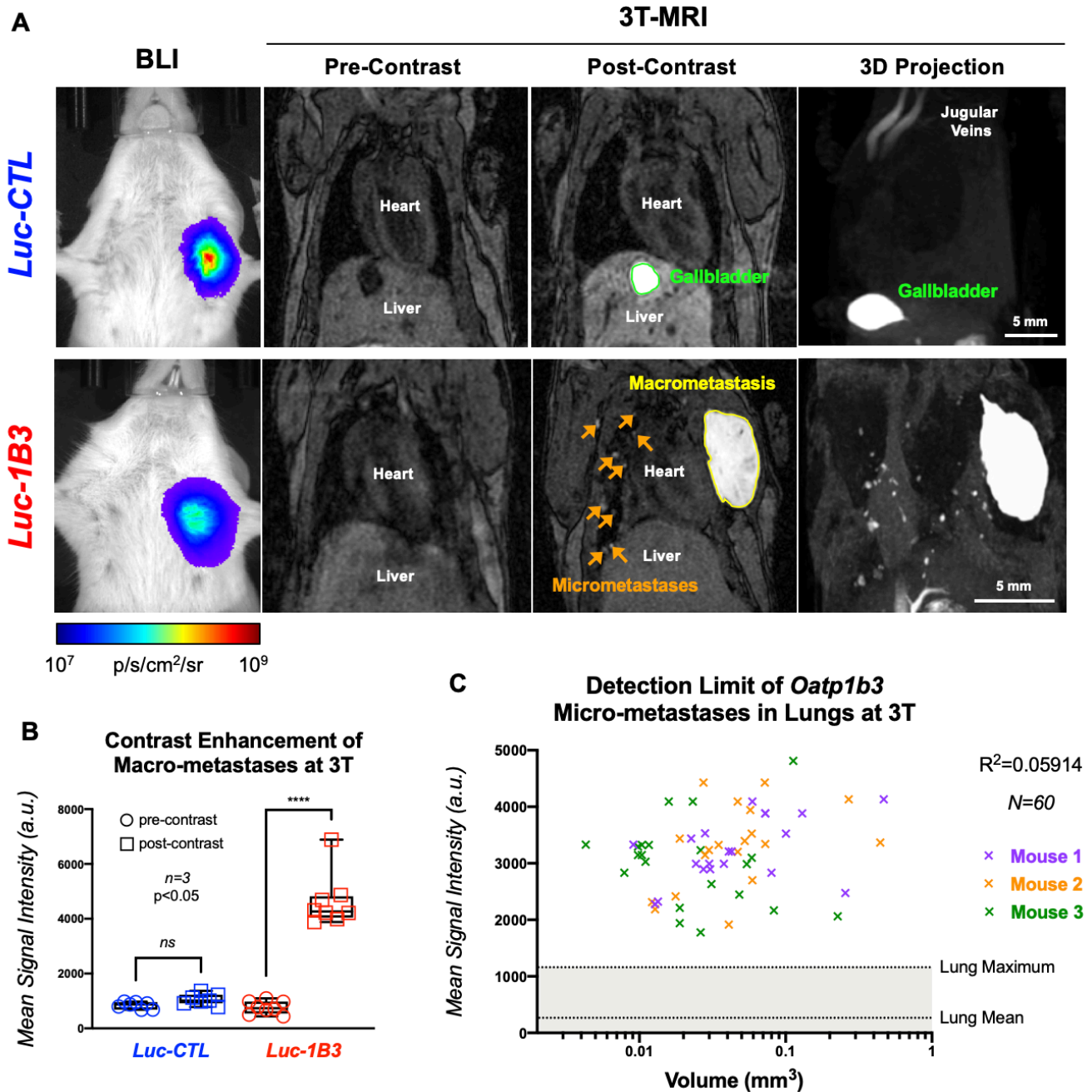


Figure 3.3. Bioluminescence Imaging and Magnetic Resonance Imaging at 3 Tesla of Spontaneous Metastases. A, Bioluminescence imaging (BLI, p/s/cm²/sr) and magnetic resonance imaging (MRI) of mice burdened with MDA-MB-231 cells engineered to express *luciferase* (Luc-CTL) or co-express *luciferase* and *Oatp1b3* (Luc-1B3). Magnetic resonance imaging was acquired pre- and 5 hours post-administration

of 1-mm/kg Gd-EOB-DTPA. Maximum intensity projections are also shown. B, Mean signal intensity (a.u.) of macro-metastases composed of MDA-MB-231 cells engineered to express *luciferase* (Luc-CTL) or co-express *luciferase* and *Oatp1b3* (Luc-1B3) before and 5 hours after administration of 1-mmol/kg Gd-EOB-DTPA (n=3, p<0.05). C, Mean signal intensity (a.u.) and volume (mm³) of individual micro-metastatic lesions (<1mm³) 5 hours after administration of 1-mm/kg Gd-EOB-DTPA, colored according to mouse identity (n=3, ****p<0.0001).

3.3.4 *Oatp1b3* allows for longitudinal tracking of engineered cells spontaneously metastasizing through the lymph nodes and to the lungs

In the Luc-1B3 cohort imaged across three weeks, metastases were first detected via BLI and MRI at the ipsilateral axillary lymph node on average 11 ± 1.3 days after cell implantation into the left-bearing 4th mammary fat pad, with significantly increased MR signal intensity (2903 ± 616.6 a.u.) relative to surrounding muscle tissue (1123 ± 110.4 a.u.) ($n=7$, $p<0.0001$) (**Figure 3.4A**). Five out of 7 mice displayed significant lymph node MRI enhancement within 24 hours following first detection of BLI signal in that region. The remaining two mice showed MR signal enhancement up to two days before BLI signal detection. Follow-up MRI at subsequent days revealed continued tumor growth at the initial ipsilateral axillary lymph node lesion (**Figure 3.4B**), as well as subsequent metastases at other loci, including the contralateral axillary lymph node (**Figure 3.4C**) and ipsilateral brachial lymph node (**Figure 3.4D**). Finally, lung micro-metastases began to appear on MRI approximately 26 days post-implantation of the primary tumor cells (**Figure 3.4E**). Mice were sacrificed at this point due to ulceration of the primary tumour (out of field-of-view in the images). Note that although the initial metastatic lesion in the ipsilateral axillary lymph node was detectible on BLI, subsequent metastatic lesions that formed afterward could be detected via *Oatp1b3*-MRI but could not be resolved on BLI. This was due to excessive light scatter from the much larger first lesions. Eventually, once the second-stage lesions grew to substantial cell numbers, the lesion could be detected on BLI (**Figure 3.4E**). However, at this point, several third-stage

metastases forming in the lungs of the animals, detectible on *Oatp1b3*-MRI, were far too small relative to the bilateral lymph node lesions surrounding them for detection on BLI (**Figure 3.4E**).

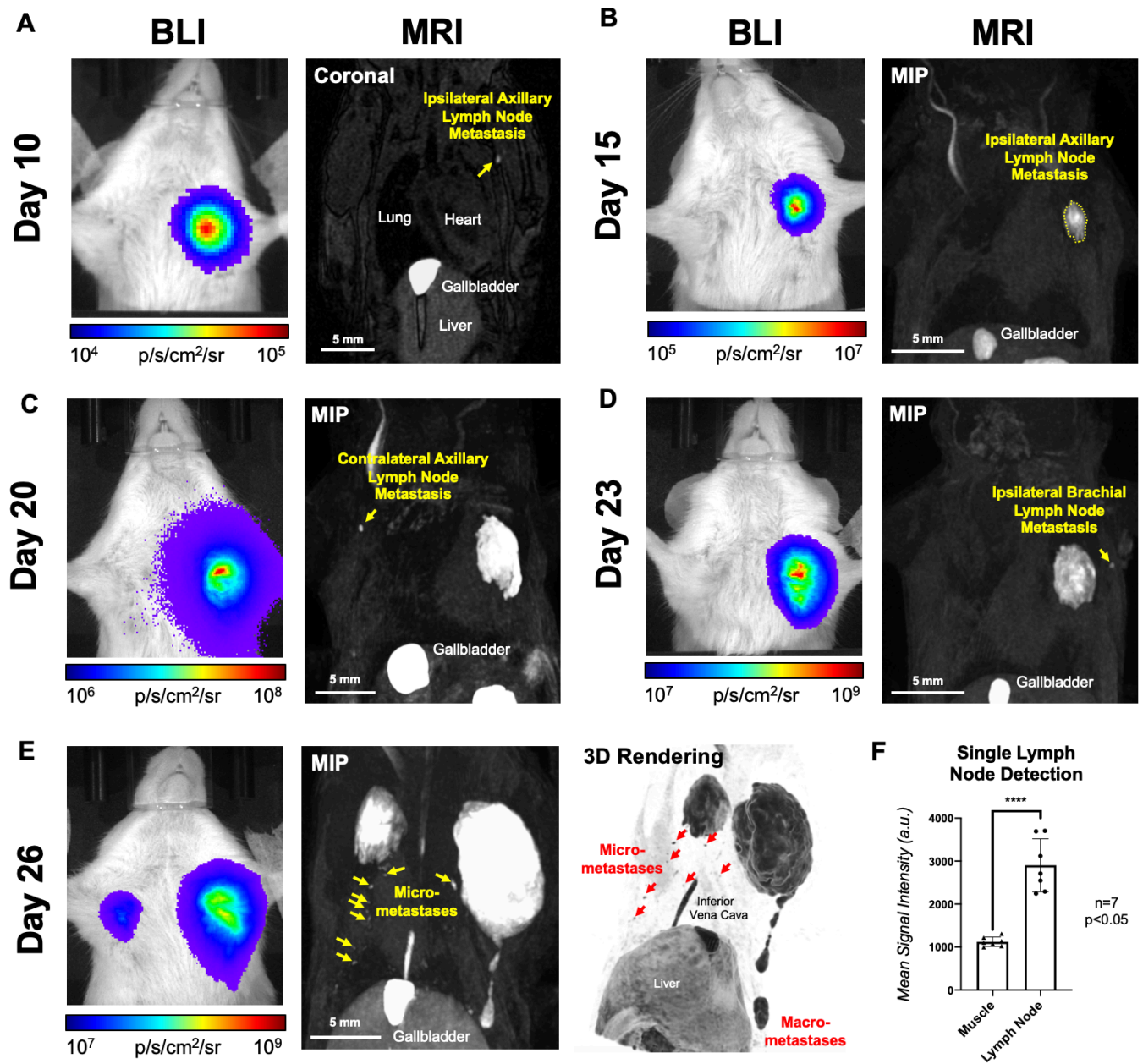


Figure 3.4. Longitudinal Tracking of Spontaneously Metastasizing Cancer Cells via Bioluminescence Imaging and Magnetic Resonance Imaging at 3 Tesla.

Representative bioluminescence images (BLI, p/s/cm²/sr) and magnetic resonance images (MRI) at 3T of female nod scid gamma mice (n=7) after implantation of MDA-MB-231 cells into the left-bearing 4th mammary fat pad on Day 10 (A), Day 15 (B), Day

20 (C), Day 23 (D), and Day 26 (E). MIP, maximal intensity projection. Scale bar, 5 mm.

E, Quantification of mean signal intensity (a.u.) of initial ipsilateral axillary lymph node lesions (Days 10-13) and mean signal intensity (a.u.) of surrounding muscle tissue on MRI (n=7, ****p<0.0001).

3.4 Discussion

Preclinical animal models provide an invaluable platform to improve our understanding of the mechanisms of metastasis and test candidate anti-metastatic therapies under controlled conditions. However, sensitive and quantitative preclinical assessment of metastatic disease with a high degree of accuracy is a significant challenge. Compared with traditional contrast agents, reporter genes offer critical information on cell viability, and do not require the presence of biomarkers to be specific to the cells of interest, as in triple-negative breast cancer. Fluorescence reporter genes generate unparalleled sensitivity and resolution but are largely limited to superficial surfaces and *ex vivo* histological examination. Although the resolution of fluorescent imaging is excellent, assessment of metastases based on histology is labor-intensive and the quality of the output data depends highly on the extent of tissue sampling, *e.g.* measurements across numerous slices composing entire organs *versus* measurements from just a few slices, as well as the reproducibility of the staining approach. To overcome the intensiveness of the process and sampling bias, the last decade has seen a surge of tissue clearing methods that render large biological samples transparent and allow unprecedented three-dimensional views of large volumes of tissue with advanced optical microscopy (31). However, a major drawback of this approach, as with histology, is that only a single timepoint can be acquired of an individual animal, which in turn, would require large numbers of animals to generate effective conclusions for a study (32). This is a particularly serious issue when working with spontaneous metastasis models

that exhibit considerable variability between animals, with respect to both the time and location of metastatic progression (33).

The ability to follow metastatic spread and its response to therapy in a single animal is an important experimental capability. Bioluminescence aims to accomplish this by providing sensitive whole-body information on locations of luciferase-expressing cancer cells, but we demonstrate that smaller cell populations can easily go undetected. Specifically, we show that initiated lymph node lesions and micro-metastases in separate organs are obscured by larger lesions throughout the metastatic process (**Figure 3.3, Figure 3.4**). Assuming that contrast enhanced voxels constituted entirely of Luc-1B3 cells, *i.e.* assuming no partial volume effects, and that 1 million cells correlate to a volume of 1-mm³, micro-metastases containing approximately 10⁴ cells could be detected with *Oatp1b3* post-administration of 1 mmol/kg of Gd-EOB-DTPA at 3 Tesla. However, the range of mean signal intensities exhibited amongst individual micro-metastases (**Figure 3.3C**) suggests that partial volume effects are in play, and that the detection limit of the *Oatp1b3* reporter gene system may fall below this 10,000-cell threshold. Immediate next steps are focused on validating this measurement and accounting for partial volume effects.

Bioluminescence measurements are often biased to detection of larger, more established lesions, that may not necessarily progress and respond to treatment in the same way as much smaller, recently-seeded metastases located in entirely different organ micro-environments. It may be that successful treatments for micro-metastases have been wrongly deemed ineffective simply

because much larger lesions dominated the measurements (34, 35). *Oatp1b3* mitigates these limitations of BLI for effective tracking of metastatic spread. We show that this reporter can dynamically track the metastatic process at its earliest stages, including small single lymph node lesions, even prior to BLI detection in some cases. At late stages, we demonstrate its superiority over BLI to track cancer spread to multiple lymph nodes and other organs such as the lungs. At this resolution, as demonstrated by others with endpoint analysis, we demonstrate that the metastatic process in this model starts when cells from the primary tumor travel to the ipsilateral axillary lymph node, subsequently spreads to the ipsilateral brachial lymph node or the contralateral axillary lymph node, and then the cancer cells appear to migrate down into the lungs. Although the sites of metastasis are in close agreement with previously published literature (36), and exhibit a pattern of metastasis similar to that observed in human breast cancer patients (37-39), imaging the dynamic migration of cancer cells in single animals from one location to the next has not previously been demonstrated. *Oatp1b3* fulfills a long-standing gap in our ability to accurately study metastatic disease over time and offers a path towards deep-tissue tracking of any *Oatp1b3*-engineered cell type with combined high resolution, sensitivity, 3D spatial information, and surrounding anatomical context.

3.5 References

1. Lambert AW, Pattabiraman DR, Weinberg RA. Emerging Biological Principles of Metastasis. *Cell* 2017;168(4):670-691. doi: 10.1016/j.cell.2016.11.037
2. Gengenbacher N, Singhal M, Augustin HG. Preclinical mouse solid tumour models: status quo, challenges and perspectives. *Nat Rev Cancer* 2017;17(12):751-765. doi: 10.1038/nrc.2017.92
3. Mezzanotte L, van 't Root M, Karatas H, Goun EA, Lowik C. In Vivo Molecular Bioluminescence Imaging: New Tools and Applications. *Trends Biotechnol* 2017;35(7):640-652. doi: 10.1016/j.tibtech.2017.03.012
4. Vandergaast R, Khongwichit S, Jiang H, DeGrado TR, Peng KW, Smith DR, Russell SJ, Suksanpaisan L. Enhanced noninvasive imaging of oncology models using the NIS reporter gene and bioluminescence imaging. *Cancer Gene Ther* 2020;27(3-4):179-188. doi: 10.1038/s41417-019-0081-2
5. Ravoori MK, Margalit O, Singh S, Kim SH, Wei W, Menter DG, DuBois RN, Kundra V. Magnetic Resonance Imaging and Bioluminescence Imaging for Evaluating Tumor Burden in Orthotopic Colon Cancer. *Sci Rep* 2019;9(1):6100. doi: 10.1038/s41598-019-42230-w
6. Marien E, Hillen A, Vanderhoydonc F, Swinnen JV, Vande Velde G. Longitudinal microcomputed tomography-derived biomarkers for lung metastasis detection in a syngeneic mouse model: added value to bioluminescence imaging. *Lab Invest* 2017;97(1):24-33. doi: 10.1038/labinvest.2016.114

7. Taus LJ, Flores RE, Seyfried TN. Quantification of metastatic load in a syngeneic murine model of metastasis. *Cancer Lett* 2017;405:56-62. doi: 10.1016/j.canlet.2017.07.011
8. Giubellino A, Woldemichael GM, Sourbier C, Lizak MJ, Powers JF, Tischler AS, Pacak K. Characterization of two mouse models of metastatic pheochromocytoma using bioluminescence imaging. *Cancer Lett* 2012;316(1):46-52. doi: 10.1016/j.canlet.2011.10.019
9. Kubota SI, Takahashi K, Nishida J, Morishita Y, Ehata S, Tainaka K, Miyazono K, Ueda HR. Whole-Body Profiling of Cancer Metastasis with Single-Cell Resolution. *Cell Rep* 2017;20(1):236-250. doi: 10.1016/j.celrep.2017.06.010
10. Chitty JL, Filipe EC, Lucas MC, Herrmann D, Cox TR, Timpson P. Recent advances in understanding the complexities of metastasis. *F1000Res* 2018;7. doi: 10.12688/f1000research.15064.2
11. Louie AY, Huber MM, Ahrens ET, Rothbacher U, Moats R, Jacobs RE, Fraser SE, Meade TJ. In vivo visualization of gene expression using magnetic resonance imaging. *Nat Biotechnol* 2000;18(3):321-325. doi: 10.1038/73780
12. Bartelle BB, Szulc KU, Suero-Abreu GA, Rodriguez JJ, Turnbull DH. Divalent metal transporter, DMT1: a novel MRI reporter protein. *Magn Reson Med* 2013;70(3):842-850. doi: 10.1002/mrm.24509
13. Moore A, Josephson L, Bhorade RM, Basilion JP, Weissleder R. Human transferrin receptor gene as a marker gene for MR imaging. *Radiology* 2001;221(1):244-250. doi: 10.1148/radiol.2211001784

14. Cohen B, Dafni H, Meir G, Harmelin A, Neeman M. Ferritin as an endogenous MRI reporter for noninvasive imaging of gene expression in C6 glioma tumors. *Neoplasia* 2005;7(2):109-117. doi: 10.1593/neo.04436
15. Zurkiya O, Chan AW, Hu X. MagA is sufficient for producing magnetic nanoparticles in mammalian cells, making it an MRI reporter. *Magn Reson Med* 2008;59(6):1225-1231. doi: 10.1002/mrm.21606
16. Patrick PS, Rodrigues TB, Kettunen MI, Lyons SK, Neves AA, Brindle KM. Development of Timd2 as a reporter gene for MRI. *Magn Reson Med* 2016;75(4):1697-1707. doi: 10.1002/mrm.25750
17. Mukherjee A, Wu D, Davis HC, Shapiro MG. Non-invasive imaging using reporter genes altering cellular water permeability. *Nat Commun* 2016;7:13891. doi: 10.1038/ncomms13891
18. Gilad AA, McMahon MT, Walczak P, Winnard PT, Jr., Raman V, van Laarhoven HW, Skoglund CM, Bulte JW, van Zijl PC. Artificial reporter gene providing MRI contrast based on proton exchange. *Nat Biotechnol* 2007;25(2):217-219. doi: 10.1038/nbt1277
19. Shapiro MG, Ramirez RM, Sperling LJ, Sun G, Sun J, Pines A, Schaffer DV, Bajaj VS. Genetically encoded reporters for hyperpolarized xenon magnetic resonance imaging. *Nat Chem* 2014;6(7):629-634. doi: 10.1038/nchem.1934
20. Patrick PS, Kettunen MI, Tee SS, Rodrigues TB, Serrao E, Timm KN, McGuire S, Brindle KM. Detection of transgene expression using hyperpolarized ¹³C urea and diffusion-weighted magnetic resonance spectroscopy. *Magn Reson Med* 2015;73(4):1401-1406. doi: 10.1002/mrm.25254

21. Gilad AA, Winnard PT, Jr., van Zijl PC, Bulte JW. Developing MR reporter genes: promises and pitfalls. *NMR Biomed* 2007;20(3):275-290. doi: 10.1002/nbm.1134
22. Patrick PS, Hammersley J, Loizou L, Kettunen MI, Rodrigues TB, Hu DE, Tee SS, Hesketh R, Lyons SK, Soloviev D, Lewis DY, Aime S, Fulton SM, Brindle KM. Dual-modality gene reporter for in vivo imaging. *Proc Natl Acad Sci U S A* 2014;111(1):415-420. doi: 10.1073/pnas.1319000111
23. Nystrom NN, Hamilton AM, Xia W, Liu S, Scholl TJ, Ronald JA. Longitudinal Visualization of Viable Cancer Cell Intratumoral Distribution in Mouse Models Using Oatp1a1-Enhanced Magnetic Resonance Imaging. *Invest Radiol* 2019. doi: 10.1097/RLI.0000000000000542
24. Wu MR, Liu HM, Lu CW, Shen WH, Lin IJ, Liao LW, Huang YY, Shieh MJ, Hsiao JK. Organic anion-transporting polypeptide 1B3 as a dual reporter gene for fluorescence and magnetic resonance imaging. *FASEB J* 2018;32(3):1705-1715. doi: 10.1096/fj.201700767R
25. Nystrom NN, Hamilton AM, Xia W, Liu S, Scholl TJ, Ronald JA. Longitudinal Visualization of Viable Cancer Cell Intratumoral Distribution in Mouse Models Using Oatp1a1-Enhanced Magnetic Resonance Imaging. *Invest Radiol* 2019;54(5):302-311. doi: 10.1097/RLI.0000000000000542
26. Niviv N. Nyström LCMY, Jeffrey J.L. Carson, Timothy J. Scholl, John A. Ronald Development of a Human Photoacoustic Imaging Reporter Gene Using the Clinical Dye Indocyanine Green. *Radiology: Imaging Cancer* 2019;1(2):e190035. doi: <https://doi.org/10.1148/rycan.2019190035>

27. Rydberg JN, Hammond CA, Huston J, 3rd, Jack CR, Jr., Grimm RC, Riederer SJ. T1-weighted MR imaging of the brain using a fast inversion recovery pulse sequence. *J Magn Reson Imaging* 1996;6(2):356-362. doi: 10.1002/jmri.1880060216
28. Bydder GM, Young IR. MR imaging: clinical use of the inversion recovery sequence. *J Comput Assist Tomogr* 1985;9(4):659-675.
29. Yushkevich PA, Yang G, Gerig G. ITK-SNAP: An interactive tool for semi-automatic segmentation of multi-modality biomedical images. *Conf Proc IEEE Eng Med Biol Soc* 2016;2016:3342-3345. doi: 10.1109/EMBC.2016.7591443
30. Schwarz UI, Meyer zu Schwabedissen HE, Tirona RG, Suzuki A, Leake BF, Mokrab Y, Mizuguchi K, Ho RH, Kim RB. Identification of novel functional organic anion-transporting polypeptide 1B3 polymorphisms and assessment of substrate specificity. *Pharmacogenet Genomics* 2011;21(3):103-114. doi: 10.1097/FPC.0b013e328342f5b1
31. Richardson DS, Lichtman JW. Clarifying Tissue Clearing. *Cell* 2015;162(2):246-257. doi: 10.1016/j.cell.2015.06.067
32. Contag CH, Jenkins D, Contag PR, Negrin RS. Use of reporter genes for optical measurements of neoplastic disease in vivo. *Neoplasia* 2000;2(1-2):41-52. doi: 10.1038/sj.neo.7900079
33. Hung KE, Maricevich MA, Richard LG, Chen WY, Richardson MP, Kunin A, Bronson RT, Mahmood U, Kucherlapati R. Development of a mouse model for sporadic and metastatic colon tumors and its use in assessing drug treatment. *Proc Natl Acad Sci U S A* 2010;107(4):1565-1570. doi: 10.1073/pnas.0908682107
34. Tanaka Y, Araki K, Tanaka S, Miyagawa Y, Suzuki H, Kamide D, Tomifuji M, Uno K, Kimura E, Yamashita T, Ueda Y, Shiotani A. Sentinel Lymph Node-Targeted Therapy

by Oncolytic Sendai Virus Suppresses Micrometastasis of Head and Neck Squamous Cell Carcinoma in an Orthotopic Nude Mouse Model. *Mol Cancer Ther*

2019;18(8):1430-1438. doi: 10.1158/1535-7163.MCT-18-1372

35. Iqbal J, Ginsburg O, Giannakeas V, Rochon PA, Semple JL, Narod SA. The impact of nodal micrometastasis on mortality among women with early-stage breast cancer.

Breast Cancer Res Treat 2017;161(1):103-115. doi: 10.1007/s10549-016-4015-5

36. Puchalapalli M, Zeng X, Mu L, Anderson A, Hix Glickman L, Zhang M, Sayyad MR, Mosticone Wangensteen S, Clevenger CV, Koblinski JE. NSG Mice Provide a Better Spontaneous Model of Breast Cancer Metastasis than Athymic (Nude) Mice. *PLoS One*

2016;11(9):e0163521. doi: 10.1371/journal.pone.0163521

37. Montel V, Huang TY, Mose E, Pestonjamas K, Tarin D. Expression profiling of primary tumors and matched lymphatic and lung metastases in a xenogeneic breast cancer model. *Am J Pathol* 2005;166(5):1565-1579. doi: 10.1016/S0002-

9440(10)62372-3

38. Kluger HM, Chelouche Lev D, Kluger Y, McCarthy MM, Kiriakova G, Camp RL, Rimm DL, Price JE. Using a xenograft model of human breast cancer metastasis to find genes associated with clinically aggressive disease. *Cancer Res* 2005;65(13):5578-

5587. doi: 10.1158/0008-5472.CAN-05-0108

39. Harrell JC, Prat A, Parker JS, Fan C, He X, Carey L, Anders C, Ewend M, Perou CM. Genomic analysis identifies unique signatures predictive of brain, lung, and liver relapse. *Breast Cancer Res Treat* 2012;132(2):523-535. doi: 10.1007/s10549-011-

1619-7

CHAPTER 4 Detection of Viable Cancer Lesions on Photoacoustic Imaging

Rationale. We wanted to develop a photoacoustic imaging (PAI) reporter gene that has high translational potential. Previous research has shown that human *Organic Anion-Transporting Polypeptide 1b3* (*Oatp1b3*) promotes the uptake of the near-infrared fluorescent dye indocyanine green (ICG). Our objective in this study was to establish *Oatp1b3* and ICG as a reporter gene–probe pair for *in vivo* PAI. **Methods.** Human breast cancer cells were engineered to express *Oatp1b3*. Control cells (not expressing *Oatp1b3*) or *Oatp1b3*-expressing cells were incubated with or without ICG, placed in a breast-mimicking phantom, and imaged with PAI. Control (n = 6) or *Oatp1b3*-expressing (n = 5) cells were then implanted orthotopically into female mice. Full-spectrum PAI was performed before and 24 hours after ICG administration. One-way analysis of variance was performed, followed by Tukey post-hoc multiple comparisons, to assess statistical significance. **Results.** *Oatp1b3*-expressing cells incubated with ICG exhibited a 2.7-fold increase in contrast-to-noise ratio relative to all other controls *in vitro* ($p < 0.05$). In mice, PAI signals after ICG administration were increased 2.3-fold in *Oatp1b3* tumours relative to those in controls ($p < 0.05$). **Conclusions.** *Oatp1b3* operates as an *in vivo* PAI reporter gene based on its ability to promote the cellular uptake of ICG. Benefits include the human derivation of *Oatp1b3*, combined with the use of wavelengths in the near-infrared region, high extinction coefficient, low quantum yield, and clinical approval of ICG. We posit that this system will be useful for localized monitoring of emerging gene- and cell-based therapies in clinical applications.

4.1 Introduction

Imaging reporter genes encode for proteins that can be used to visualize cellular and molecular processes in living systems (1). Unlike traditional contrast agents, reporter genes provide unique information on cellular viability as only living cells would express the reporter; and further, reporter expression can be linked to a gene of interest for dynamic tracking of its spatial and temporal expression patterns. Reporter genes for various imaging modalities have been developed, contributing extensively to monitoring the fates of various engineered cell types such as cancer, immune and stem cells in preclinical models (2-4). Moreover, clinical studies have applied reporter genes for monitoring of gene- (5) and cell-based (6) therapies in cancer patients via positron emission tomography (PET). While PET produces whole-body images with high sensitivity, it has limitations such as cost, availability, and ionizing radiation concerns for longitudinal studies. Reporter genes for affordable, portable, and safer imaging modalities are sought for continued localized monitoring of gene and cell therapies in humans.

Photoacoustic imaging (PAI), or optoacoustic imaging, detects acoustic waves from optically-excited sources and is considerably more affordable than PET. Based on the photoacoustic effect, endogenous molecules such as deoxy- and oxyhemoglobin are able to absorb light and convert a fraction of that energy into heat. This heat energy leads to a transient thermoelastic expansion, resulting in emission of ultrasonic waves that can be detected by transducers to produce images. PAI thus combines the benefits of optical contrast with the resolution and depth-detection of ultrasound. Clinical PAI systems currently provide significant contrast at depths of several centimeters with resolutions of a few hundred microns

(7, 8), and PAI is increasingly being applied to a growing number of biomedical applications, from sentinel lymph node imaging to vertebrae imaging for spinal surgery guidance (9-11). Reporter genes for PAI would allow for contrast enhancement of cell populations that would not otherwise produce PAI signals, thus potentially extending the utility of PAI for *in vivo* monitoring of gene- or cell-based therapies. PAI reporter genes that operate in the near-infrared (NIR) window are particularly desirable due to minimal endogenous photoacoustic molecules absorbing at these wavelengths (12).

Though several PAI reporter genes have been developed and have shown significant value in preclinical studies, their clinical utility is potentially limited due to their non-human origin and/or undesirable toxicity (12). We sought to develop a PAI reporter gene system that overcomes these issues to increase the potential for clinical translation. As such, a member of the organic anion-transporting polypeptide (Oatp) family of proteins, namely OATP1B3, is endogenously expressed in the human liver and is responsible for hepatocyte uptake of the NIR fluorescent dye indocyanine green (ICG) during liver function tests. Previous work has also shown that OATP1B3 can take up ICG into cells that express it and can be used as a fluorescence reporter gene system (13, 14). Here we extended these previous studies to establish the combined use of OATP1B3 and ICG as a novel PAI human reporter gene.

4.2 Materials and Methods

4.2.1 Cell Culture

Human embryonic kidney cells (HEK 293T), human triple negative breast cancer cells (MDA-MB-231), and murine triple negative breast cancer cells (4T1) were obtained from a commercial supplier (American Type Culture Collection; ATCC, Manassas, Virginia, United States) and cultured in Dulbecco's Modified Eagle Media (DMEM, Wisent Inc., Saint-Jean-Baptiste, Quebec, Canada) supplemented with 10% fetal bovine serum at 37°C and 5% CO₂. Cells were routinely tested negative for mycoplasma using the MycoAlert mycoplasma detection kit (Lonza Group, Basel, Switzerland).

4.2.2 Lentiviral Production and Generation of Stable Cells

Genetic engineering of the reporter gene system involved third-generation packaging and envelope-expression plasmids (pMDLg/pRRE, pRSV-Rev, and pMD2.G, Addgene plasmids: #12251, #12253, and #12259, respectively; gifts from Didier Trono). A lentiviral transfer vector encoding the *tdTomato* (*tdT*) reporter gene for fluorescence, under regulation of the human elongation factor 1 alpha promoter (pEF1α) was obtained (15) along with a second lentiviral transfer plasmid encoding the *zsGreen1* (*zsG*) reporter gene for fluorescence and the *Organic anion transporting polypeptide 1a1* (*Oatp1a1*) reporter gene separated via a P2A self-cleaving peptide, also under regulation of pEF1α (15). The sequence for *Organic anion transporting polypeptide 1b3* (*Oatp1b3*) was acquired from the hOATP1B3/SLCO1B3 VersaClone cDNA Vector (Cat. RDC0870, R&D Systems, Minneapolis, Minnesota, United States). All cloning was performed using In-Fusion

HD Cloning (Takara Bio USA Inc, Madison, Wisconsin, United States). The *Oatp1a1* sequence in the second lentiviral transfer plasmid was replaced by the *Oatp1b3* sequence to obtain a resultant zsG/*Oatp1b3* lentiviral transfer plasmid. The zsG fluorescent protein was utilized for fluorescence-activated cell sorting of *Oatp1b3*-expressing cells, as it absorbs virtually no near-infrared light within the 680 to 970 nm wavelength range and thus, will not confound signals generated during analysis of *Oatp1b3* as a reporter gene for NIR-PAI (16).

To produce tdT and zsG/*Oatp1b3* lentiviruses (LV-tdT and LV-zsG/*Oatp1b3*), packaging, envelope and the relevant transfer plasmid were co-transfected into human embryonic kidney (HEK 293T) cells using Lipofectamine 3000 according to the manufacturer's lentiviral production protocol (Thermo Fisher Scientific Inc., Waltham, Massachusetts, United States). Lentivirus-containing supernatants were harvested 24h and 48h post transfection, filtered through a 0.45- μ m filter, and stored at -80°C prior to use. Human (MDA-MB-231) and murine (4T1) triple negative breast cancer cells were transduced with lentivirus encoding tdTomato fluorescent protein overnight in the presence of 4- to 8- μ g/mL polybrene. Transduced cells were washed, collected, and sorted using a FACSAria III fluorescence-activated cell sorter (BD Biosciences, Mississauga, Ontario, Canada) for positive tdTomato fluorescence, generating tdTomato Control cells. A subset of these was then transduced with a second lentivirus co-encoding zsGreen fluorescent protein and OATP1B3 and sorted for equivalent tdTomato fluorescence intensity relative to the original tdTomato Control cells, as well as for positive zsGreen fluorescence. The resulting population was named tdTomato OATP1B3 cells.

4.2.3 Immunofluorescence Staining

Cells were grown on glass coverslips, fixed with 4% paraformaldehyde (PFA) for 10 minutes, permeabilized via 0.02% Tween 20 for 20 minutes, and incubated overnight at 4°C with rabbit anti-SLCO1B3 (OATP1B3) primary antibody (2- $\mu\text{g}/\text{mL}$ working concentration, HPA004943, Sigma-Aldrich Canada, Oakville, Ontario, Canada). Goat anti-rabbit AlexaFluor 647-conjugated secondary antibody was then applied (1:500 dilution; 4- $\mu\text{g}/\text{ml}$ working concentration, ab150079, Lot E114795, Abcam, Cambridge, Massachusetts, United States). Cells on coverslips were counterstained with DAPI and imaged using an LSM Meta 510 microscope (Carl Zeiss AG, Oberkochen, Germany).

4.2.4 Proliferation Assays

Non-transduced, tdTomato Control, and tdTomato OATP1B3 cells (5×10^4) were seeded and cell proliferation was evaluated using a tetrazolium salt (3-(4,5-dimethylthiazol-2-yl)-2,5-diphenyltetrazolium bromide, MTT) assay. Cells were incubated in phenol red-free DMEM (Cat. 319-051-CL, Wisent Inc., Saint-Jean-Baptiste, Quebec, Canada) supplemented with 10% FBS that did or did not contain 35- $\mu\text{g}/\text{ml}$ ICG. Prior to optical measurements, wells were washed three times with PBS containing dimethyl sulfoxide (DMSO; 10% v/v). Absorbance measurements at 590 nm were acquired with a spectrophotometer at 0, 24 and 48 hours after seeding. Proliferative measurements at 24 and 48 hours were normalized to absorption values obtained at seeding (0 hours).

4.2.5 *In Vitro* Fluorescence Imaging

Human (MDA-MB-231) and murine (4T1) tdTomato Control and tdTomato OATP1B3 cells were incubated for 90 minutes at 37°C and 5% CO₂ in media containing either 35-µg/ml ICG or an equivalent volume of DMSO solvent. Cells were then washed three times with DMSO-containing PBS (10% v/v), trypsinized, counted and 1x10⁶ cells were pelleted and subsequently transferred into the wells of a custom-built 1% agarose, 0.5% intralipid phantom, designed to be asymmetrical in its distribution of wells. Additionally, a well containing 35-µg/ml ICG, and a well containing media without ICG were included as positive and negative controls, respectively. An IVIS Lumina XRMS *In Vivo* Imaging System (PerkinElmer, Waltham, Massachusetts, United States) was used to measure ICG fluorescence intensity using a 0.5-s exposure time, 780-nm excitation filter, and 845-nm emission filter.

4.2.6 *In Vitro* Photoacoustic Imaging

PAI of the cell phantoms was then performed using a custom-built photoacoustic tomography system. The PAI system consisted of a transducer array with 28 custom-built cylindrical unfocused transducers (2.7-MHz central frequency, ~127% bandwidth, 4.5-mm diameter) mounted on two concentric circular rungs. All transducers were angled inwards to a point 25 mm below the array, providing a field-of-view ~20 mm in diameter. 780-nm NIR illumination was provided by a tunable (680 – 950 nm) 10-Hz-pulsed laser (Phocus InLine, Oportek Inc., California, United States) injected into a four-legged fused-end fiber bundle (Lumen Dynamics Group Inc., Mississauga, Ontario, Canada). The output ends of the fiber bundle were

positioned at the centre of the circular transducer rings, pointing inwards towards the same focal point as the transducers. The transducer array with attached fiber bundles was mounted to an Epson SCARA robot (Epson C4, Suwa, Nagano Prefecture, Japan) for scanning. All transducers were connected to a custom 28-channel, 50-MHz data acquisition system. The phantom was sealed with water in a modified Ziploc bag and submerged in a water tank along with the transducer array. The imaging array was raster scanned in three dimensions with 4-mm steps in the XY-plane, and 5-mm steps in the Z-direction to image the entire phantom. At each scan point, signal averaging was performed over 16 laser pulses to increase the signal-to-noise ratio. Following imaging, image reconstruction using universal back-projection was performed (17). A maximum intensity projection (MIP) image of the 3D stack was then acquired using ImageJ (18). Average signal intensity was measured from each well and the contrast-to-noise ratio (CNR) was calculated relative to an equal-sized ROI positioned at the centre of the MIP image.

4.2.7 *In Vivo* Fluorescence Imaging

All animal experiments were performed in compliance with an approved protocol of the University of Western Ontario's Council on Animal Care (Animal Use Protocol 2016-026) and in accordance with the standards of the Canadian Council on Animal Care. tdTomato Control (n=6) or tdTomato OATP1B3 (n=5) MDA-MB-231 cells (3×10^5) were implanted orthotopically into the right-bearing fourth mammary fat pad of immunocompromised (NU-*Foxn1*^{nu}) 6-8-week-old female mice (Charles River Laboratories, Wilmington, Massachusetts, United States). FLI was performed on an IVIS Lumina XRMS *In Vivo* Imaging System (PerkinElmer,

Waltham, Massachusetts, United States), starting 48h post cellular implantation. Mice were anesthetized with 1-2% isoflurane using a nose cone attached to an activated carbon charcoal filter for passive scavenging. FLI for tdTomato was performed using 520-nm excitation and 570-nm emission filters and images were acquired with a 5-minute exposure time. FLI for ICG was performed using 780-nm excitation and 845-nm emission filters and images were acquired with a 5-min exposure time.

4.2.8 *In Vivo* Photoacoustic Imaging

Mice were anesthetized as described above, and US and PAI were performed using the Vevo LAZR-X System (Fujifilm VisualSonics Inc., Toronto, Ontario, Canada). An LZ550 transducer was used to acquire US and PAI images with axial resolutions of 40 μm . Acoustic signals at each wavelength were measured ten times for signal averaging. The total acquisition time per wavelength was 2.0 s, and a total time of approximately 1.93 minutes was required to image each slice across all wavelengths. US images of tumours were first acquired, followed by NIR spectrum (680-970 nm) PAI in 5-nm increments. For each tumour, a central slice, along with adjacent slices 800 μm on either side were acquired. Regions-of-interest (ROIs) around the perimeter of each tumour in US images were outlined and subsequently overlaid onto corresponding photoacoustic images. Tumour ROIs were processed through the software to generate a full-spectrum photoacoustic plot for each tumour both before and 24 hours following administration of ICG. Vevo Lab Image Software (Fujifilm VisualSonics Inc., Toronto, Ontario, Canada) was used to

spectrally unmix ICG signals from tumour data to generate ICG localization images within tumours, as previously described (19).

4.2.9 *Ex Vivo* FLI and Histology

Following *in vivo* imaging, mice were immediately sacrificed via isofluorane overdose, perfused with 4% paraformaldehyde through the left heart ventricle and tumours were excised from mammary fat pads. Tumours were subsequently frozen in Tissue-Tek Optimum Cutting Temperature (OCT) medium (Sakura Finetek, Maumee, Ohio, United States) and both 150- μ m and 10- μ m frozen sections were collected via the Leica CM350 Cryostat (Leica Microsystems, Wetzlar, Germany). The 150- μ m sections were plated on glass slides and FLI images were collected using the IVIS Lumina XRMS *In Vivo* Imaging System (PerkinElmer, Waltham, Massachusetts, United States) for tdTomato expression (5-s exposure, 520-nm excitation filter, 570-nm emission filter), zsGreen expression (10-s exposure, 480-nm excitation filter, 520-nm emission filter), and ICG uptake/retention (10-s exposure, 780-nm excitation filter, 845-nm emission filter). Microscopy images for tdTomato and zsGreen fluorescence were taken of the 10- μ m sections using an EVOS FL Auto 2 Imaging System (Invitrogen, Thermo Fisher Scientific Inc., Waltham, Massachusetts, United States).

4.2.10 Statistics

One-way Analysis of Variance (ANOVA) was performed followed by Tukey's post-hoc multiple comparisons using Graphpad Prism software (Version 7.00 for Mac OS X, GraphPad Software Inc., La Jolla, California, United States,

www.graphpad.com). For time-course experiments, repeated measures ANOVA was performed, followed by Tukey's post-hoc multiple comparisons. For all tests, a nominal p-value less than 0.05 was considered statistically significant.

4.3 Results

4.3.1 Generation of breast cancer cells expressing reporter genes

Human (MDA-MB-231) and murine (4T1) cells were transduced first with lentivirus encoding the fluorescence reporter *tdTomato* and were subsequently sorted for tdTomato fluorescence with >95% purity to generate tdTomato Control cells. A subset of these was then transduced with a second lentivirus co-encoding the fluorescence reporter *zsGreen1* (zsG) and *Oatp1b3* (**Figure 4.1A**). This second cell population was sorted for both tdTomato intensity equivalent to the tdTomato Control cell population, as well as zsGreen intensity with >95% purity to generate tdTomato OATP1B3 cells (**Figure 4.1B**). Immunofluorescence staining validated absence of *Oatp1b3* expression in tdTomato Control cells, whereas positive staining was present in the tdTomato OATP1B3 cells (**Figure 4.1C**). Proliferation assays showed no significant difference in growth rates between non-transduced cells, tdTomato Control cells, and tdTomato OATP1B3 cells, or between cell populations incubated in 35- μ g/ml ICG for 60 minutes (**Figure 4.1D**).

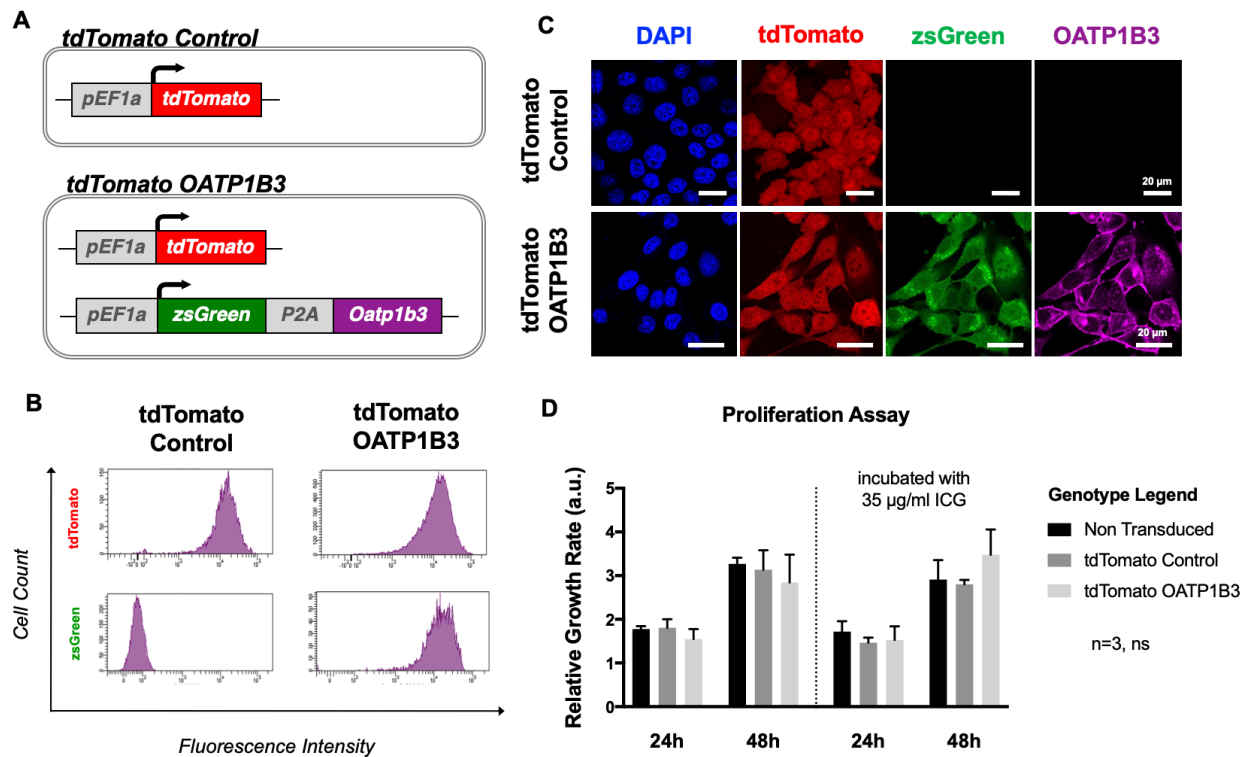


Figure 4.1. Cell Engineering and Characterization. A) Reporter gene constructs used to engineer cells, which include the fluorescence reporter *tdTomato* (top; tdTomato Control), or *tdTomato* in addition to the fluorescence reporter *zsGreen* (zsG) with *Organic anion-transporting polypeptide 1b3* (*Oatp1b3*) separated by the self-cleaving peptide (P2A) (bottom; tdTomato OATP1B3), each under control of the human elongation factor 1 promoter (*pEF1a*). B) Fluorescence-activated cell sorting plots following lentivirus transduction of MDA-MB-231 cells with *tdTomato* Control transfer plasmids or *tdTomato* OATP1B3 transfer plasmids. C) Microscopy of engineered MDA-MB-231 cells for nuclear staining (DAPI; blue), *tdTomato* fluorescence (red), *zsGreen* fluorescence (green), and immunofluorescence staining for OATP1B3 expression (purple). Scale bar, 20 µm. D) Relative growth rates (arbitrary units, a.u.) of Non Transduced, *tdTomato* Control, and *tdTomato* OATP1B3 cells grown in the presence or absence of 35 µg/ml indocyanine green (ICG). Error bars represent one standard deviation.

4.3.2 *In vitro* ICG-enhanced FLI and PAI of breast cancer cells expressing *Oatp1b3*

Next, we evaluated FLI and PAI contrast of both human and murine cells expressing *Oatp1b3* incubated with or without ICG. Both MDA-MB-231 and 4T1 tdTomato OATP1B3 cells incubated with 35- $\mu\text{g/ml}$ ICG, and subsequently washed, exhibited significantly increased fluorescence radiance ($\text{p/s/cm}^2/\text{sr}$) at ICG wavelengths relative to ICG-incubated tdTomato Control cells (4.0-fold, $p < 0.05$; **Figure 4.2A**). Fluorescence radiance from ICG-incubated tdTomato OATP1B3 cells was also significantly increased relative to an equivalent volume of 35- $\mu\text{g/ml}$ ICG alone as the positive control (2.6-fold; $p < 0.05$). No significant difference in fluorescence radiance at ICG wavelengths was observed between tdTomato Control and tdTomato OATP1B3 cells not incubated with ICG, ruling out any contribution of zsGreen to signals at NIR wavelengths. PAI of the same phantom at 780 nm was acquired using a custom-built PAI system. Photoacoustic CNR (arbitrary units, a.u.) was significantly increased for both MDA-MB-231 (2.7-fold; $p < 0.05$) and 4T1 (2.4-fold; $p < 0.05$) tdTomato OATP1B3 cells incubated with 35 $\mu\text{g/ml}$ -ICG, relative to CNR of ICG-incubated tdTomato Control cells and all untreated controls (**Figure 4.2B**). PAI of tdTomato Control cells incubated with ICG did not exhibit a significant difference in CNR relative to untreated Control cells. Additionally, it is important to note that both MDA-MB-231 and 4T1 treated control cells exhibited average fluorescence radiance that was greater than the fluorescence radiance from untreated controls, indicating that there was marginal uptake of ICG by control cells. However, on PAI, these same treated control cells did not demonstrate contrast enhancement greater than untreated controls,

suggesting that the threshold for detection for ICG using PAI is greater than that for ICG using fluorescence imaging.

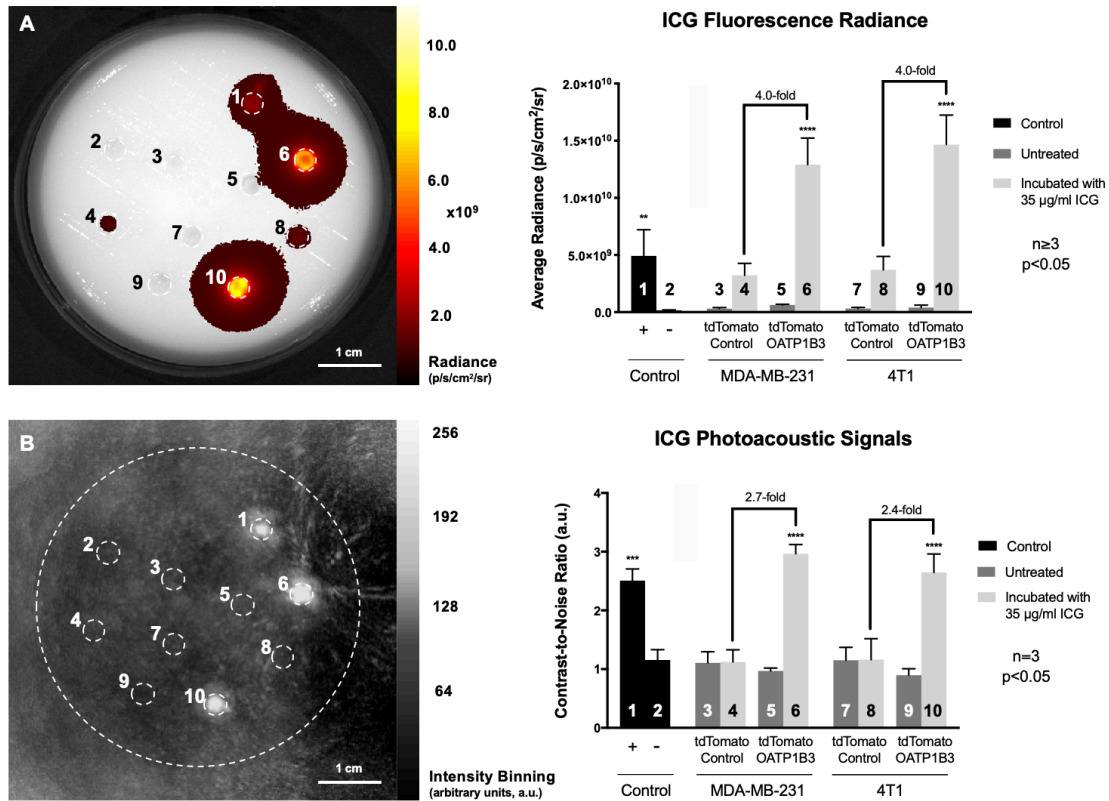


Figure 4.2. In Vitro Fluorescence and Photoacoustic Imaging. A) Fluorescence imaging, acquired with 780-nm excitation and 845-nm emission filters, of an asymmetrical phantom with wells: (1) 35- μ g/ml indocyanine green (ICG); (2) media; (3) MDA-MB-231 tdTomato Control cells; (4) MDA-MB-231 tdTomato Control cells incubated with 35 μ g/ml ICG; (5) MDA-MB-231 tdTomato OATP1B3 cells; (6) MDA-MB-231 tdTomato OATP1B3 cells incubated with 35- μ g/ml ICG; (7) 4T1 tdTomato Control cells; (8) 4T1 tdTomato Control cells incubated with 35- μ g/ml ICG; (9) 4T1 tdTomato OATP1B3 cells; and (10) 4T1 tdTomato OATP1B3 cells incubated with 35- μ g/ml ICG. Fluorescence radiance is measured in p/s/cm²/sr. B) Photoacoustic imaging (PAI) of the same phantom acquired with an optical excitation at 780 nm. Contrast-to-noise ratios (relative to the center of the phantom) were quantified (arbitrary units, a.u.). Numbers, 1-10, on graphs correspond to numbers on images. Scale bar, 1 cm. Error bars represent one standard deviation.

4.3.3 ICG-enhanced FLI signal from *Oatp1b3*-expressing tumours

No significant difference in fluorescence radiance (p/s/cm²/sr) at tdTomato wavelengths was found between tdTomato Control (n=4) and tdTomato OATP1B3 (n=4) tumours over time, suggesting comparable tumour growth rates (**Figure 4.3A**). Longitudinal FLI for ICG fluorescence after intraperitoneal administration of 8-mg/kg ICG determined that the largest significant difference in ICG signals between tdTomato Control and tdTomato OATP1B3 tumours occurred at 24 hours post-ICG (**Figure 4.3B**). Accordingly, a second cohort of animals was imaged prior to ICG administration and 24 hours post-ICG. Neither tdTomato Control (n=6) nor tdTomato OATP1B3 (n=5) tumours generated FLI radiance at ICG wavelengths prior to ICG administration, confirming no possible contribution by zsGreen (**Figure 4.3C, middle column**). Prior to ICG administration, mean fluorescence radiance measures (\pm standard deviation) for ICG were not significantly different between tdTomato Control tumours ($9.14 \pm 3.49 \times 10^6$ p/s/cm²/sr) and tdTomato OATP1B3 tumours ($7.41 \pm 1.86 \times 10^6$ p/s/cm²/sr). In contrast, twenty-four hours after ICG administration, tdTomato OATP1B3 tumours exhibited significantly increased (8.9-fold) fluorescence ($7.36 \pm 1.77 \times 10^8$ p/s/cm²/sr) relative to tdTomato Control tumours ($8.22 \pm 0.527 \times 10^7$ p/s/cm²/sr; $p < 0.05$; **Figure 4.3D**). FLI signals at ICG wavelengths were also detected from the abdomen of both tdTomato Control and tdTomato OATP1B3 tumours 24 hours following ICG administration, likely from physiological hepatobiliary clearance of ICG (20) (**Figure 4.3C, last column**).

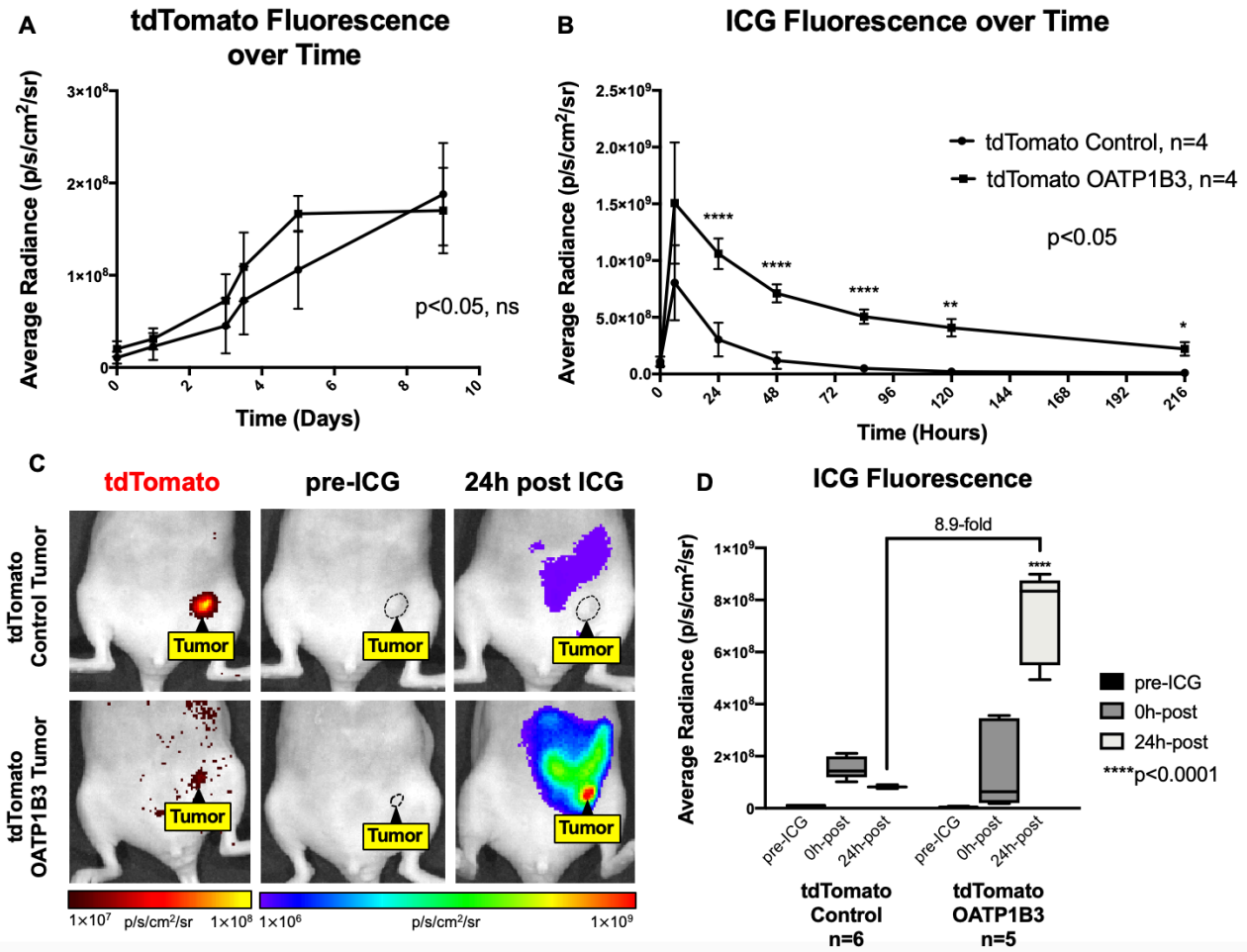


Figure 4.3. *In Vivo* Fluorescence Imaging of Engineered Tumours. A) tdTomato fluorescence radiance (p/s/cm²/sr) of tdTomato Control (n=4) and tdTomato OATP1B3 (n=4) tumours over time. B) ICG fluorescence radiance (p/s/cm²/sr) of tdTomato Control (n=4) and tdTomato OATP1B3 (n=4) tumours over time, up to 9 days, following administration of 8 mg/kg ICG. C) Fluorescence imaging (FLI) for tdTomato (*first column*) and indocyanine green (ICG) average radiance (p/s/cm²/sr) before (pre-ICG; *second column*) and 24 hours following administration of 8-mg/kg ICG (24h post ICG; *third column*) of a representative mouse burdened with a human breast cancer (MDA-MB-231) tdTomato Control tumour (*top panel*) or with a MDA-MB-231 tdTomato OATP1B3 tumour (*bottom panel*). Tumours are outlined with black dashed lines and/or pointed out via the “Tumour”

label. tdTomato signal (*first column*) is directly proportional to tumour size. D) Fluorescence radiance ($\text{p/s/cm}^2/\text{sr}$) of tdTomato Control ($n=6$) and tdTomato OATP1B3 ($n=5$) tumours before administration of indocyanine green (ICG; pre-ICG), immediately following intraperitoneal injection of ICG (0h post ICG), and 24 hours following ICG administration (24h post ICG). Error bars represent one standard deviation. Whiskers on the box graph represent the range of observed values.

4.3.4 ICG-enhanced PAI signal from *Oatp1b3*-expressing tumours

Prior to ICG administration, tdTomato Control and tdTomato OATP1B3 tumour morphology was discernible via US, enabling acquisition of PAI baseline signals at field of views encompassing tumour boundaries (**Figure 4.4A**; i, iii). Since there was variance in tumour size, background signals, and tumour morphology within and across tdTomato Control and tdTomato OATP1B3 tumour groups, mean hemoglobin (HbO₂) PA signals, measured via acoustic average (a.u.) as $\lambda \in (855, 955)$; $\Delta\lambda=5\text{nm}$, was calculated for each acquired spectrum and used to normalize the signal acquired at 805 nm. This ICG-to-HbO₂ signal ratio, referred to as normalized PA signal (a.u.), was not statistically different between tdTomato Control (0.72 ± 0.09 a.u.) and tdTomato OATP1B3 (0.85 ± 0.16 a.u.) tumours prior to ICG injection. Normalized PA signal was also not significantly different between images of tdTomato Control tumours collected before and after ICG administration (0.75 ± 0.13 a.u.; **Figure 4.4C**). In contrast, 24 hours post ICG, tdTomato OATP1B3 tumours demonstrated significantly increased normalized PA signals (1.92 ± 0.40 a.u.) relative to all other groups ($p<0.05$). Importantly, tdTomato OATP1B3 tumours exhibited increased PAI signal within a narrow absorption band spanning from 695 to 855 nm, with a consensus maximum peak at 805 nm across all tdTomato OATP1B3 tumours 24 hours post-ICG.

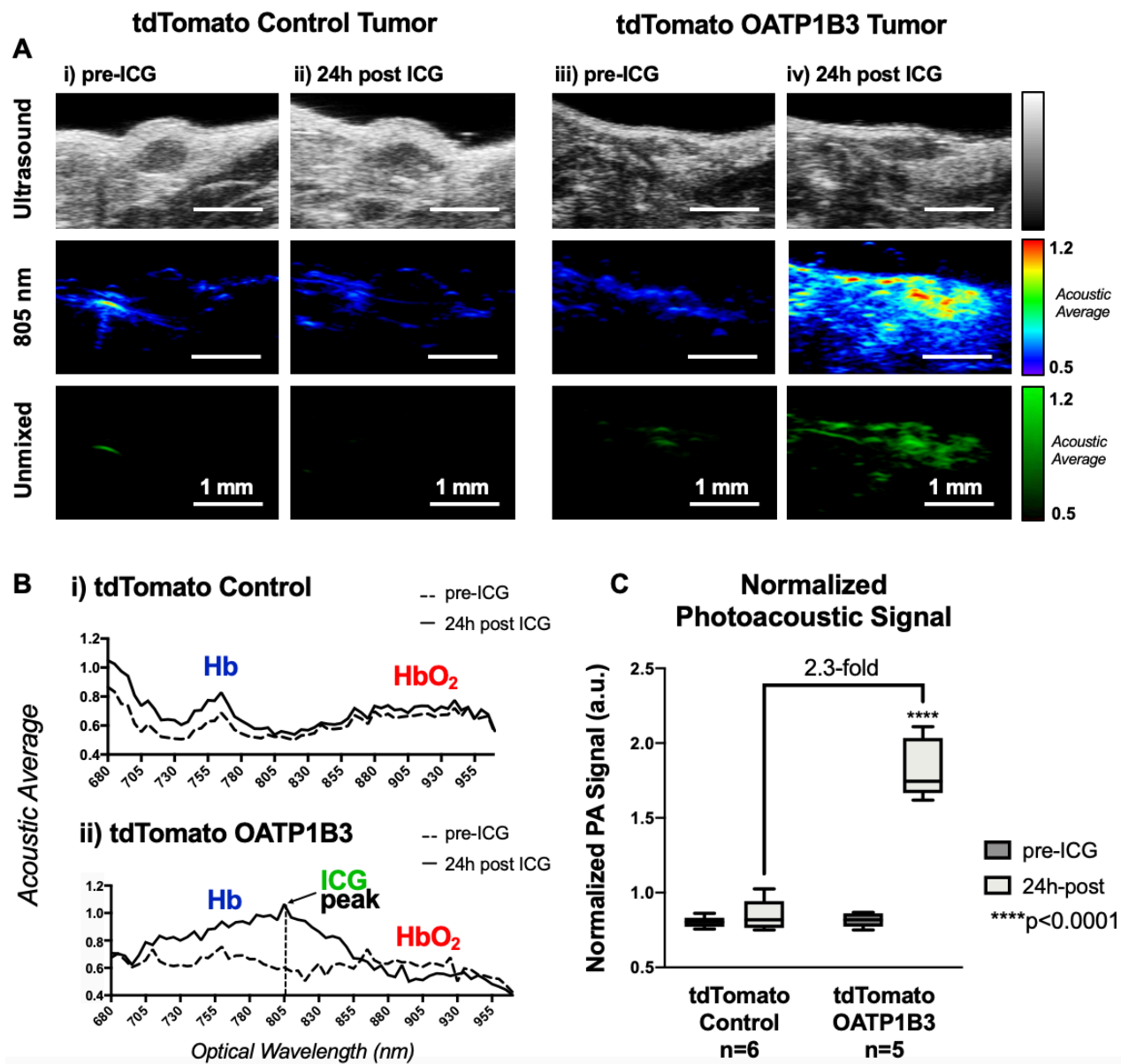


Figure 4.4. *In Vivo* Near-Infrared Spectral Photoacoustic Imaging. A) Ultrasound image (*top row*), PAI image at 805 nm (*second row*), and a spectrally unmixed image of indocyanine green (ICG) distribution across all wavelengths (Unmixed; *third row*) of a representative human breast cancer (MDA-MB-231) tdTomato Control Tumour (*left panel*) and tdTomato OATP1B3 Tumour (*right panel*), both prior-to administration of ICG (i, iii; pre-ICG) and 24 hours following administration of 8-mg/kg ICG (ii, iv; 24h post ICG). PAI contrast enhancement on PAI is exhibited by tdTomato OATP1B3 tumours 24 hours

following ICG administration, while tdTomato Control tumours do not exhibit increased signals 24 hours following ICG administration. B) Near-infrared PAI spectra of a representative tdTomato Control Tumour (*top*) and tdTomato OATP1B3 tumour (*bottom*), before administration of ICG (*dashed-line plot*) and 24 hours following administration of 8-mg/kg ICG (*solid-line plot*), each labelled with hemoglobin (HbO₂; red) and deoxyhemoglobin (Hb; blue) peaks. Increased photoacoustic signals are observed exclusively within tdTomato OATP1B3 tumours 24h post ICG, with a maximum at 805 nm (ICG peak). C) ICG-to-HbO₂ ratio, referred to as the Normalized PA signal (arbitrary units, a.u.), across tumour and treatment groups. Scale bar, 1 mm. Error bars represent one standard deviation. Whiskers on the box graph represent the range of observed values.

4.3.5 *Ex vivo* FLI confirms selective ICG retention in *Oatp1b3*-expressing tumours

zsGreen fluorescence (10-s exposure, 480-nm excitation filter, 520-nm emission filter) was absent in tdTomato Control tumour sections but present in tdTomato OATP1B3 tumour sections. Importantly, ICG FLI signal (10-s exposure, 780-nm excitation filter, 845-nm emission filter) was visible only in tdTomato OATP1B3 tumour sections. Fluorescence microscopy was also conducted, and further validated the presence and/or absence of tdTomato and zsGreen signals from FLI of tumours (**Figure 4.5**).

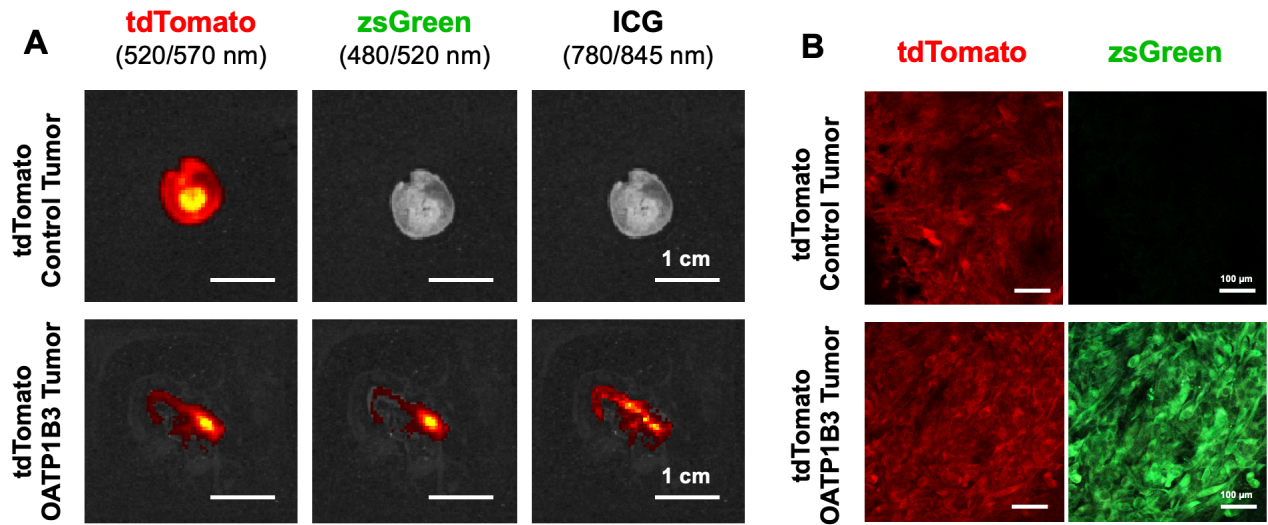


Figure 4.5. Ex Vivo Fluorescence Imaging. A) Fluorescence imaging (FLI) for tdTomato fluorescence (*first column*), zsGreen fluorescence (*second column*), and indocyanine green (ICG; *third column*) of tdTomato Control (*top row*) and tdTomato OATP1B3 (*second row*) tumour slices. Scale bar, 1 cm. B) Fluorescence microscopy for tdTomato (*first column*) and zsGreen (*second column*) of tdTomato Control (*top row*) and tdTomato OATP1B3 (*second row*) tumour slices. Scale bar, 100 μm .

4.4 Discussion

In this study we establish *Oatp1b3* and ICG as a novel reporter gene-probe system for *in vivo* PAI of engineered cell populations. We generated a novel lentiviral vector encoding *Oatp1b3*, allowing for engineering of cell lines to stably express this ICG transporter. Cells engineered to express *Oatp1b3* demonstrated significantly increased fluorescence signals at NIR wavelengths following incubation with ICG, which was not observed in control cells. On PAI, *Oatp1b3*-expressing cells incubated with ICG exhibited significantly increased signals *in vitro*, while ICG-incubated control cells were virtually undetectable. We also demonstrated that *Oatp1b3*-expressing breast cancer cells can be implanted to grow orthotopic tumours *in vivo*, and significantly increased FLI and PAI signal was seen in small tumours (<1mm³) 24 hours following administration of ICG. Importantly, we demonstrate that the increase in PAI detection was specific to the 695 to 855-nm wavelength range, with a consensus maximal peak at 805 nm, allowing for accurate *in vivo* identification of reporter gene-enhanced PAI signal. We further validate selective retention of ICG by *Oatp1b3*-expressing tumours.

Our study extends previous work on *Oatp1b3*, establishing it as a multimodality reporter for numerous clinically-relevant modalities such as FLI, and now PAI, and also introduces potential for *Oatp1b3* reporter gene imaging on a clinical 3-Tesla MR scanner. OATP1B3-enhanced PAI uniquely offers a non-ionizing and cost-effective method to detect engineered cell populations with sensitivity and relatively high resolution. Clinical PAI systems can image up to around 7 centimeters (21), and thus future work should establish how many *Oatp1b3*-expressing cells can be detected at specific depths in larger animal models. A caveat of this system is

that the engineered cells to be imaged on PAI should not be located beyond an optical-scattering material *e.g.*, within the adult human skull, where the light needed to excite ICG would be largely reflected by bone before getting to the engineered cells. However, this issue may be solved through the use of more penetrative PAI systems that are being developed (22, 23). The ability to evaluate the status of a gene or cell population using whole-body (MRI) (24), localized (PAI) and microscopic (fluorescence) imaging techniques with a single reporter gene system could be broadly useful for many biomedical applications, such as tracking the viability and migration of therapeutic cells in patients (25, 26). Rat-derived *Oatp1a1* and the tracer ¹¹¹Indium-EOB-DTPA have also been established as a reporter gene-probe pair for single photon emission computed tomography (SPECT) (27). Studies evaluating human *Oatp1b3* as a SPECT reporter gene are warranted to further extend the potential utility of this human reporter beyond FLI, PAI, and MRI, and improve cellular detectability via the higher probe sensitivity offered by SPECT.

The ideal PAI reporter gene would be specific to the biological process of interest; exhibit an absorption maximum within the NIR window for deep tissue *in vivo* imaging; and, be nontoxic to the cell. Though other reporter genes for PAI have been described (*e.g.*, NIR fluorescent proteins, photo-switchable fluorescent proteins), the PAI reporter gene arguably considered to have the highest translational potential is human *tyrosinase*, which initiates the conversion of endogenous tyrosine into detectable melanin (19, 28-30). Though *tyrosinase* presents desirable properties, including human origin, signal amplification due to enzymatic action, and a detectible product with high photostability, it is not without limitations (7). For instance, the melanin photoacoustic profile displays a broadband,

featureless absorption spectrum, making it difficult to distinguish ectopic melanin from other intrinsic signals with accuracy (12). Our *Oatp1b3*-ICG system, on the other hand, features a distinct band within the NIR region that is easy to identify and un-mix from hemoglobin and deoxyhemoglobin spectra, and from spectra of other PAI reporters added to the biological system for more complex functional imaging. It is also interesting to note that wells in the *in vitro* experiments containing a sample of ICG-incubated *Oatp1b3*-engineered cells exhibited greater fluorescence radiance (2.6-fold) and PAI signals (1.19-fold) relative to the positive-control well containing a sample of ICG at the treatment concentration. This suggests that uptake of ICG by OATP1B3 occurs in an active or active-coupled process, rather than simple diffusion, which is in agreement with current theories describing uptake mechanisms of the OATP1 family of transporters (31). While *tyrosinase* exhibits signal amplification due to enzymatic action, *Oatp1b3* may provide signal amplification through active or active-coupled uptake of many ICG molecules. In addition, altered cell phenotype and toxicity associated with ectopic *tyrosinase* activity has been documented, (28, 32, 33) in so much that *tyrosinase*-encoding plasmid distributors (e.g., Imanis Life Sciences), recommend inducible promoters to minimize undesired biological effects during imaging studies. Though documented experiments are limited in number, ectopic *Oatp1b3* overexpression has not been reported to cause cellular toxicity or confer observable phenotypic changes (14, 34), and we did not observe any quantitative or qualitative differences in cell proliferation rates and/or morphology in our own work, even when engineered cells were incubated in the presence of ICG. As we performed here, it was important to assess the effectiveness of this system at the preclinical stage using doses of ICG equivalent to current

clinical guidelines. Though ICG is safe to inject at these doses, further safety evaluation may be warranted on the intracellular toxicity of ICG once it is internalized by the OATP1B3 transporter. It should also be noted that detection of engineered cells near the hepatobiliary system would be difficult, as clearance of ICG within that pathway obscure the ability to detect OATP1B3-engineered cells retaining ICG.

In the clinic, PET reporter genes have so far been used in patients for imaging of adenoviral gene therapy (5) and cytotoxic T cell immunotherapies (6) in cancer patients. These studies mark major milestones in reporter gene imaging, but limited access and costs due to associated infrastructure and operation, in combination with concerns over ionizing radiation may hinder broad applicability and longitudinal imaging via PET reporter genes. These limitations highlight the need for alternative reporter gene systems for safe, cost-effective, and accessible imaging modalities within the clinic. Although nuclear imaging (PET/SPECT) is capable of whole-body visualization, and photoacoustics is limited to localized imaging, reporter gene imaging with PAI should be applicable for a variety of clinical problems that only require imaging of specific tissues (35). For example, including the *Oatp1b3* reporter gene to the genetic engineering protocol of chimeric antigen receptor (CAR) T cell therapies targeting prostate cancer stem cells (36) would allow for longitudinal monitoring of these cells in the prostate via an intraperitoneal laser/transrectal transducer system (37). We expect this technology to be particularly useful in clinical trials that involve localized injection of a gene or cellular therapy into a specific tissue, as it allows for real-time information on how a particular therapy is operating in the patient. Questions of interest include: is the therapy getting to the target site? Is it activating at the target site? For how long does it persist? Does reporter

expression correlate with patient response? However, until more gene and cell-based therapeutics make their way into the clinic, we expect that this multimodality reporter system will be more rapidly utilized for tracking of gene expression and cell populations in preclinical animal models.

4.5 References

1. James ML, Gambhir SS. A molecular imaging primer: modalities, imaging agents, and applications. *Physiol Rev* 2012;92(2):897-965. doi: 10.1152/physrev.00049.2010
2. Dubey P. Reporter gene imaging of immune responses to cancer: progress and challenges. *Theranostics* 2012;2(4):355-362. doi: 10.7150/thno.3903
3. Liu H, Yang H, Zhu D, Sui X, Li J, Liang Z, Xu L, Chen Z, Yao A, Zhang L, Zhang X, Yi X, Liu M, Xu S, Zhang W, Lin H, Xie L, Lou J, Zhang Y, Xi J, Deng H. Systematically labeling developmental stage-specific genes for the study of pancreatic beta-cell differentiation from human embryonic stem cells. *Cell Res* 2014;24(10):1181-1200. doi: 10.1038/cr.2014.118
4. Fesnak AD, June CH, Levine BL. Engineered T cells: the promise and challenges of cancer immunotherapy. *Nat Rev Cancer* 2016;16(9):566-581. doi: 10.1038/nrc.2016.97
5. Jacobs A, Voges J, Reszka R, Lercher M, Gossmann A, Kracht L, Kaestle C, Wagner R, Wienhard K, Heiss WD. Positron-emission tomography of vector-mediated gene expression in gene therapy for gliomas. *Lancet* 2001;358(9283):727-729.
6. Keu KV, Witney TH, Yaghoubi S, Rosenberg J, Kurien A, Magnusson R, Williams J, Habte F, Wagner JR, Forman S, Brown C, Allen-Auerbach M, Czernin J, Tang W, Jensen MC, Badie B, Gambhir SS. Reporter gene imaging of targeted T cell immunotherapy in recurrent glioma. *Sci Transl Med* 2017;9(373). doi: 10.1126/scitranslmed.aag2196
7. Weber J, Beard PC, Bohndiek SE. Contrast agents for molecular photoacoustic imaging. *Nat Methods* 2016;13(8):639-650. doi: 10.1038/nmeth.3929
8. Choi W, Park EY, Jeon S, Kim C. Clinical photoacoustic imaging platforms. *Biomed Eng Lett* 2018;8(2):139-155. doi: 10.1007/s13534-018-0062-7

9. Stoffels I, Morscher S, Helfrich I, Hillen U, Leyh J, Burton NC, Sardella TC, Claussen J, Poeppel TD, Bachmann HS, Roesch A, Griewank K, Schadendorf D, Gunzer M, Klode J. Metastatic status of sentinel lymph nodes in melanoma determined noninvasively with multispectral optoacoustic imaging. *Sci Transl Med* 2015;7(317):317ra199. doi: 10.1126/scitranslmed.aad1278
10. Shubert J, Lediju Bell MA. Photoacoustic imaging of a human vertebra: implications for guiding spinal fusion surgeries. *Phys Med Biol* 2018;63(14):144001. doi: 10.1088/1361-6560/aacdd3
11. Jose J, Grootendorst DJ, Vijn TW, Wouters MW, van Boven H, van Leeuwen TG, Steenbergen W, Ruers TJ, Manohar S. Initial results of imaging melanoma metastasis in resected human lymph nodes using photoacoustic computed tomography. *J Biomed Opt* 2011;16(9):096021. doi: 10.1117/1.3631705
12. Brunker J, Yao J, Laufer J, Bohndiek SE. Photoacoustic imaging using genetically encoded reporters: a review. *J Biomed Opt* 2017;22(7). doi: 10.1117/1.JBO.22.7.070901
13. Wu MR, Liu HM, Lu CW, Shen WH, Lin IJ, Liao LW, Huang YY, Shieh MJ, Hsiao JK. Organic anion-transporting polypeptide 1B3 as a dual reporter gene for fluorescence and magnetic resonance imaging. *FASEB J* 2018;32(3):1705-1715. doi: 10.1096/fj.201700767R
14. de Graaf W, Hausler S, Heger M, van Ginhoven TM, van Cappellen G, Bennink RJ, Kullak-Ublick GA, Hesselmann R, van Gulik TM, Stieger B. Transporters involved in the hepatic uptake of (99m)Tc-mebrofenin and indocyanine green. *J Hepatol* 2011;54(4):738-745. doi: 10.1016/j.jhep.2010.07.047
15. Nystrom NN, Hamilton AM, Xia W, Liu S, Scholl TJ, Ronald JA. Longitudinal Visualization of Viable Cancer Cell Intratumoural Distribution in Mouse Models Using

Oatp1a1-Enhanced Magnetic Resonance Imaging. *Invest Radiol* 2019. doi:

10.1097/RLI.0000000000000542

16. Comenge J, Fragueiro O, Sharkey J, Taylor A, Held M, Burton NC, Park BK, Wilm B, Murray P, Brust M, Levy R. Preventing Plasmon Coupling between Gold Nanorods Improves the Sensitivity of Photoacoustic Detection of Labeled Stem Cells in Vivo. *ACS Nano* 2016;10(7):7106-7116. doi: 10.1021/acsnano.6b03246

17. Xu M, Wang LV. Universal back-projection algorithm for photoacoustic computed tomography. *Phys Rev E Stat Nonlin Soft Matter Phys* 2005;71(1 Pt 2):016706. doi: 10.1103/PhysRevE.71.016706

18. Schneider CA, Rasband WS, Eliceiri KW. NIH Image to ImageJ: 25 years of image analysis. *Nat Methods* 2012;9(7):671-675.

19. Paproski RJ, Heinmiller A, Wachowicz K, Zemp RJ. Multi-wavelength photoacoustic imaging of inducible tyrosinase reporter gene expression in xenograft tumours. *Sci Rep* 2014;4:5329. doi: 10.1038/srep05329

20. Cusin F, Fernandes Azevedo L, Bonnaventure P, Desmeules J, Daali Y, Pastor CM. Hepatocyte Concentrations of Indocyanine Green Reflect Transfer Rates Across Membrane Transporters. *Basic Clin Pharmacol Toxicol* 2017;120(2):171-178. doi: 10.1111/bcpt.12671

21. Valluru KS, Willmann JK. Clinical photoacoustic imaging of cancer. *Ultrasonography* 2016;35(4):267-280. doi: 10.14366/usg.16035

22. Nie L, Cai X, Maslov K, Garcia-Uribe A, Anastasio MA, Wang LV. Photoacoustic tomography through a whole adult human skull with a photon recycler. *J Biomed Opt* 2012;17(11):110506. doi: 10.1117/1.JBO.17.11.110506

23. Nasiriavanaki M, Xia J, Wan H, Bauer AQ, Culver JP, Wang LV. High-resolution photoacoustic tomography of resting-state functional connectivity in the mouse brain. *Proc Natl Acad Sci U S A* 2014;111(1):21-26. doi: 10.1073/pnas.1311868111
24. Nystrom NN, Hamilton AM, Xia W, Liu S, Scholl TJ, Ronald JA. Longitudinal Visualization of Viable Cancer Cell Intratumoural Distribution in Mouse Models Using Oatp1a1-Enhanced Magnetic Resonance Imaging. *Invest Radiol* 2019;54(5):302-311. doi: 10.1097/RLI.0000000000000542
25. Li M, Wang Y, Liu M, Lan X. Multimodality reporter gene imaging: Construction strategies and application. *Theranostics* 2018;8(11):2954-2973. doi: 10.7150/thno.24108
26. Kircher MF, de la Zerda A, Jokerst JV, Zavaleta CL, Kempen PJ, Mittra E, Pitter K, Huang R, Campos C, Habte F, Sinclair R, Brennan CW, Mellinghoff IK, Holland EC, Gambhir SS. A brain tumour molecular imaging strategy using a new triple-modality MRI-photoacoustic-Raman nanoparticle. *Nat Med* 2012;18(5):829-834. doi: 10.1038/nm.2721
27. Patrick PS, Hammersley J, Loizou L, Kettunen MI, Rodrigues TB, Hu DE, Tee SS, Hesketh R, Lyons SK, Soloviev D, Lewis DY, Aime S, Fulton SM, Brindle KM. Dual-modality gene reporter for in vivo imaging. *Proc Natl Acad Sci U S A* 2014;111(1):415-420. doi: 10.1073/pnas.1319000111
28. Thangasamy T, Sittadjody S, Limesand KH, Burd R. Tyrosinase overexpression promotes ATM-dependent p53 phosphorylation by quercetin and sensitizes melanoma cells to dacarbazine. *Cell Oncol* 2008;30(5):371-387.
29. Krumholz A, Vanvickle-Chavez SJ, Yao J, Fleming TP, Gillanders WE, Wang LV. Photoacoustic microscopy of tyrosinase reporter gene in vivo. *J Biomed Opt* 2011;16(8):080503. doi: 10.1117/1.3606568

30. Zheng H, Zhou L, Shi Y, Tian J, Wang F. Tyrosinase-Based Reporter Gene for Photoacoustic Imaging of MicroRNA-9 Regulated by DNA Methylation in Living Subjects. *Mol Ther Nucleic Acids* 2018;11:34-40. doi: 10.1016/j.omtn.2018.01.008
31. Stieger B, Hagenbuch B. Organic anion-transporting polypeptides. *Curr Top Membr* 2014;73:205-232. doi: 10.1016/B978-0-12-800223-0.00005-0
32. Greggio E, Bergantino E, Carter D, Ahmad R, Costin GE, Hearing VJ, Clarimon J, Singleton A, Eerola J, Hellstrom O, Tienari PJ, Miller DW, Beilina A, Bubacco L, Cookson MR. Tyrosinase exacerbates dopamine toxicity but is not genetically associated with Parkinson's disease. *J Neurochem* 2005;93(1):246-256. doi: 10.1111/j.1471-4159.2005.03019.x
33. Hasegawa T. Tyrosinase-expressing neuronal cell line as in vitro model of Parkinson's disease. *Int J Mol Sci* 2010;11(3):1082-1089. doi: 10.3390/ijms11031082
34. Monks NR, Liu S, Xu Y, Yu H, Bendelow AS, Moscow JA. Potent cytotoxicity of the phosphatase inhibitor microcystin LR and microcystin analogues in OATP1B1- and OATP1B3-expressing HeLa cells. *Mol Cancer Ther* 2007;6(2):587-598. doi: 10.1158/1535-7163.MCT-06-0500
35. Steinberg I, Huland DM, Vermesh O, Frostig HE, Tummers WS, Gambhir SS. Photoacoustic clinical imaging. *Photoacoustics* 2019;14:77-98. doi: 10.1016/j.pacs.2019.05.001
36. Deng Z, Wu Y, Ma W, Zhang S, Zhang YQ. Adoptive T-cell therapy of prostate cancer targeting the cancer stem cell antigen EpCAM. *BMC Immunol* 2015;16:1. doi: 10.1186/s12865-014-0064-x

37. Lediju Bell MA, Kuo NP, Song DY, Kang JU, Boctor EM. In vivo visualization of prostate brachytherapy seeds with photoacoustic imaging. *J Biomed Opt* 2014;19(12):126011. doi: 10.1117/1.JBO.19.12.126011

CHAPTER 5 Summary and Future Work

This thesis presents work on *Organic Anion-Transporting Polypeptide 1 (Oatp1)* as a reporter gene for multimodality cell tracking in preclinical animal models with high sensitivity, high resolution, and surrounding anatomical context. At the start of this research, a single publication existed describing rat *Oatp1a1* as a magnetic resonance reporter gene, using optimal parameters to prove its principle: high field strengths (7T, 9.4T), large doses of Gd-EOB-DTPA, and xenografts in animal models. At that point in time, *Oatp1* demonstrated great potential as a reporter gene, and provided a lot of excitement for future utility. In our work, we were first interested in assessing the feasibility of translating this system to the clinic. We showed that *Oatp1a1* can be used to track cells at 3 Tesla, with clinically-feasible doses of the paired imaging probe Gd-EOB-DTPA, and that these parameters allow for imaging high resolution distribution patterns of viable cells in 3-dimensional space. Next, we transitioned to a closely-related human transporter called *Oatp1b3*. We showed that *Oatp1b3* can be used to track small populations of spontaneously metastasizing cancer cells longitudinally via MRI, and estimated its detection limit at about 10^4 cells. Finally, we demonstrated that *Oatp1b3* can be used as a photoacoustic imaging reporter gene, based on its ability to take up indocyanine green *in vivo*, allowing for rapid and cost-effective imaging of engineered cells in tissues. This thesis represents an important step in the development of a versatile imaging tool for tracking the location of viable engineered cells in preclinical animal models and lays groundwork for translating this technology for tracking of genes and/or cells in patients. The following sections outline a summary of the main findings in each study, as well as challenges and limitations, and future research avenues.

5.1 Discussion and Conclusions

5.1.1 Chapter 2 - High Resolution *Oatp1* Imaging using Clinical MR Parameters

First, we tested the feasibility of using *Oatp1a1* to track the growth of primary tumours over time on MRI, at clinical field strengths of 3 Tesla and clinically-feasible doses of 0.1-mmol/kg Gd-EOB-DTPA in mice. Using bioluminescence imaging as a reference modality, we observed continued growth in BLI signals from primary tumours over time at low resolutions. The main findings of this chapter were: 1) *Oatp1a1* enhances bioluminescence imaging signals by mediating increased D-luciferin transport into engineered cells; 2) there is significant *in vivo* contrast enhancement by *Oatp1a1*-engineered cells on MRI at 3 Tesla, and 0.1-mmol/kg Gd-EOB-DTPA; and, 3) high resolution contrast enhancement patterns of engineered cells on MRI strongly correlated to distributions of viable cancer cells on matched histology.

Ultimately, this initial set of observations established the multi-dimensional utility of using *Oatp1a1* for tracking viable cells *in vivo*. Increased uptake of D-luciferin resulted in increased sensitivity on bioluminescence imaging, allowing for detection of smaller and/or deeper populations of engineered cells, that would have otherwise gone undetected. MRI demonstrated that engineered cells appear enhanced at 3 Tesla, with relatively low doses of Gd-EOB-DTPA. Further, with longitudinal monitoring, we were able to dynamically observe architectural changes within primary tumours at high resolutions, including the emergence of necrotic centres and non-cancer cells within primary tumour boundaries, and were able to quantitatively validate these enhancement patterns at endpoint

using matched histology. In summary, this chapter established *Oatp1a1* reporter gene imaging as a powerful tool to track viable engineered cells on MRI, with concomitant BLI enhancement. The multi-ligand nature of *Oatp1a1*, in its ability to take up D-luciferin and enhance BLI signals, as well as Gd-EOB-DTPA to enhance MR signals, warranted investigation towards other hepato-specific substrates, such as indocyanine green (ICG) for the enhancement of fluorescent and photoacoustic signals (1). However, we observed only modest uptake of ICG by *Oatp1a1* in preliminary studies. At this point, we sought to investigate additional *Oatp1* transporters, namely human *Oatp1b1* and *Oatp1b3*, to characterize their uptake preferences for potential use in molecular imaging. *Oatp1b3* proved to be very useful, and the sequential chapters highlight our major findings.

5.1.2 Chapter 3 - Whole-Body Tracking of Spontaneous Metastases on MRI

In the previous chapter, we initially planned to use *Oatp1* as a tool to track bulk groups of cells on MRI and held conservative views on the sensitivity of this reporter gene technology. However, we were surprised to observe strong, positive quantitative correlations between enhancement patterns on MRI and matched histology at high resolutions in the previous chapter. As a result, we became increasingly interested in the potential of this technology for dynamic tracking of small populations of migrating cells. To this end, we used a spontaneous metastasis model of breast cancer in preclinical mice. Additionally, we were increasingly interested in studying the human *Oatp1b3* transporter as a

reporter gene, for future applications of cell tracking in humanized mice models and clinical tracking of cell-based therapies in patients. The main findings of this chapter were: 1) there is significant contrast enhancement by *Oatp1b3*-engineered cells on MRI at 3 Tesla, and 1-mmol/kg Gd-EOB-DTPA in preclinical animal models; 2) *Oatp1b3* allows for longitudinal, whole-body tracking of migrating cells with high sensitivity and resolution; and, 3) the *in vivo* detection limit of *Oatp1b3* is on the order of 10^4 cells, and sits on par with the detection limit of bioluminescence imaging.

These findings were significant, as they offer a new approach for assessing metastatic burden with high resolution, sensitivity, and across the whole-body. With this technology, we were able to dynamically track the metastatic process in deep tissues on MRI, from early-stage metastasis at the single lymph-node level, to late-stage metastasis, when the cancer cells have invaded distant organs, such as the lungs. While tracking metastases non-invasively with BLI allows for whole-body tracking of metastases, light scatter from larger lesions may obscure smaller metastases. Additionally, light scatter limits the resolution of imaging via bioluminescence, making it difficult to pinpoint the exact locations of engineered cells in 3-dimensional space. Further, light attenuation from surrounding signals make it difficult to distinguish between signals stemming from smaller populations of superficial cells or larger populations of deep-seated cells. In this way, light attenuation also contributes to the difficulty of pinpointing exact locations of engineered cells on BLI, and the capacity to quantify their signals on BLI. With *Oatp1b3*-MRI, we were able to

reveal the true locations of engineered cells in 3-dimensional space, with sensitivity comparable to that of bioluminescence. Notably, we were able to reveal smaller micro-metastases via *Oatp1b3*-MRI, which were indiscernible on BLI due to light scatter from larger lesions, allowing us to capture a “true picture” of how the cancer cells grow and migrate throughout the body.

5.1.3 Chapter 4 - Photoacoustic Imaging with *Oatp1* and Indocyanine Green

Finally, in the final research chapter, we wanted to explore the potential of using *Oatp1b3* as a multimodality reporter gene. Individual modalities present with inherent limitations, whereas combining multiple modalities with complementary advantages and limitations offers a more thorough understanding of the biological phenomenon being studied. The initial *Oatp1a1* reporter gene paper introduced an indium-111 radionuclide analog of Gd-EOB-DTPA that was used for SPECT detection of *Oatp1a1*-expressing cells. While SPECT offers a clinical platform with increased sensitivity relative to MRI, it is far more limited in resolution and accessibility. Taking on a different direction, we discovered previous evidence suggesting that indocyanine green was a ligand for the *Oatp1b3* transporter (2). Following this data, we sought to establish *Oatp1b3* as a photoacoustic imaging reporter gene, as indocyanine green exhibits a high extinction coefficient, low quantum yield, and has previously been demonstrated as an effective photoacoustic contrast agent. The main findings of this chapter were: 1) there was significant contrast enhancement on PAI by *Oatp1b3*-engineered cells in preclinical animal models, following administration of 8

mg/kg-ICG; 2) imaging was optimal at 24h post-intraperitoneal injection of ICG, at which point any non-specific ICG across the body was largely cleared; and, 3) specifically, broad increases in PAI signals within the NIR region (730-855 nm) were detected, with a consensus maximal peak at 805 nm.

These findings provided support *Oatp1b3* and ICG as a novel reporter gene system for photoacoustic imaging. While photoacoustic imaging is limited in its ability to capture whole-body images in non small animal models, largely due to the cumulative attenuation of the exciting light and/or optical scattering of the exciting light by materials like bone, there is still great utility for high-resolution localized imaging at depths of several centimeters. The ability to assess genetic and cellular information via the *Oatp1b3*-PAI reporter gene system paves the path towards cost-effective, and therefore, potentially widespread *in vivo* molecular imaging at the preclinical stage, and perhaps even for clinical applications. Longstanding clinical approval and commercial availability of the paired imaging probe, indocyanine green, may also facilitate the dissemination of this technology for use in the laboratory and for clinical tracking of gene- and cell-based therapies in the clinic. Although more work is warranted, our initial studies demonstrate promising feasibility of this photoacoustic imaging approach for various applications requiring gene and/or cellular tracking.

5.2 Challenges and Limitations

5.2.1 Sensitivity of Detection

The ultimate goal of molecular imaging is to detect molecular events as they occur in a living organism. Several factors are important in assessing the effectiveness of an imaging strategy for detecting a biochemical feature. One of these is its sensitivity, defined as the detection threshold of the imaging approach, which can be measured in a number of ways, such as probe concentration, molecular events per second, or number of cells. Some imaging modalities are inherently more sensitive than others. A PET scanner, for instance, can detect probe concentrations between 10^{-11} mol/L to 10^{-12} mol/L, whereas proton MRI has a probe sensitivity of around 10^{-3} mol/L to 10^{-5} mol/L, which can be limiting (3). Due to the novelty of photoacoustic imaging, combined with the assortment of systems built and used for studies in the literature, it is somewhat challenging to estimate the sensitivity of photoacoustic imaging. However, specific studies can provide insight on its sensitivity: the blue product, 5-bromo-4-chloro-indoxyl, generated by the β -galactosidase reporter gene has been detected at depths of several millimeters at 10^{-6} mol/L to 10^{-9} mol/L concentrations (4), which is more sensitive than MRI, but less sensitive than PET. Still, with increasing tissue depth, photoacoustic imaging becomes less sensitive and MRI more advantageous.

Perhaps a more pertinent measure of sensitivity, especially for cell tracking purposes, is the minimal number of detectable cells. Some molecular imaging strategies have already permitted detection of single cells *in vivo*, such

as preloading of cells with iron oxide nanoparticles for detection on MRI (5). In this case, the single cell detection limit of iron oxide nanoparticles has repeatedly been validated at various field strengths, in a number of cell types including cancer cells directed to the brain for metastasis modelling (6, 7), mouse embryonic cells for tracking developmental cell migration (8), primary hepatocytes for transplant quality assurance (9), antigen-specific cytotoxic lymphocytes for targeting tumours (10), and mesenchymal stem cells for regenerative medicine (11). Although cellular pre-loading methods with PET have a limited timeframe due to radioactive decay, dynamic *in vivo* tracking of a single cell on PET was very recently demonstrated using ^{68}Ga -labeled mesoporous silica nanoparticles: a single pre-labelled cancer cell was injected into the tail vein of a mouse, where its velocity in the bloodstream was tracked until its arrest in the lungs (12). The sensitivity of more traditional targeted probe methods for PET is highly variable and depends greatly on probe design, but the most well-designed PET probes in recent years have exhibited detection thresholds on the order of 10^4 cells (13-15).

Reporter genes offer increased accuracy and sensitivity for monitoring of cell trafficking, proliferation, and persistence over long periods of time, relative to *ex vivo* cellular labelling methods (16). The sensitivity of a reporter gene in a particular experiment depends on a number of variables which may vary from study to study, including the efficiency of transfection or transduction, the promoter regulating its expression, and, in relevant cases, the bioavailability of the imaging probe to the reporter protein. Accordingly, studies employing

constitutive promoters and stable transfection or transduction methods would be able to provide information on sensitivity with optimized conditions. Recently, single cell bioluminescence imaging *in vivo* was demonstrated with a red-shifted luciferase-luciferin system (17). However, on more traditional luciferase systems, as few as 10^1 cells can be detected at the skin surface, whereas 10^6 cells would be required at depths of 2 cm due to light attenuation by surrounding tissues (18).

With respect to clinically-relevant modalities, a comparative analysis of several established PET reporter genes, including the human sodium iodide symporter (hNIS), the human norepinephrine transporter (hNET), the human deoxycytidine kinase double mutant (hdCKDM), and the herpes simplex virus type 1 thymidine kinase (hsvTK), revealed detection limits between 10^5 to 10^6 cells (19). With MRI, experimental evidence suggest that the detection limit of the ferritin reporter gene may fall above 10^5 cells *in vitro* at lower field strengths (4.7T) (20), but can go as low as 10^4 cells at high field (11.7T), as demonstrated *in vivo* by scientists from Carnegie Mellon University (21). In perspective, the estimated *in vivo* detection limit of 10^4 cells at 3T presented by *Oatp1b3* in deep tissues is highly competitive, especially when combined with the positive contrast, high resolution, high specificity, and detailed anatomical information that are also provided by the system.

5.2.2 Unintended Effects on Biology by Reporter Genes

The ideal reporter gene would provide detailed high resolution information, with biologically and statistically significant signal-to-noise, high specificity to the target of interest, and importantly, minimal effects on baseline physiological processes, so as not to alter, confound, and/or cause toxicity to the biology being studied (22). Two levels of reporter gene effects exist: 1) the method of reporter gene delivery, a necessary step in cellular engineering, that is relatively independent of the specific reporter gene used in a study; and, 2) any toxic or undesired biological effects caused directly by the reporter protein encoded by the gene introduced into the cell, which is highly dependent on the identity of the specific reporter system used in a study. The means of reporter gene delivery can be divided into methods that result in either transient expression of the reporter gene, *i.e.* extrachromosomal, or integrating methods that result in a stable cell line (23).

The studies presented in this thesis use lentiviral methods to integrate the reporter gene into the host genome, which is a sub-class of retrovirus that can infect both proliferating and non-proliferating cells, and generates a relatively low immune response in target cells (24). This approach is efficient with respect to transporting the reporter gene to its final destination in the genome. However, its drawback is that integration occurs at preferentially-problematic positions in the genome *e.g.* near transcriptional start sites, within transcriptional units, (25) and has been previously been shown to result in disruption of important genes (26). Lentiviral gene delivery could potentially confound results, as any engineered

cells used in a study should ideally match the physiological behavior of the original cell population.

Alternatively, the reporter gene product itself could potentially interfere with vital biochemical pathways and also lead to the generation of engineered cells with marked phenotypic differences relative to their ancestral cell population. For example, one study that focused on the toxic effects of GFP and LacZ revealed that engineered neuronal cells exhibited morphological differences *in vitro* relative to control cells, including long processes which eventually fragmented, smaller rounded cell bodies typical of dying cortical cells, as well as rapid decreases in fractions of viable engineered cells over passaging intervals (27). Although reporter gene-associated toxicity was observed *in vitro*, long term expression of reporter genes *in vivo* was more readily sustained, likely due to the presence of factors within the complex *in vivo* environment that provide support and protection to the engineered cells (27).

In our own studies, *in vitro* proliferation rates of *Oatp1a1*- and *Oatp1b3*-engineered cells were measured over time and found to not be significantly different from those of their parental cell counterparts. Additionally, qualitative observations of cell morphology did not indicate any biologically significant changes in cellular structure and *in vivo* growth rates of *Oatp1*-engineered breast cancer cells did not significantly differ from control tumours. Notably, the metastatic potential of the *Oatp1b3*-engineered MDA-MB-231 breast cancer cell line in mice was in close agreement with animals burdened with control MDA-MB-231 luciferase control cells, as well as previously published timeframes of

studies employing the same cell line and preclinical animal model (28). However, more thorough experiments may be warranted to study specific effects of *Oatp1a1* and *Oatp1b3* expression on baseline biochemical processes and phenotypes such as resting membrane potential. It is assuring that some *Oatp1* transporters with significant ligand overlap relative to *Oatp1a1* and *Oatp1b3*, e.g. human *Oatp1a2*, have widespread tissue expression (29).

5.2.3 Gadolinium Toxicity and Dose

Another aspect to consider when using reporter genes is the potential toxicity of the reporter gene's paired imaging probe. For our photoacoustic reporter gene system described in Chapter 4, indocyanine green is already a widely used contrast agent and has had longstanding approval for clinical use at comparable concentrations to those used in our preclinical *Oatp1b3* study (1), and did not appear to have any effect on the proliferation rates of cells *in vitro*. Although gadolinium-based contrast agents have also been granted clinical approval for some time now, including the Gd-EOB-DTPA compound used as the imaging probe for *Oatp1a1* and *Oatp1b3*, recent concerns over the biological effects of gadolinium have raised serious precautions over their utility in the clinic (30). These include long-term retention of gadolinium in brains of patients after single doses of gadolinium, the specific effects of which are not yet understood, as well as the phenomenon of nephrogenic system fibrosis (NSF), which manifests as scarring of the skin and internal organs as a direct result of exposure to gadolinium (31, 32).

These are not substantial concerns for preclinical studies, like those investigated in this thesis: cells *in vitro* tolerated the gadolinium, as measured via viability and growth assays, and cells *in vivo* developed tumours and metastatic lesions at reasonable rates after repeated administration of gadolinium over several weeks. The doses of gadolinium used in this thesis (0.1-mmol/kg in Chapter 2, 1-mmol/kg in Chapter 4) also fell far below the median lethal dose for rodents, that is 10-mmol/kg (33). The challenge, however, lies in the translation of this system for clinical tracking of gene- and cell-based therapies in patients, which would require a cap on the administered dose of gadolinium. The main concern of chelated Gd constructs here comes from dissociation of free Gd³⁺ ions, which then go on to competitively inhibit Ca²⁺ in a number of physiologically important processes, including adenosine triphosphatase (ATPase) (34, 35).

Under normal circumstances, the chelator allows sufficient clearance of Gd-EOB-DTPA ($t_{1/2} = 1.8 \pm 0.2$ hours) before any biologically significant dissociation occurs (36). Yet, with *Oatp1*, Gd-EOB-DTPA remains within engineered cells, in the body, for several hours, and it is not yet known whether dissociation of free Gd³⁺ is negligible under these parameters. In Chapter 2, we successfully demonstrated that detailed intratumoral distributions of viable cells could be mapped out on MRI at a clinically feasible dose of 0.1 mmol/kg. However, the sensitivity of this system to track small populations of migrating cells at clinically-relevant doses has not yet been assessed. It will be important to maximize reporter expression and optimize imaging parameters for enhancing the conspicuity of engineered cells in order to minimize gadolinium dose.

5.3 Future Work

5.3.1 Genetic Engineering Methods

The studies presented in this thesis use lentiviral vectors to introduce the gene into the genome and constitutive promoters to express the protein product for basic cell tracking purposes. A translational bottleneck, however, is the necessity to engineer cells with randomly-integrating vectors. CRISPR (Clustered Regularly Interspaced Short Palindromic Repeats) and CRISPR-associated (Cas) targeted approaches for knock-in of reporter genes at a genomic safe harbor locus may overcome these safety concerns. To date, our group has built Homology Independent Targeted Integration (HITI) CRISPR/Cas9 plasmids for precise AAVS1-targeted simultaneous knock-in of the *Oatp1a1* reporter gene, and observed increases in knock-in efficiency at the AAVS1 site using HITI vectors compared to traditional homology-directed repair donor vectors (37). Characterization of select HITI clones demonstrated significant *Oatp1a1*-mediated uptake of Gd-EOB-DTPA, thereby supporting the feasibility of introducing *Oatp1a1* via safer genetic engineering approaches (37). Further into the future, we are integrating the *Oatp1b3* reporter gene into increasingly complex genetic circuits, so that its expression is activated in response to a specific stimulus, rather than having it simply expressed at all times (38, 39).

5.3.2 Manganese Probe for MR Imaging of *Oatp1b3* Expression

With the goal of establishing human *Oatp1b3* as a clinical-grade MR reporter gene, the pairing of a gadolinium-based contrast agent as its imaging

probe may considerably hinder its translation to the clinic, due to concerns over toxicity. With this in mind, future work on the *Oatp1b3* reporter gene system will focus on developing a gadolinium-free manganese-based contrast agent as a ligand specific to *Oatp1b3*. To accomplish this goal, manganese porphyrin constructs offer a safe, sensitive, and versatile platform for molecular MRI, but little work has been performed to target these agents towards specific molecular biomarkers. We hypothesize that addition of an ethoxybenzyl (EOB) group to a manganese(III) porphyrin construct would allow for its uptake by cells expressing the *Oatp1b3* transporter.

Decreased toxicity of free manganese(III) relative to free gadolinium(III) *in vivo* (40), in combination with increased stability of the manganese(III) porphyrin structure relative to gadolinium chelates (41, 42) offer increased safety. Additionally, non-porphyrin manganese structures previously developed for MRI sacrifice relaxivity for safety (40), but the planar geometry of the porphyrin construct allows for water coordination both above and below the plane of the agent, leading to increased relaxivity, since relaxivity is directly proportional to the number of water molecules coordinated to the paramagnetic label and the residency time of the water molecules. In conjunction with the ability to “tune” the electron configuration at the paramagnetic center, these properties collectively contribute to increased relaxivity of Mn(III)-EOB-TriCP relative to Gd(III)-EOB-DTPA. Further, the porphyrin backbone offers four locations onto which different functional groups may be added to alter important properties such as circulation half-life and ligand activity. Promising preliminary data poses the possibility of

replacing Gd-EOB-DTPA entirely with Mn-EOB-TriCP, pending future work focused on comparing enhancement of *Oatp1b3*-expressing cells *in vivo* between Mn-EOB-TriCP and Gd-EOB-DTPA in animals, as well as assessing *in vivo* biodistribution, demetallation and toxicity of Mn-EOB-TriCP.

5.3.3 Syngeneic Reporter Gene Systems

A separate issue is that introduction of a foreign protein into the preclinical animal model may elicit an immune reaction from the host, such that reporter gene expression becomes inconsistent, suppresses tumour growth, limits metastasis, and/or leads to therapeutic response misinterpretations (43). To circumvent this issue at the proof-of-principle stage, immune-compromised animal models were used to assess and characterize the *Oatp1* reporter gene system in this thesis. In the future, however, we hope to develop a syngeneic reporter gene approach for cell tracking. In essence, we hope to develop mouse *Oatp1a1* for murine cell tracking in immune-competent mouse models, rat *Oatp1a1* for rat cell tracking in immune-competent rat models, and human *Oatp1b3* for cell tracking in humanized animal models (44). In theory, any T cells that would have reacted to the reporter protein should have been negatively selected and eliminated during immune system development. Future work will focus on developing these systems and quantifying differences between reporter-expressing cells relative to non-reporter expressing cells. In combination, with new genetic engineering methods (**Section 5.3.1**), a gadolinium-free manganese probe for imaging (**Section 5.3.2**) and a syngeneic reporter gene scheme

(**Section 5.3.3**), we hope to develop the *Oatp1* reporter gene as a safe, sensitive, non-confounding imaging system for cell tracking in preclinical animal models, as well as cell tracking of gene- and cell-based therapies in human patients down the line.

5.4 References

1. Alander JT, Kaartinen I, Laakso A, Patila T, Spillmann T, Tuchin VV, Venermo M, Valisuo P. A review of indocyanine green fluorescent imaging in surgery. *Int J Biomed Imaging* 2012;2012:940585. doi: 10.1155/2012/940585
2. de Graaf W, Hausler S, Heger M, van Ginhoven TM, van Cappellen G, Bennink RJ, Kullak-Ublick GA, Hesselmann R, van Gulik TM, Stieger B. Transporters involved in the hepatic uptake of (99m)Tc-mebrofenin and indocyanine green. *J Hepatol* 2011;54(4):738-745. doi: 10.1016/j.jhep.2010.07.047
3. Pysz MA, Gambhir SS, Willmann JK. Molecular imaging: current status and emerging strategies. *Clin Radiol* 2010;65(7):500-516. doi: 10.1016/j.crad.2010.03.011
4. Li L, Zemp RJ, Lungu G, Stoica G, Wang LV. Photoacoustic imaging of lacZ gene expression in vivo. *J Biomed Opt* 2007;12(2):020504. doi: 10.1117/1.2717531
5. Wang YX. Current status of superparamagnetic iron oxide contrast agents for liver magnetic resonance imaging. *World J Gastroenterol* 2015;21(47):13400-13402. doi: 10.3748/wjg.v21.i47.13400
6. Heyn C, Ronald JA, Mackenzie LT, MacDonald IC, Chambers AF, Rutt BK, Foster PJ. In vivo magnetic resonance imaging of single cells in mouse brain with optical validation. *Magn Reson Med* 2006;55(1):23-29. doi: 10.1002/mrm.20747
7. Heyn C, Ronald JA, Ramadan SS, Snir JA, Barry AM, MacKenzie LT, Mikulis DJ, Palmieri D, Bronder JL, Steeg PS, Yoneda T, MacDonald IC, Chambers AF, Rutt BK, Foster PJ. In vivo MRI of cancer cell fate at the single-cell level in a mouse model of breast cancer metastasis to the brain. *Magn Reson Med* 2006;56(5):1001-1010. doi: 10.1002/mrm.21029

8. Shapiro EM, Skrtic S, Sharer K, Hill JM, Dunbar CE, Koretsky AP. MRI detection of single particles for cellular imaging. *Proc Natl Acad Sci U S A* 2004;101(30):10901-10906. doi: 10.1073/pnas.0403918101
9. Shapiro EM, Sharer K, Skrtic S, Koretsky AP. In vivo detection of single cells by MRI. *Magn Reson Med* 2006;55(2):242-249. doi: 10.1002/mrm.20718
10. Smirnov P, Poirier-Quinot M, Wilhelm C, Lavergne E, Ginefri JC, Combadiere B, Clement O, Darrasse L, Gazeau F. In vivo single cell detection of tumor-infiltrating lymphocytes with a clinical 1.5 Tesla MRI system. *Magn Reson Med* 2008;60(6):1292-1297. doi: 10.1002/mrm.21812
11. Ariza de Schellenberger A, Kratz H, Farr TD, Lova N, Hauptmann R, Wagner S, Taupitz M, Schnorr J, Schellenberger EA. Labeling of mesenchymal stem cells for MRI with single-cell sensitivity. *Int J Nanomedicine* 2016;11:1517-1535. doi: 10.2147/IJN.S101141
12. Jung KO, Kim TJ, Yu JH, Rhee S, Zhao W, Ha B, Red-Horse K, Gambhir SS, Prax G. Whole-body tracking of single cells via positron emission tomography. *Nat Biomed Eng* 2020. doi: 10.1038/s41551-020-0570-5
13. Yusufi N, Mall S, Bianchi HO, Steiger K, Reder S, Klar R, Audehm S, Mustafa M, Nekolla S, Peschel C, Schwaiger M, Krackhardt AM, D'Alessandria C. In-depth Characterization of a TCR-specific Tracer for Sensitive Detection of Tumor-directed Transgenic T Cells by Immuno-PET. *Theranostics* 2017;7(9):2402-2416. doi: 10.7150/thno.17994
14. Wei W, Jiang D, Ehlerding EB, Luo Q, Cai W. Noninvasive PET Imaging of T cells. *Trends Cancer* 2018;4(5):359-373. doi: 10.1016/j.trecan.2018.03.009

15. Mayer AT, Gambhir SS. The Immunoimaging Toolbox. *J Nucl Med* 2018;59(8):1174-1182. doi: 10.2967/jnumed.116.185967
16. Perrin J, Capitaio M, Mouglin-Degraef M, Guerard F, Faivre-Chauvet A, Rbah-Vidal L, Gaschet J, Guilloux Y, Kraeber-Bodere F, Cherel M, Barbet J. Cell Tracking in Cancer Immunotherapy. *Front Med (Lausanne)* 2020;7:34. doi: 10.3389/fmed.2020.00034
17. Iwano S, Sugiyama M, Hama H, Watakabe A, Hasegawa N, Kuchimaru T, Tanaka KZ, Takahashi M, Ishida Y, Hata J, Shimozone S, Namiki K, Fukano T, Kiyama M, Okano H, Kizaka-Kondoh S, McHugh TJ, Yamamori T, Hioki H, Maki S, Miyawaki A. Single-cell bioluminescence imaging of deep tissue in freely moving animals. *Science* 2018;359(6378):935-939. doi: 10.1126/science.aaq1067
18. Rice BW, Cable MD, Nelson MB. In vivo imaging of light-emitting probes. *J Biomed Opt* 2001;6(4):432-440. doi: 10.1117/1.1413210
19. Moroz MA, Zhang H, Lee J, Moroz E, Zurita J, Shenker L, Serganova I, Blasberg R, Ponomarev V. Comparative Analysis of T Cell Imaging with Human Nuclear Reporter Genes. *J Nucl Med* 2015;56(7):1055-1060. doi: 10.2967/jnumed.115.159855
20. Cohen B, Dafni H, Meir G, Harmelin A, Neeman M. Ferritin as an endogenous MRI reporter for noninvasive imaging of gene expression in C6 glioma tumors. *Neoplasia* 2005;7(2):109-117. doi: 10.1593/neo.04436
21. Iordanova B, Ahrens ET. In vivo magnetic resonance imaging of ferritin-based reporter visualizes native neuroblast migration. *Neuroimage* 2012;59(2):1004-1012. doi: 10.1016/j.neuroimage.2011.08.068

22. Ashmore-Harris C, Iafrate M, Saleem A, Fruhwirth GO. Non-invasive Reporter Gene Imaging of Cell Therapies, including T Cells and Stem Cells. *Mol Ther* 2020;28(6):1392-1416. doi: 10.1016/j.ymthe.2020.03.016
23. Anguela XM, High KA. Entering the Modern Era of Gene Therapy. *Annu Rev Med* 2019;70:273-288. doi: 10.1146/annurev-med-012017-043332
24. Milone MC, O'Doherty U. Clinical use of lentiviral vectors. *Leukemia* 2018;32(7):1529-1541. doi: 10.1038/s41375-018-0106-0
25. Ciuffi A. The benefits of integration. *Clin Microbiol Infect* 2016;22(4):324-332. doi: 10.1016/j.cmi.2016.02.013
26. Lewinski MK, Yamashita M, Emerman M, Ciuffi A, Marshall H, Crawford G, Collins F, Shinn P, Leipzig J, Hannenhalli S, Berry CC, Ecker JR, Bushman FD. Retroviral DNA integration: viral and cellular determinants of target-site selection. *PLoS Pathog* 2006;2(6):e60. doi: 10.1371/journal.ppat.0020060
27. Detrait ER, Bowers WJ, Halterman MW, Giuliano RE, Bennice L, Federoff HJ, Richfield EK. Reporter gene transfer induces apoptosis in primary cortical neurons. *Mol Ther* 2002;5(6):723-730. doi: 10.1006/mthe.2002.0609
28. Puchalapalli M, Zeng X, Mu L, Anderson A, Hix Glickman L, Zhang M, Sayyad MR, Mosticone Wangensteen S, Clevenger CV, Koblinski JE. NSG Mice Provide a Better Spontaneous Model of Breast Cancer Metastasis than Athymic (Nude) Mice. *PLoS One* 2016;11(9):e0163521. doi: 10.1371/journal.pone.0163521
29. Roth M, Obaidat A, Hagenbuch B. OATPs, OATs and OCTs: the organic anion and cation transporters of the SLCO and SLC22A gene superfamilies. *Br J Pharmacol* 2012;165(5):1260-1287. doi: 10.1111/j.1476-5381.2011.01724.x

30. Burke LM, Ramalho M, AlObaidy M, Chang E, Jay M, Semelka RC. Self-reported gadolinium toxicity: A survey of patients with chronic symptoms. *Magn Reson Imaging* 2016;34(8):1078-1080. doi: 10.1016/j.mri.2016.05.005
31. Perazella MA. Current status of gadolinium toxicity in patients with kidney disease. *Clin J Am Soc Nephrol* 2009;4(2):461-469. doi: 10.2215/CJN.06011108
32. Rogosnitzky M, Branch S. Gadolinium-based contrast agent toxicity: a review of known and proposed mechanisms. *Biometals* 2016;29(3):365-376. doi: 10.1007/s10534-016-9931-7
33. Schuhmann-Giampieri G, Schmitt-Willich H, Press WR, Negishi C, Weinmann HJ, Speck U. Preclinical evaluation of Gd-EOB-DTPA as a contrast agent in MR imaging of the hepatobiliary system. *Radiology* 1992;183(1):59-64. doi: 10.1148/radiology.183.1.1549695
34. Ogurusu T, Wakabayashi S, Shigekawa M. Functional characterization of lanthanide binding sites in the sarcoplasmic reticulum Ca(2+)-ATPase: do lanthanide ions bind to the calcium transport site? *Biochemistry* 1991;30(41):9966-9973. doi: 10.1021/bi00105a022
35. Idee JM, Berthommier C, Goulas V, Corot C, Santus R, Hermine C, Schaefer M, Bonnemain B. Haemodynamic effects of macrocyclic and linear gadolinium chelates in rats: role of calcium and transmetallation. *Biometals* 1998;11(2):113-123. doi: 10.1023/a:1009225911668
36. Gschwend S, Ebert W, Schultze-Mosgau M, Breuer J. Pharmacokinetics and imaging properties of Gd-EOB-DTPA in patients with hepatic and renal impairment. *Invest Radiol* 2011;46(9):556-566. doi: 10.1097/RLI.0b013e31821a218a

37. Kelly J. J. S-MM, Nyström N. N., Chen Y., Evans M. M., Hamilton A. M., Ronald J. A. A Safe Harbor-Targeted CRISPR/Cas9 Homology Independent Targeted Integration (HITI) System for Multi-Modality Reporter Gene-Based Cell Tracking. *bioRxiv* 2020;2020.02.10.942672. doi: <https://doi.org/10.1101/2020.02.10.942672>
38. Morsut L, Roybal KT, Xiong X, Gordley RM, Coyle SM, Thomson M, Lim WA. Engineering Customized Cell Sensing and Response Behaviors Using Synthetic Notch Receptors. *Cell* 2016;164(4):780-791. doi: 10.1016/j.cell.2016.01.012
39. Roybal KT, Rupp LJ, Morsut L, Walker WJ, McNally KA, Park JS, Lim WA. Precision Tumor Recognition by T Cells With Combinatorial Antigen-Sensing Circuits. *Cell* 2016;164(4):770-779. doi: 10.1016/j.cell.2016.01.011
40. Gale EM, Wey HY, Ramsay I, Yen YF, Sosnovik DE, Caravan P. A Manganese-based Alternative to Gadolinium: Contrast-enhanced MR Angiography, Excretion, Pharmacokinetics, and Metabolism. *Radiology* 2018;286(3):865-872. doi: 10.1148/radiol.2017170977
41. Frenzel T, Lengsfeld P, Schirmer H, Hutter J, Weinmann HJ. Stability of gadolinium-based magnetic resonance imaging contrast agents in human serum at 37 degrees C. *Invest Radiol* 2008;43(12):817-828. doi: 10.1097/RLI.0b013e3181852171
42. Reboucas JS, DeFreitas-Silva G, Spasojevic I, Idemori YM, Benov L, Batinic-Haberle I. Impact of electrostatics in redox modulation of oxidative stress by Mn porphyrins: protection of SOD-deficient *Escherichia coli* via alternative mechanism where Mn porphyrin acts as a Mn carrier. *Free Radic Biol Med* 2008;45(2):201-210. doi: 10.1016/j.freeradbiomed.2008.04.009

43. Day CP, Carter J, Weaver Ohler Z, Bonomi C, El Meskini R, Martin P, Graff-Cherry C, Feigenbaum L, Tuting T, Van Dyke T, Hollingshead M, Merlino G. "Glowing head" mice: a genetic tool enabling reliable preclinical image-based evaluation of cancers in immunocompetent allografts. *PLoS One* 2014;9(11):e109956. doi:

10.1371/journal.pone.0109956

44. Walsh NC, Kenney LL, Jangalwe S, Aryee KE, Greiner DL, Brehm MA, Shultz LD. Humanized Mouse Models of Clinical Disease. *Annu Rev Pathol* 2017;12:187-215. doi:

10.1146/annurev-pathol-052016-100332

CHAPTER 6 Appendix

The materials provided in this section include permissions for figures and texts copyrighted by third parties, as well as the curriculum vitae of the candidate at the time of thesis submission on May 14, 2020.

6.1. Permissions

Permissions for figures acquired from third parties are included in this section.



Nivin Nyström <[REDACTED]>

Permission to Use Copyrighted Material in Doctoral Thesis

PNAS Permissions <[REDACTED]>
To: Nivin Nyström <[REDACTED]>

Fri, Jul 17, 2020 at 3:04 PM

Dear Dr. Nyström,

Thank you for your message. Permission is granted for your use of the material as described in your request. Please include a complete citation for the original PNAS article when reusing the material. Because this material published after 2008, a copyright note is not needed. There is no charge for this material, either. Let us know if you have any questions.

Best regards,

Delaney Cruickshank for

Diane Sullenberger

PNAS Executive Editor

From: Nivin Nyström <[REDACTED]>**Sent:** Wednesday, July 15, 2020 11:10 AM**To:** PNAS Permissions <[REDACTED]>**Subject:** Permission to Use Copyrighted Material in Doctoral Thesis

Dear Editor/Publisher(s),

I am a University of Western Ontario graduate student completing my Doctoral thesis entitled "A Genetically-Encoded Reporter for Imaging in Deep Tissues". I would like permission to allow inclusion of the following material in my thesis:

Figure 3A-C from Patrick et al. Dual-modality gene reporter for in vivo imaging. *Proc Natl Acad Sci U S A* 2014;111(1):415-420. doi: 10.1073/pnas.131900111

This material will be attributed through a citation in the thesis. I have provided details on access and licensing of the thesis below. If you could please confirm *in writing or by email* that these arrangements meet your approval, I would greatly appreciate it. If your approval requires any changes to these arrangements, please let me know and I would be happy to address any concerns. Thank you in advance.

Thesis Access: My thesis will be available in full-text on the internet for reference, study and/or copy. Except in situations where a thesis is under embargo or restriction, the electronic version will be accessible through the Western Libraries web pages, the Library's web catalogue, and also through web search engines.

7/24/2020

Gmail - Permission to Use Copyrighted Material in Doctoral Thesis

License Agreement: I will be granting Library and Archives Canada and ProQuest/UMI a non-exclusive license to reproduce, loan, distribute, or sell single copies of my thesis by any means and in any form or format. These rights will in no way restrict republication of the material in any other form by you or by others authorized by you.

Nivin Nyström BSc (Hons)

PhD *Candidate*, Medical Biophysics

Robarts Research Institute, Room 2298

Schulich School of Medicine and Dentistry

The University of Western Ontario

p. ██████████

[Quoted text hidden]



Nivin Nyström <[REDACTED]>

Permission to Use Copyrighted Material in Doctoral Thesis

2 messages

Nivin Nyström <[REDACTED]>

Wed, Jul 15, 2020 at 11:15 AM

To: [REDACTED]

Dear Editor/Publisher(s),

I am a University of Western Ontario graduate student completing my Doctoral thesis entitled "A Genetically-Encoded Reporter for Imaging in Deep Tissues". I would like permission to allow inclusion of the following material in the introduction chapter of my thesis:

Figure 1 from Brunker et al. Photoacoustic imaging using genetically encoded reporters: a review. J Biomed Opt 2017;22(7). doi: 10.1117/1.JBO.22.7.070901

This material will be attributed through a citation in the thesis. I have provided details on access and licensing of the thesis below. If you could please confirm *in writing or by email* that these arrangements meet your approval, I would greatly appreciate it. If your approval requires any changes to these arrangements, please let me know and I would be happy to address any concerns. Thank you in advance.

Thesis Access: My thesis will be available in full-text on the internet for reference, study and/or copy. Except in situations where a thesis is under embargo or restriction, the electronic version will be accessible through the Western Libraries web pages, the Library's web catalogue, and also through web search engines.

License Agreement: I will be granting Library and Archives Canada and ProQuest/UMI a non-exclusive license to reproduce, loan, distribute, or sell single copies of my thesis by any means and in any form or format. These rights will in no way restrict republication of the material in any other form by you or by others authorized by you.

Nivin Nyström BSc (Hons)
 PhD ~~Candidate~~, Medical Biophysics
 Robarts Research Institute, Room 2298
 Schulich School of Medicine and Dentistry
 The University of Western Ontario
 p. [REDACTED]



Unless expressly stated otherwise, this message is confidential and may be privileged. It is intended for the addressee(s) only. Access to this e-mail by anyone else is unauthorized. If you are not an addressee, any disclosure or copying of the content of this e-mail or any action taken (or not taken) in reliance on it is unauthorized and may be unlawful. If you are not an addressee, please inform the sender immediately.

Shannon Engelbrecht <[REDACTED]>

Wed, Jul 15, 2020 at 12:34 PM

To: Nivin Nyström <[REDACTED]>

Dear Dr. Nyström,

Thank you for seeking permission from SPIE to reprint material from our publications. The article you have requested to reprint from is published under Creative Commons (CC BY 4.0)—Gold Open Access. For articles published under CC BY 4.0, users are free to share (copy, distribute, and transmit), to remix (adapt), and to make commercial use of the Article under the following conditions:

7/24/2020

Gmail - Permission to Use Copyrighted Material in Doctoral Thesis

Attribution: Users must attribute the contribution in the manner specified by the author or licensor (but not in any way that suggests that they or their use of the Article is endorsed by the Author or licensor). See citation formatting below.

Notice: For any reuse or distribution, users must make clear to others the license terms of this work, preferably using a link to the [Creative Commons webpage](#).

The full legal code of the CC BY 4.0 license can be found at <https://creativecommons.org/licenses/by/4.0/legalcode>.

Citation format (Journals):

Author(s), "Article Title," Journal Title and Volume Number (Issue), Article Number (Publication Date). [http://dx.doi.org/...](http://dx.doi.org/)

Please let me know if I may be of further assistance.

Sincerely,

Shannon Engelbrecht

Conference Programs & Proceedings Assistant

TEL: 



SPIE is the international society for optics and photonics

<http://SPIE.org>

SPIE.

[Quoted text hidden]

6.2. Curriculum Vitae

Education

2016/9 - 2020/6 (expected)	Doctor of Philosophy, Medical Biophysics Supervisors: Dr. Timothy Scholl and Dr. John Ronald <i>The University of Western Ontario, London, Canada</i>
2012/9 - 2016/6	Bachelor of Science (Honours), Genetics <i>The University of Western Ontario, London, Canada</i>

Awards and Recognitions

2020/3	Invited Student Keynote, Alan C. Burton Day 29 th Annual Alan C. Burton Day, University of Western Ontario [Cancelled, COVID]
2020/2	Graduate Educational Travel Award International Society for Magnetic Resonance in Medicine (ISMRM)
2019/9	Industry-Selected Award World Molecular Imaging Society (WMIS)
2019/9	Finalist, Shark Tank Business Competition World Molecular Imaging Society (WMIS)
2019/9	Invited Talk Canadian Molecular Imaging pre-symposium, World Molecular Imaging Society (WMIS)
2019/9	Drs. Madge and Charles Macklin Award Schulich School of Medicine, University of Western Ontario
2019/7	Young Investigator Award Cellular and Molecular Imaging Study Group, International Society for Magnetic Resonance in Medicine (ISMRM)
2019/7	Molecular MRI Travel Award Cellular and Molecular Imaging Study Group, International Society for Magnetic Resonance in Medicine (ISMRM)

2019/4	Invited Talk with Dr. Silvio Aime Cellular and Molecular Imaging Study Group, International Society for Magnetic Resonance in Medicine (ISMRM)
2019/4	Honourable Mention for Best Oral Presentation London Health Research Day, Lawson Health Research Institute and Schulich School of Medicine, University of Western Ontario
2019/4	Lucille and Norton Wolf Award Lawson Health Research Institute and Schulich School of Medicine
2019/3	Alfred Jay Award in Cellular and Cardiovascular Research Department of Medical Biophysics, Schulich School of Medicine
2018/9 - 2021/8	NSERC PGS Doctoral Scholarship Natural Sciences and Engineering Council (NSERC) of Canada
2018/6	2 nd Place Oral Presentation Cellular and Molecular Imaging Study Group, International Society of Magnetic Resonance in Medicine (ISMRM)
2018/6	1 st Place Poster Prize Oncology Research Day, Schulich School of Medicine
2018/6	1 st Place Poster Prize Robarts Research Retreat, Robarts Research Institute
2018/5 - 2018/8	Translational Breast Cancer Research Scholarship Breast Cancer Society of Canada
2018/4	Molecular Imaging Travel Award Molecular Imaging Program, University of Western Ontario
2018/3	Top Team, Proteus Innovation Competition Richard Ivey School of Business and WORLDiscoveries

2017/9	Graduate Student Innovation Scholar Richard Ivey School of Business
2017/7	Invited Student Keynote Speaker Synthetic Biology Symposium, Ontario Genomics
2017/6	1st Place Oral Presentation Award London Imaging Discovery Day, Schulich School of Medicine
2017/5 – 2018/4	NSERC CGS Masters Scholarship Natural Sciences and Engineering Council (NSERC) of Canada
2017/5 – 2018/4	Ontario Graduate Scholarship [Declined] The Government of Ontario
2016/9 – 2020/6	Western Graduate Research Award University of Western Ontario
2015/4	Letter of Advanced Student Leadership University of Western Ontario
2012/6	Merit in Science Award Shad Valley

Journal Publications

NN Nyström, JJ Kelly, FM Martinez, TJ Scholl, JA Ronald. Whole-Body Profiling of Spontaneously Metastasizing Cancer Cells. *In Preparation*.

JJ Kelly, M Saeed-Marand, **NN Nyström**, Y Chen, MM Evans, AM Hamilton, JA Ronald. A Safe Harbor-Targeted CRISPR/Cas9 Homology Independent Targeted Integration System for Multi-Modality Reporter Gene-Based Cell Tracking. *BioRxiv* doi.org/10.1101/2020.02.10.942672. *In Revision*.

NN Nyström, LCM Yip, JLL Carson, TJ Scholl, JA Ronald. Development of a Human Photoacoustic Imaging Reporter Gene using the Clinical Dye Indocyanine Green. *Radiology: Imaging Cancer* 2019 November; 1(2): e190035.

NN Nyström, AM Hamilton, W Xia, S Liu, TJ Scholl, JA Ronald. Longitudinal Visualization of Viable Cancer Cell Intratumoral Distribution in Mouse Models using *Oatp1a1*-enhanced Magnetic Resonance Imaging. *Investigative Radiology* 2019 May; 54(5): 302-311.

Oral Presentations

NN Nyström, TJ Scholl, JA Ronald. Whole-body Detection of Metastasizing Cancer Cells in Preclinical Animal Models. International Society for Magnetic Resonance in Medicine, Virtual Conference, August 8-14, 2020.

M Mozaffari, **NN Nystrom**, A Li, M Bellyou, TJ Scholl, R Bartha. Chemical Exchange Saturation Transfer MRI: Sensitive to Intracellular pH Change Over Time in a Rat Model of Brain Cancer. American Association of Physicist in Medicine Congress, Virtual Conference, July 12-16, 2020.

M Mozaffari, **NN Nystrom**, A Li, M Bellyou, TJ Scholl, R Bartha. Study of Tumour Intracellular pH (pHi) in a Rat Model of Glioblastoma Using CEST-MRI. Canadian Association of Physicists Congress, Virtual Conference, June 8-12, 2020.

NN Nyström, FM Martinez, JJ Kelly, TJ Scholl, JA Ronald. Tracking the Spontaneous Metastasis of Triple Negative Breast Cancer Cells in Preclinical Animals via Reporter Gene Imaging at 3 Tesla. Imaging Network of Ontario, Virtual Conference, March 26-27, 2020.

NN Nyström, **TD Wang**, JA Ronald. An Aerosolized Cancer-Activatable PET Reporter Gene System for Early Detection of Lung Cancer. World Molecular Imaging Congress, Montreal, Canada, September 4-7, 2019. **Finalist, Business Shark Tank Competition.**

NN Nyström, HA Liu, XA Zhang, TJ Scholl, JA Ronald. Of mice and Mn: Preclinical development of a gadolinium-free MRI probe targeting organic anion-transporting polypeptides. World Molecular Imaging Congress, Montreal, Canada, September 4-7, 2019.

NN Nyström, LCM Yip, JLL Carson, TJ Scholl, JA Ronald. A human photoacoustic and 3T magnetic resonance reporter gene system that uses the clinical agents indocyanine green and Gd-EOB-DTPA. World Molecular Imaging Congress, Montreal, Canada, September 4-7, 2019. **Industry-Choice Award.**

NN Nyström. Development of *Oatp1* as a Multimodality Reporter Gene. Canadian Molecular Imaging Symposium, World Molecular Imaging Congress, Montreal, Canada, September 3, 2019. **Invited Talk.**

NN Nyström, LCM Yip, JLL Carson, TJ Scholl, JA Ronald. *In vivo* cell tracking via a clinically-relevant reporter gene for fluorescence, photoacoustic, and magnetic resonance imaging at 3 Tesla. Cellular and Molecular Imaging Workshop, International Society for Magnetic Resonance in Medicine, St. John's, Canada, July 14-17, 2019. **Young Investigator Award.**

JJ Kelly, M Saeed-Marand, **NN Nyström**, Y Chen, MM Evans, AM Hamilton, JA Ronald. A Safe Harbor-Targeted CRISPR/Cas9 Homology Independent Targeted Integration System for Multi-Modality Reporter Gene-Based Cell Tracking. Cellular and Molecular Imaging Workshop, International Society for Magnetic Resonance in Medicine, St. John's, Canada, July 14-17, 2019.

MM Mozaffari, **NN Nyström**, A Li, M Bellyou, TJ Scholl, R Bartha. Tumor Intracellular pH in a Rat C6 Model of Glioblastoma. Roberts Research Retreat, London, Canada, June 7, 2019.

NN Nyström, S Aime. Developments of the *Oatp1* Reporter Gene. International Society for Magnetic Resonance in Medicine, Montreal, Canada, May 11-16, 2019. **Invited Talk.**

NN Nyström, LCM Yip, JLL Carson, TJ Scholl, JA Ronald. Multimodality OATP1B3-enhanced reporter gene imaging of engineered cells via fluorescence, photoacoustic, and magnetic resonance imaging. International Society for Magnetic Resonance in Medicine, Montreal, Canada, May 11-16, 2019.

NN Nyström, LCM Yip, JLL Carson, TJ Scholl, JA Ronald. *In vivo* cell tracking via multimodality reporter-based fluorescence, photoacoustic, and magnetic resonance imaging at 3 Tesla. London Health Research Day, London, Canada, April 30, 2019. **Honourable Mention for Best Oral Presentation.**

NN Nyström, LCM Yip, JLL Carson, TJ Scholl, JA Ronald. *In vivo* cell tracking via a clinically-relevant reporter gene for fluorescence, photoacoustic, and magnetic resonance imaging at 3 Tesla. Imaging Network of Ontario, Toronto, Canada, March 28-29, 2019.

NN Nyström, AM Hamilton, W Xia, S Liu, TJ Scholl, JA Ronald. *Oatp1a1* reporter gene-enhanced magnetic resonance imaging of triple negative breast cancer in animal models at 3 Tesla. International Society for Magnetic Resonance in Medicine, Paris, France, June 16-21, 2018. **2nd Place Oral Presentation Award in Cellular and Molecular Imaging.**

NN Nyström, AM Hamilton, TJ Scholl, JA Ronald. Novel MRI reporter genes for *in vivo* imaging. Provincial Synthetic Biology Symposium, London, Canada, July 28, 2017. **Invited Student Keynote.**

NN Nyström, TJ Scholl, JA Ronald. Overcoming the obscurity of triple-negative breast cancer via Organic Anion-Transporting Polypeptide (OATP)-enhanced MRI. London Imaging Discovery Day, London, Canada, June 27, 2017. **1st Place Oral Presentation Award.**

Employment

2018/9 - present	BIOPHYS 9700 Graduate Teaching Assistant Department of Medical Biophysics, University of Western Ontario
2016/5 - 2018/8	Factory Worker Williams Form and Rockbolt

Event Administration

2019/4 - present	Cellular and Molecular Imaging Study Group Trainee, International Society for Magnetic Resonance In Medicine (ISMRM) Congress Preparing administrative group meeting materials; attending virtual meetings with the study group council; and leading the organization of the official study group-sponsored member-initiated symposium (MIS) application for approval by the Board of Governors of ISMRM. Elected as the official trainee representative for the 2020-2021 conference year.
2019/9 - present	Ontario Rising Star Trainee Research Network Co-founder, Ontario Institute for Cancer Research (OICR) In conjunction with the Ontario Institute for Cancer Research, the Ontario Trainee Network aims to facilitate the professional development and collaborative coordination of cancer research trainees, through mentorship activities, travel awards, speaker series, newsletters, and more.
2017/5 - 2019/8	Executive Member, Robarts Association of Trainees (RATs) Organized the Robarts Research Retreat and smaller activities including professional development seminars and socials; brainstorming novel events and scholarship prizes unique to Robarts trainees; facilitating investigator/trainee interactions between Imaging and Molecular Medicine Divisions of Robarts Research Institute; and acting as a council representative for the Imaging Division.
2017/8 - 2019/8	Canadian Cancer Society Research Information Outreach Team (RIOT) RIOT aims to communicate current cancer research objectives to the general public in a number of different ways, including through local newspaper publications, public coffee workshops, and through its annual Let's Talk Cancer event aimed towards high school students.

2016/4 - present	<p>Organizing Committee, Thames Valley Science and Engineering Fair</p> <p>Recruited secondary schools to participate; reviewed individual abstract submissions for approval; and set up students' posters in the Thompson Gym at the University of Western Ontario on days leading up to the science fair.</p>
2016/4 - present	<p>Awards Committee, Thames Valley Science and Engineering Fair</p> <p>Listened to and discussed the research endeavours of secondary school students as they presented their posters; provided constructive feedback to the students regarding their projects; coordinated with other judges in a closed room on the distribution of awards and scholarships to the top posters, advocating for certain posters over others.</p>
2014/4 - 2015/4	<p>Director of Programming, TEDxWesternU</p> <p>Recruited various alumni and faculty from across the University of Western Ontario to participate as speakers for the conference; assisted speakers in preparation for their lectures; provided transportation and living accommodations for certain speakers; designed an itinerary handbook, organized its printing and distribution to the attendees; and participated in the conference as the master of ceremonies.</p>

Mentoring Activities

2017/5 - present	<p>4th Year Thesis Training, University of Western Ontario</p> <p>Number of Mentorees: 4</p> <p>Introducing the 4th year student to the project, its scope, training protocols and publication materials; providing training for relevant research techniques such as cell culture, cloning, PCR analysis, sequencing, fluorescence microscopy, fluorescence-activated cell sorting (FACS), CRISPR design and engineering, luciferase assays and bioluminescent imaging; and providing discussion to the student regarding topics pertaining to the project; lecturing and demonstrating data analysis.</p>
2016/9 - present	<p>Supervisor, Partners in Experiential Learning</p> <p>Number of Mentorees: 3</p> <p>Preparing training protocols and materials focused on molecular techniques such as cell culture, cloning, PCR, immunoblotting, sequencing, cell lysis, microscopy, BCA normalization, luciferase assays and bioluminescent imaging; supervising and providing feedback on</p>

methodology; lecturing and demonstrating data analysis; and allowing the students to contribute to the research goals of the Ronald Lab through data acquisition. **Special note:** One of my students, Shirley Liu, went on to win gold at the Thames Valley Science Fair, and received an additional award at the Canada Wide Science Fair in 2017.

2013/9 - 2016/8

Guidance Tutor, Learning Disabilities Association of London Region

Number of Mentorees: 12

Worked with elementary school students, individually and in group settings, on building good work ethics and organizational skills, as well as critical thinking; lectured on the sciences and maths, going over homework, tackling complex problems and delving into deeper thought experiments; and a special focus was placed on overcoming learning disabilities in science and math subjects, for example by drawing out word problems instead of trying to solve them straight from the reading.

End of Curriculum Vitae for Nivin Nyström